Master's thesis

2023

Aaron Henskens

NTNU
Norwegian University of
Science and Technology
Faculty of Engineering
Department of Marine Technology

Aaron Henskens

Examination of environmental lumping methods for fatigue assessment of floating wind turbines

November 2023

NTNU
Norwegian University of
Science and Technology

NTNU
Norwegian University of
Science and Technology

Examination of environmental lumping methods for fatigue assessment of floating wind turbines

Aaron Henskens

European Wind Energy Master
Submission date: November 2023
Supervisor: Erin Bachynski-Polić
Co-supervisor: Eliz-Mari Lourens, Anastasios Stampoultzoglou, Jasper van den Broek-de Bruijn

Norwegian University of Science and Technology
Department of Marine Technology

Abstract

Floating turbines constitute a new field of research within offshore wind, a young industry itself. The demand for offshore wind turbines is likely to significantly increase in the next decades. Where bottom fixed turbines are generally limited to a maximum water depth of 60 m, floating turbines are not, making them suitable for offshore energy harvesting in deep waters, such as along the coasts of Japan and the United States of America. Due to the repeated load cycles caused by wind and waves, small material cracks are initiated and can propagate, resulting in material failure. This phenomenon is described as fatigue damage and is one of the governing factors during the design phase of offshore turbines. In order to analyse whether material failure occurs during the turbine's lifetime, a fatigue damage analysis is performed. Performing a fatigue damage analysis of an offshore turbine may take several months, due to the high number of sea states that each require a 1-hour time domain load simulation. To reduce computational time, a lumping method is used to select one or several lumped sea states in each scatter diagram. Lumping methods are designed to select lumped sea states for which the fatigue damage approximates the average fatigue damage of the scatter diagram. Subsequently, the scatter diagram fatigue damage can be approximated by only performing a load analysis on these lumped sea states, instead of every sea state in the scatter diagram. This practice results in a large reduction of computational time, at the cost of a small fatigue damage error.

In previous research, lumping methods have been tested on several offshore structures (including monopiles), but no studies could be found on non-axisymmetric floating turbines. This study will evaluate the accuracy and the reduction of computational time of four existing lumping methods when applied to a semi-submersible.

It is concluded that the Katsikogiannis lumping method most consistently shows a high accuracy and a high reduction of computational time. This is due to the fact that for a semi-submersible, a large range of internal stress frequencies may significantly contribute to the fatigue damage. These different frequencies are best captured by the frequency domain load calculation, used by the Katsikogiannis method to estimate the fatigue damage.

Preface

Dear reader,

The document I hereby present as my master's thesis is entitled an 'Examination of environmental lumping methods for fatigue assessment of floating wind turbines'.
After finishing my bachelor in Mechanical Engineering, I decided that during my future career, I wanted to contribute to the development of green energy technologies. The European Wind Energy Master provided me the opportunity to study wind energy at DTU in Copenhagen, NTNU in Trondheim and UNIS in Longyearbyen, as well as the TU Delft. During the two-year program, I met many international students, who taught me about their home countries and about their cultures. Because of this, I learned about the world, almost as much as I learned about wind turbines. For these experiences, I feel very grateful.

My interest in floating wind turbines grew as I discovered how much research still had to be done, could this technology be applied on a larger scale. I envisioned that floating wind turbines would be installed further at sea, preventing visual pollution at shores and beaches, while also allowing green energy to be harvested at places with deeper sea levels. For this reason, I was incredibly excited to hear that Siemens Gamesa Renewable Energy, being one of the experts on floating wind, selected me to provide guidance during my thesis project.

Several people have been of great value and support during my journey. First of all, I would like to thank my Siemens supervisors. Anastasios, whenever I experienced set-backs during the process, you were there to support me and to inspire me. Thank you for your enthusiasm, for your constructive feedback and of course, for sharing your extensive knowledge on offshore wind turbine dynamics with me. Jasper, in my experience, you were able to explain almost any question or unforeseen result. Thank you for sharing your expertise with me and for your critical thinking and questioning that allowed me to raise my study to a higher level. Furthermore, I would like to express my gratitude to all other colleagues at Siemens for their support, insights and critical questions.

Throughout my thesis, I have been supported by my supervisors Erin Bachynski-Polić from NTNU and Eliz-Mari Lourens from TU Delft. Erin, I could turn to you for any question on SIMA and floating wind turbine dynamics. Thank you for your expertise, that has served as a pillar for much of this study. Eliz-Mari, as you were less involved with the day-to-day work of my thesis, you looked at my work from a refreshing perspective. Thank you for your critical observations and questions, that allowed me to deliver a higher quality of work.

In addition, I would like to thank George Katsikogiannis, whose work on a monopile has served as an important base to my study. Thank you, George, for our meetings and for the time and energy you spent to explain your methods, to answer my many questions and to unfold your train of thought.

Finally, I would like to thank my family and my friends for supporting me when I experienced set-backs, for proofreading, and for staying so desperately determined to understand what exactly I have been working on.

Aaron Henskens
Delft, October 2023

Table of Contents

List of Figures

List of Tables

1 Introduction

Floating turbines constitute a new field of research within offshore wind, a young industry itself. For bottom fixed turbines, the material cost is the limiting factor that prevents these turbines from being installed at sea depths larger than 60 m [1]. As floating turbines are anchored by mooring lines or tension legs instead of a fixed structure, this limiting factor can be neglected. They can therefore be installed at much larger sea depths.
Nonetheless, during the design phase, turbine developers encounter long computation times when calculating the extent to which a turbine can withstand a lifetime of cyclic loads due to wind and waves. Methods exist to decrease the computational time, but often they decrease the accuracy of the computation as well. This may result in material failure earlier than expected, potentially causing dangerous situations for humans and economic loss. On the other hand, the turbine might be overdesigned, resulting in higher material costs or a lower lifetime expectancy than necessary. This introduction will expound this problem and aims to clarify the relevance of the research question of this thesis:

What lumping method approximates the fatigue damage at the tower base of a non-axisymmetric floating wind turbine best, while simultaneously decreasing computational time?

1.1 Relevance of deep sea wind energy harvesting

The International Renewable Energy Agency (IRENA) investigated the capacity of offshore renewable energy needed from 2030 to 2050 to prevent exceeding the 1.5°C global warming target. Their estimation can be reviewed in Figure 1, showing a large increase in offshore wind.

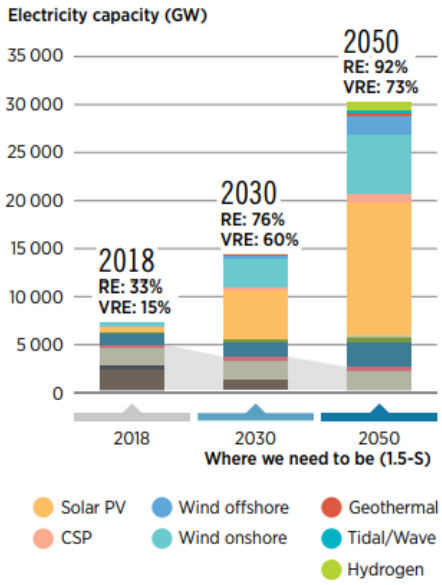

Figure 1: Estimated growth of offshore energy capacity [2]

As shown in Figure 2, the near-coast water depth varies widely around the globe. Given that bottom-founded offshore turbines are typically installed at a maximum water depth of 60 m

[1], the North Sea is particularly suitable for these structures. Nevertheless, in regions like the west coast of the U.S.A., the Mediterranean Sea and the Japanese Sea, the water depth is far larger. Here, floating turbines could offer a solution.

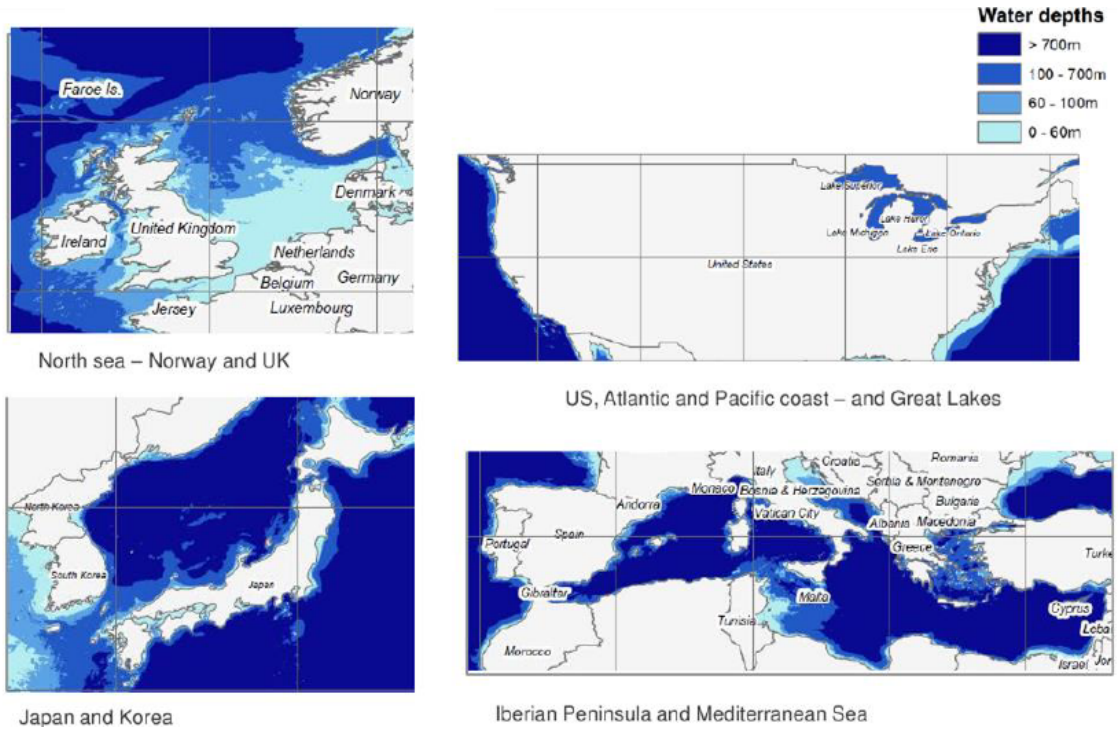

Figure 2: The water depth at different coasts around the globe [3]

1.2 Functionality of floater designs

To retrieve energy from the wind, the overturning moment caused by the thrust force exerted on the rotor, must be resisted. One of the main goals of the turbine foundation is to provide stiffness to prevent the turbine from tipping over.
The monopile and jacket foundation are bottom-founded structures. The stiffness provided by bottom-founded structures consists of material stiffness and the stiffness of the seabed, to which the foundation is attached.
For turbines not fixed to the seabed, a different mechanism must be employed to achieve static stability. Generally, this can be done in three ways [4], as described below.

- **Mooring line stabilized:** The tension leg platform, also called the TLP, is fixed to the sea bed using tension cables. The system of tension legs is the main source of stiffness in all directions. Installation of a TLP is more complex than a spar or semi-submersible as the tension legs require an anchor capable of resisting a vertical force component, causing the risk of the anchor being pulled out of the seabed. The need for applying the right amount of tension to the cables complicates the installation process as well.

- **Ballast stabilized:** The counterweight at the bottom of the spar stabilizes the system and provides stiffness in roll and pitch direction. Its catenary mooring system limits drifting-off and yaw motions. A spar floater experiences smaller and slower motions compared to a semi-submersible. Yet, its centre of rotation is located far below seawater level (SWL), which causes the rotor nacelle assembly (RNA) to

experience larger motions. In addition, a spar requires a large water depth due to its large draft [5].

- **Buoyancy stabilized:** When the buoyancy forces act on the structure far from the centreline (as for a semi-submersible or a barge) the area moment of inertia at the waterline provides stiffness in roll and pitch direction. The catenary mooring system limits the system in drifting off and yawing.

Figure 3 shows these three foundation types. More floating foundation designs exist, but so far the most well-known designs are all based on one or more of the principles described above.

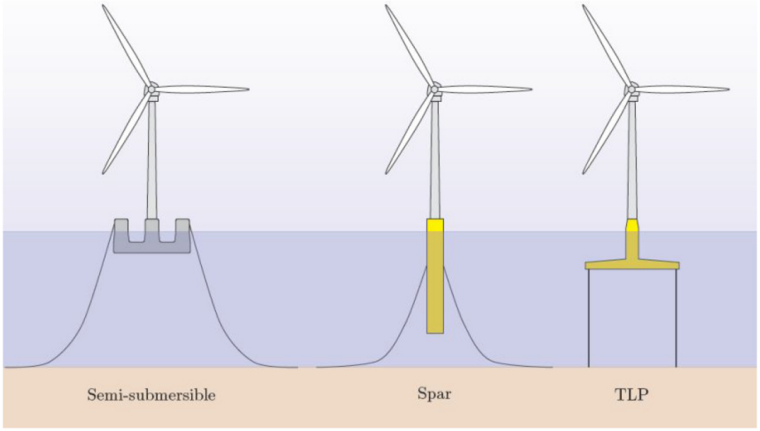

Figure 3: Foundation types for offshore wind turbines [6]

When designing a floating wind farm, the investor has the choice between different types of floaters that have been designed over the last few years. Be as that may, when proposed the question which design is best, the turbine developer may not be able to give a definite answer [7]. The bottom-fixed monopile has been most prominent in recent years, as shown in Figure 4, and most research has been done on this foundation type. Due to differences in hydrodynamics and in the tower/monopile eigenfrequency, it should not be assumed that research on monopiles can be one-to-one applied to floating designs. This topic will be expounded in Section 1.5.2 (based on this thesis' literature study) and in Section 5.2.2 (based on this thesis' findings).

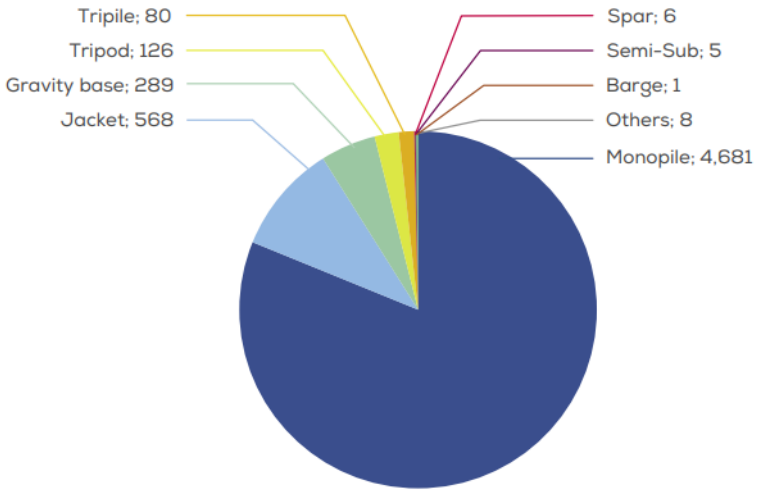

Figure 4: Offshore wind turbine foundations installed at the end of 2020 [8]

1.3 Design phase problem of floating turbines

Fatigue damage describes the initiation and propagation of small cracks in the material, due to cyclic loading, and is quantified as a value between zero and one; where zero represents the absence of any fatigue damage and one represents material failure. Fatigue damage is one of the governing factors during the design phase of offshore floating wind turbines [9]. This is because of the repeated load cycles caused by waves and wind. To analyse fatigue damage, an accurate and efficient model is required in order to compute the internal forces at the most vulnerable locations of the structure.
Compared to the oil and gas industry, the profit margins of offshore wind are small. A floater design that is over-conservative regarding its lifetime fatigue damage is therefore likely to involve a higher material use than necessary, leading to higher costs. Due to the small profit margins, an accurate fatigue analysis is needed to design a structure that has sufficient strength to prevent failure, while at the same time avoiding excessively exceeding the required strength. [10]

1.3.1 Fatigue damage analysis

Fatigue analysis of offshore wind turbines for commercial projects in the industry is generally done according to the following steps.

1. **Hindcast dataset:** The weather conditions at the chosen site for the wind farm are measured for multiple years. This dataset is called the *hindcast*. A hindcast generally shows the data for the variables wind speed, wind direction, wave height, wave period and wave direction (for total sea, wind waves and swell). This data set usually has time steps of 1 hour to 3 hours.

2. **Scatter diagrams:** The wind speed range of the hindcast data set is determined. For each wind speed, a scatter diagram of sea states is created. It is recommended by industry standards to use wind bins of 1 m/s to 2 m/s. For every wind speed bin, all data points are collected. For each combination of wave height H_s and wave period T_p, the number of occurrences for this specific wind speed bin are counted. Next, the

T_p and H_s are binned and a scatter diagram is created. An example of such a scatter diagram is given in Figure 5. If additional parameters like wind-wave misalignment are included, a scatter diagram may be made for every parameter combination present in the hindcast. For example, a single scatter diagram would contain all (T_p, H_s)-combinations where a wind speed of 8 m/s bin (including wind speeds in the range 7 m/s $< v \leq$ 9 m/s) and a wind-wave misalignment of 0° (using 30° bins, therefore including misalignments in the range -15° $< \mu \leq$ 15°) were measured. Doing so, will result in a larger number of scatter diagrams, each containing less sea states. [11]

3. **Load analysis:** For every sea state in every scatter diagram, a load analysis in time domain is performed. This computation results in time series of the internal forces and moments at a specific location or multiple locations on the floater and/or turbine tower. Using these forces, the time series of the axial and shear stresses can be computed.

4. **Fatigue damage analysis:** Rainflow counting is used to determine how many times every stress range of the different load cycles appear in the stress response. The S-N curve of a material shows the number of cycles needed (N) at a certain stress (S) for material failure to occur. Using the Palmgren-Miner rule as shown in Equation 1, the fatigue damage D can now be calculated. Here, k represents the number of stress bins, S is the magnitude of stress bin i, n is the number of occurrences of stress S as counted by the rainflow analysis and N is the number of occurrences of S that will cause the material to fail as given by the S-N curve. [12]

$$D = \sum_{i=1}^{k} \frac{n_i \cdot S_i}{N_i \cdot S_i} = \frac{n_i}{N_i} \tag{1}$$

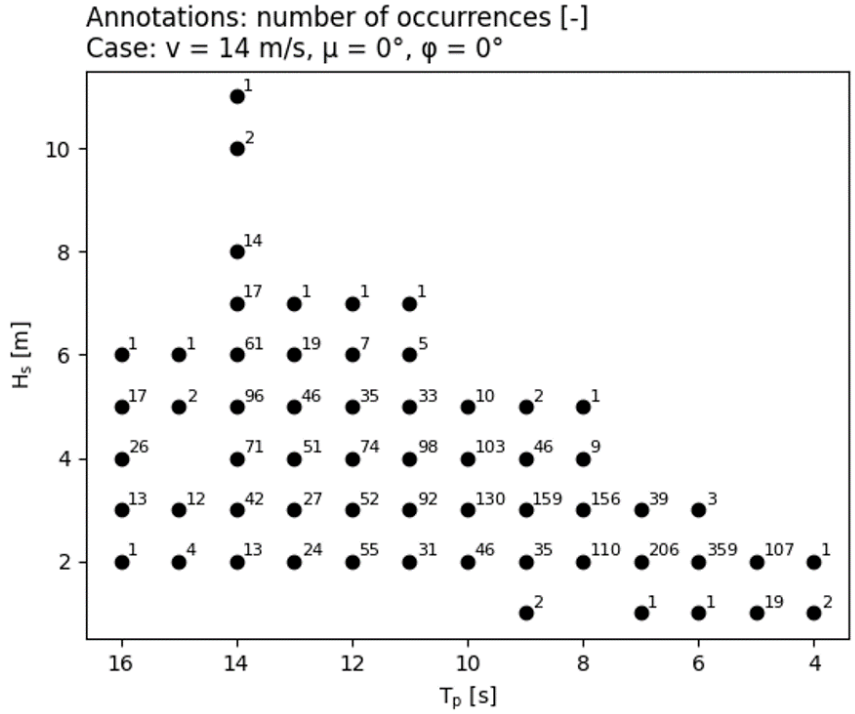

Figure 5: An (T_p, H_s)-scatter diagram at a wind speed v of 14 m/s, a wind-wave misalignment μ of 0° and a floater orientation ϕ of 0°, as measured at the coast of Norway (see Section 2.3). The annotations represent the number of occurrences (NOC) for each sea state.

1.3.2 Computationally intensive time domain simulations

In step 3 of the fatigue damage assessment mentioned previously, a time domain simulation is done for every sea state in every scatter diagram of the hindcast data set. A hindcast data set usually includes wind directions and wind speeds, as well as the wave height, wave period and wave direction of the swell, the wind waves, and the total sea. This may result in more than 10,000 combinations of parameters [13].
For a non-axisymmetric foundation, the number of combinations is even larger than for an axisymmetric foundation. This is due to the fact that for an axisymmetric foundation like a monopile, the number of combinations can be reduced by replacing wave direction with the absolute wind-wave misalignment, as Equation 2 shows.

$$\Delta\theta_{\text{wi-wa}} = |\theta_{\text{wind}} - \theta_{\text{wave}}| \tag{2}$$

This is not possible with a non-axisymmetric floating turbine, as the same wind-wave misalignment for a specific wind direction can result in different loads, depending on the orientation of the floater. This is illustrated in Figure 6. [14]

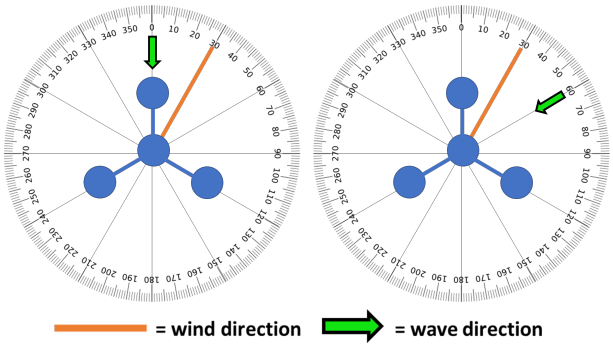

Figure 6: Two 30° wind-wave misalignment with equal wind directions, potentially resulting in different loads on a structure due to the structure's non-axisymmetric shape (top view)

Because the time domain computation of one sea state can last between one and four hours, it would take too much time to compute the entire hindcast for a commercial project, where multiple designs may need to be tested and where deadlines must be met.

1.4 Solution to increase computational speed

This thesis will focus on a method to reduce computational time, called *lumping*, where multiple sea states of a scatter diagram are represented by a single sea state.
Lumping is defined as selecting a representative sea state that results in a fatigue damage, that approximates the average fatigue damage (weighed by the number of occurrences) of the original group of sea states from which the representative sea state is derived. This representative sea state is called the *lumped sea state*.
A *lumping method* is the procedure that selects one or multiple lumped sea state(s) from a scatter diagram.
Assuming only one lumped sea state is selected, the total fatigue damage of the scatter diagram can now be computed by only performing a time domain load analysis of the lumped sea state, and multiplying its fatigue damage with the scatter diagram's total number of occurrences. In this way, the number of sea states to be modelled in time domain is vastly reduced, as the cost of a small fatigue damage error. Naturally, a lumping method is designed to minimize both the computational time and this error.
Using a lumping method to find a lumped sea state is a preliminary step to fatigue damage analysis, done by turbine developers for commercial projects. The construction of the lumping method itself can be defined as scientific research. Table 1 suggests a set of assumptions taken for the lumping method and its resulting lumped sea states.

Lumping method:	Lumped sea state:	
For a specific...	For a specific...	foundation design (e.g., monopile, spar or semi-sub)
For a specific...	For a specific...	(range of) locations on the structure
Regardless of...	For a specific...	turbine's load case (e.g., operational or parked)
Regardless of...	For a specific...	hindcast data set
Regardless of...	For a specific...	scatter diagram within the hindcast data set
Regardless of...	For a specific...	floater orientation
Regardless of...	Regardless of...	small structural changes (e.g., tower diameter)

Table 1: Overview of the recommended conditions for which a lumping method and a lumped sea state should be valid (for example, a lumping method is 'only valid for a specific floater type' and 'valid regardless of turbine's load case')

Depending on the preferences, insights and resources of the researcher and turbine developer, these assumptions may change. A lumping method for which more assumptions are made, is likely to have a higher accuracy, but can be applied to fewer cases.

1.5 In this study

In this thesis, the performances of different lumping methods are investigated. As the research question at the beginning of this chapter implies, the performance of a lumping method is defined by two factors:

- **Reduction of computational time:** Instead of computing the loads of every sea state in time domain, only the lumped sea state needs to be computed. Some lumping methods yield multiple lumped sea states per scatter diagram. Others may require additional time domain load simulations in order to find the lumped sea state. For these reasons, the reduction of computational time may differ per lumping method.
- **Accuracy:** The fatigue damage of a scatter diagram is computed using Equation 3, where N_{ss} is the number of sea states in a scatter diagram, D_i is the fatigue damage and n_i is the number of occurrences corresponding to sea state i. A lumping method approaches this fatigue damage, using Equation 4, where N_{lss} is the number of lumped sea states yielded by the lumping method. Often, N_{lss} is equal to 1. In that case, n_k is equal to the total number of occurrences of the scatter diagram $\sum_{i=1}^{N_{ss}} n_i$. The accuracy of a lumping method is measured by the error between $D_{\text{scatter diagram}}$ and $D_{\text{scatter diagram, lumped}}$. The lower this error, the higher the lumping method's accuracy. The formula of this error is given by Equation 5. This equation shows that in order to determine the error, a time domain load computation of every sea state of the scatter diagram is needed, as well as time domain load computations of the lumped sea states. For this reason, the accuracy of a lumping method depends on the following factors:
  - The turbine and floater model used in the time domain simulation (in this study a semi-submersible, see Section 1.5.2);
  - The location on the turbine or floater where the fatigue damage was computed (in this study at the tower base, see Section 1.5.3);
  - The load case (this study will assume the operational load case, as a wind turbine is operational about 70% to 80% of its lifetime [15]);
  - The environmental data set that was used (see Section 1.5.4).

These assumptions are much more limiting than the assumptions for a lumping method given in Table 1. This will be taken into account in the conclusion in Section 7.4, where the conclusion of this thesis will be generalized for the assumptions in Table 1.
Figure 7 visualizes how the evaluation of lumping method accuracy will be performed in this study. Using Equation 5, the error between the fatigue damages resulting from the fatigue analysis based on every sea state in the scatter diagram, and based on the lumped sea state(s) only, is checked. The smaller the error, the more accurate the lumping method.

$$D_{\text{scatter diagram}} = \sum_{i=1}^{N_{ss}} D_i \cdot n_i \tag{3}$$

$$D_{\text{scatter diagram}} \approx \sum_{k=1}^{N_{lss}} D_k \cdot n_k = D_{\text{scatter diagram, lumped}} \tag{4}$$

$$\text{error}_{\%} = \frac{D_{\text{scatter diagram, lumped}} - D_{\text{scatter diagram}}}{D_{\text{scatter diagram}}} \cdot 100\% \tag{5}$$

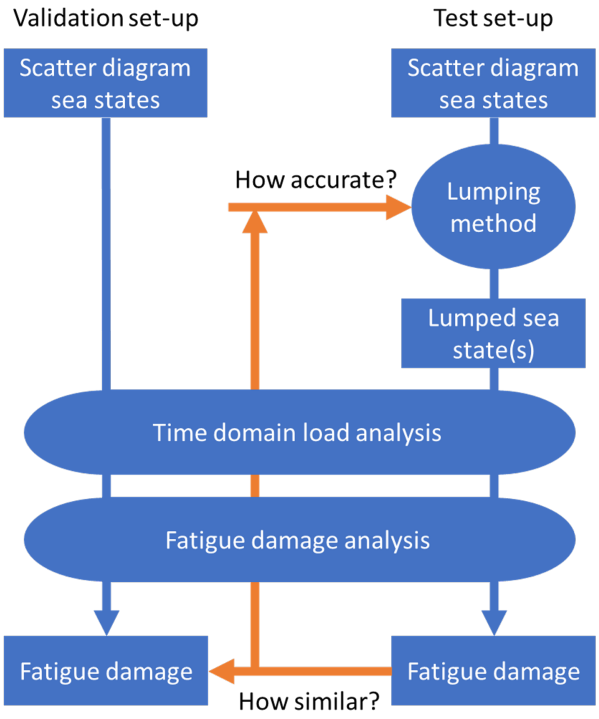

Figure 7: The validation set-up (computing Equation 3) and the test set-up (computing Equation 4) used to evaluate lumping method accuracy

Performing a time domain load analysis for every sea state in a scatter diagram is time-consuming. In previous research, computing the fatigue damage error was approached in the following two ways:

- The error was computed for a single scatter diagram. This method saves time. Yet, the error of a single scatter diagram might not be sufficient to guarantee the same accuracy for the other scatter diagrams in the hindcast.

- The error was computed for all scatter diagrams in the hindcast [16]. While being extremely computationally intensive, this is a robust method to study the performance of a lumping method for a large range of weather conditions.

In this thesis, a compromise between these methods is used, as a sensitivity study will be performed on the variables wind speed, wind-wave misalignment and floater orientation. By computing the error for a wide range of weather variables, the aim is to better predict the accuracy of the lumping methods when applied to the entire hindcast, than when only a single scatter diagram is computed. The choice of scatter diagrams will be discussed in Section 1.5.5.
The selection of the lumping methods that will be tested in this study is based on their high accuracy demonstrated in previous research. The selection of the lumping method will be discussed in Section 1.5.1.
Section 1.5.2 will show that the dynamics of a monopile, spar and semi-submersible differ, and will justify the choice for the semi-submersible model used in this study. Until now, almost every study on lumping methods has been performed on structures other than floating turbines. This study should to contribute to closing this knowledge gap.
For that, three subquestions must be answered (the first subquestion can be split into two):

1. What factors determine the accuracy of a lumping method?
   (a) Which hydrodynamic factors influence the fatigue damage gradient at tower base most for a semi-submersible? (Answered in Section 4)
   (b) Which hydrodynamic model is assumed by the lumping methods? (Answered in Section 5)
2. What is the performance of the four lumping methods when applied to a semi-submersible? (Answered in Section 6)

It must be noted that questions 1a and 1b focus on hydrodynamic factors, as H_s and T_p are being lumped and wind speed v is constant for the scatter diagram. In addition, question 1a refers to the *fatigue damage gradient* instead of the fatigue damage. The reason for this will be discussed in Section 5.2. Note that question 2 assesses the performance of the lumping methods, thereby studying both their accuracy and reduction of computational time. The time domain model and the fatigue damage calculation used to answer these questions will be discussed in Part I. Lastly, Section 7 will give a final recommendation which (if any) of the four lumping methods can be applied to semi-submersible model used in this study, and will discuss to what extent this conclusion can be generalized for non-axisymmetric floating turbines.

1.5.1 Choice of lumping methods: Jia, Song & Wang, Seidel and Katsikogiannis

Previous research studied lumping methods for several types of marine structures, like mooring and riser systems, bottom-fixed offshore wind turbines, fixed and floating platforms and fish cages. In addition, comparison studies were performed on the fatigue damage error of these lumping methods. Only one study was found that applied a lumping method to a floating turbine. This study did not test the accuracy of this method.
This thesis aims to compare multiple lumping methods based on significantly different hydrodynamic models, that performed well in previous research. The choice of the four

selected methods will now be justified.
The Hou et al. paper [17] from 2019 compared several block partitioning lumping methods. Block partitioning is a method, where the scatter diagram is divided into blocks. For each block, a lumped sea state is found. A block partitioning method has the following disadvantages:

- There is no recommended method to perform block partitioning. Block partitioning is performed differently in various studies, and often no reasoning behind the choice of the block partitioning is provided.
- The accuracy of the lumping method is sensitive to the way that you are splitting the scatter diagram into blocks, especially around the T_p that is close to the structure's natural period. A very different accuracy can be found for different block partitionings.
- A block partitioning lumping method yields multiple lumped sea states per scatter diagram, and therefore often requires more computational time than a non block partitioning method.

In the Hou et al. study, the errors were computed for a bridle line, grid line and a buoy line. A block partitioning of 16 blocks per scatter diagram was used (with 4 to 12 sea states per block) and the loads on the lines were computed in time domain. The four best performing lumping methods from the Hou paper are shown in Table 2. These methods showed an average (for different lines and block partitionings) fatigue damage error lower than 30%. Table 2 is only provided to give a clear overview of the best performing combinations of lumping methods, and does not show exact errors, as the original paper only provided graphs.

Lumping method used to find H_s:	Lumping method used to find T_p:
Jia [18]	Sheehan [19]
Song & Wang [20]	Song & Wang [20]
Song & Wang [20]	Sheehan [19]
Song & Wang[20]	Kühn [21]

Table 2: Best performing lumping methods of the Hou et al. study [17], with an average error lower than 30% for all mooring lines

The Song & Wang method has a predecessor, that will be referred to as the Song method, that lacked the correction factor regarding the number of sea states per block that was applied in the Song & Wang method. The errors from the comparison in the Song paper from 2016 [22] are given in Table 3. These results were obtained using a time domain load calculation, rainflow counting and the Palmgren-Miner rule to compute the fatigue damage. The fatigue damage was computed at the platform of a monopile. It must be noted that the lumping method recommended by the DNV standard showed a relatively high inaccuracy. In the Hou comparison, the Sheehan method (when used for both the T_p and H_s) showed an extremely high error as well (between 200% and 850% for the different blocks of a block partitioning of 16 blocks).

Lumping method:	Error:
DNV	64.4%
Sheehan	109%
Jia	-5.10%
Song	8.40%

Table 3: Errors computed by the Song paper [22] for a monopile platform

When the improved Song & Wang method was applied to a fixed jacket structure and to the mooring lines of a semi-submersible, a slight underestimation by the Jia method and a slight overestimation of the fatigue damage by the Song & Wang method was observed [20]. The error did not seem to get larger than 20% and was often smaller than 5% (mostly figures were shown in the paper, so no exact values could be derived). The Song & Wang paper [20] noted that regarding the preference for a conservative fatigue damage calculation, a lumping method that consistently slightly overestimates the fatigue damage is preferred over a slight underestimation. In this case, the Song & Wang method would be preferred over the Jia method.
The Low & Cheung study [23] from 2012 compared a selection of statistical lumping methods and one block partitioning method close to the Sheehan method. The Sheehan method resulted in the highest error of 84.8%. A statistical method called importance sampling gave the lowest error of 0.4%. A frequency domain analysis, that had been validated against time domain simulations, was used to compute the loads. The study was performed on mooring lines and risers.
In the Passon study from 2015 [24], a contour line method (further studied by George Katsikogiannis [16] [9], and in this study referred to as the Katsikogiannis method) was compared to the Seidel method [25] and the Kühn method [21]. The Passon/Katsikogiannis method yielded an almost 0% error, while the Seidel and Kühn method resulted in an error of about 25% (the study only showed graphs, so no exact values could be derived).
These studies show that a fatigue damage error of less than 30% is a reasonable expectation for a lumping method. Any lumping method with a higher error can likely be disregarded. Yet, these studies show that an error lower than 5% may be achieved, when the (hydro)dynamic factors accounted for by the lumping method equal the (hydro)dynamics that influences the fatigue damage gradient of the structure that is being modelled. Based on the previous research described above, potential lumping methods to study are:

- **The Jia method [18]:** This is a block partitioning method, where the lumped sea state of each block is determined by assuming fatigue damage gradient can be estimated using the hydrodynamic force, as computed by the inertia term of the Morison's equation. The method involves a few straightforward formulas and therefore is easy to apply.

- **The Song & Wang method [20]:** This is a block partitioning method, that assumes that the lumped sea state's zeroth spectral moment (also called the spectral energy) raised to the power of two, is equal to the weighed average (based on the probability of occurrence (POC)) of the zeroth spectral moment raised to the power of two of the entire block. This method is relatively straightforward to apply.

- **The Importance Sampling method (by Low & Cheung) [23]:** Random sea states are drawn from a pool containing all sea states in the hindcast. These random sea states will be treated as the lumped sea states of this lumping method. During importance sampling, the sea states that influence the fatigue damage most, appear in the pool

most frequently (this is called the importance sampling density) and therefore have a higher probability of being drawn. No suggestion was given on how to compute the importance sampling density. Because of this, it is unknown if (and if so, how many) time domain simulations were needed to compute the importance sampling density, yielding the small error of 0.4%.

- **The Kühn method [21]:** The fatigue damage due to aerodynamics is computed using a time domain load simulation for every wind case. Using the aerodynamic damping coefficient and the hydrodynamic matrices, a transfer function is constructed to compute the axial stress for any given wave spectrum. These stresses are used to estimate the fatigue damage for each sea state. An iterative method is proposed to select the lumped sea state.

- **The Seidel method [25]:** It is assumed that the damage equivalent loads are proportional to the square root of the wave spectral density at a specified frequency. The fatigue damage is equal to the damage equivalent loads raised to the power of m, where m is the slope of the S-N curve. Knowing the estimated fatigue damage for each sea state, the lumped sea state can be selected using Equation 3 and Equation 4.

- **The Passon/Katsikogiannis method [24] [26] [16] [9]:** It is assumed that the fatigue damage can be approximated using a frequency domain method. A white noise load simulation is run in time domain. Then the transfer function relating the white noise wave spectrum to the resulting internal axial stresses is computed. Using this transfer function, the axial stresses can be computed for any given wave spectrum and the fatigue damage can be computed. Knowing the estimated fatigue damage for each sea state, the lumped sea state can be selected using Equation 3 and Equation 4.

The importance sampling method was disregarded due to the lack of information on how to derive the importance sampling density. It is uncertain how valuable this method is, as no information is given in the paper on the number of time domain simulations needed to derive a density, that lead to such a small error. The Kühn method and the Katsikogiannis method were similar in the fact that they both use a frequency domain load analysis to estimate the fatigue damage. As the Katsikogiannis method resulted in a much smaller error, the Katsikogiannis method was chosen over the Kühn method. The Jia and Song & Wang method consistently showed low errors in multiple studies, when applied to different structures. Even though both are block partitioning methods, they are based on different physical principles, making both of them an interesting candidate to study.
Jia and Song & Wang are both block partitioning methods, yielding multiple sea states per scatter diagram, and the Katsikogiannis and Kühn method require an extra time domain load simulation. In contrast to these four methods, the Seidel method achieved a low error without the use of an extra time domain load simulation, while also yielding just one lumped sea state. For this reason, the Seidel method could potentially have the highest reduction of computational time of all lumping methods studied, while still showing a low error. Therefore, the Seidel method was selected to study as well.
In conclusion, for the reasons described above, the Jia, the Song & Wang, the Seidel and the Katsikogiannis method were selected to be studied in this thesis.

1.5.2 Choice of floater design: semi-submersible floater

The research question of this thesis defines that a non-axisymmetric floater will be studied. Yet, as Section 1.5.1 stated, almost no lumping method research has been performed on any type of floating turbine. Because of this, it could be questioned, why this study focusses on a non-axisymmetric design specifically.
In the literature study [27] done in preparation to this thesis, the hydrodynamics of a fixed turbine (monopile), a floating axisymmetric turbine (spar) and a floating non-axisymmetric turbine (semi-submersible) were studied. The main findings were the following:

- For any wind-wave misalignment, a spar experiences an increase in fatigue damage if the wave height is increased. For a semi-submersible, this depends on the wind and wave direction with respect to the floater. [28]
- For a spar, the maximum fatigue damage at the tower base circumference aligns with the wave direction. For a semi-submersible, the non-axisymmetric shape causes the floater dimensions to interact with the wave length for certain wave directions. This causes an increase in wave loads. For these wave directions, the maximum fatigue damage may align with the wave direction. For other wave directions, the maximum fatigue damage tends to align with the wind direction. Such an increase in wave loads at a specific wave direction does not occur for an axisymmetric floater like a spar. [28] For the same reason, the hydrodynamic forces are expected to be the same for every wave direction for a monopile.
- If the wave direction is as such that all four semi-submersible columns experience frontal waves, the fatigue damage at tower base is highest. A channel effect, where the two front columns push water towards the centre column, increases the fatigue damage even more. At other wave directions, the waves break against the single frontal column, after which they tend to 'slip' between the columns behind. In this case, the fatigue damage is much lower. [29]

These studies show that for a semi-submersible the relation of the wave height, wave frequency and wave direction to the fatigue damage is specific to its non-axisymmetric shape. For this reason, research on lumping methods for floating turbines must take the different dynamics of an axisymmetric and non-axisymmetric floater shape into account. A lumping method that works for a spar, might not work for a semi-submersible. As almost all lumping method research has been done on an axisymmetric (fixed) turbine foundation (namely, a monopile), a study on a non-axisymmetric foundation seemed most relevant.
As Figure 4 shows, the most commonly installed non-axisymmetric floater is the semi-submersible. For this reason, a semi-submersible was chosen as the floater design for this study. Section 5.2.2 will discuss more key differences (regarding its structural natural frequency and the relation between wave excitation and the frequency range of the internal stresses) between a monopile and a semi-submersible, using the results found in this study.

1.5.3 Choice of fatigue damage location: tower base interface

As Figure 8 shows, different locations along the tower experience a different fatigue damage. In this experiment [30], a high fatigue damage was found at tower base and at a 60 m height. The high fatigue damage at the tower base is due to the fact that the standard deviation of the M_y and M_z moments (see Figure 16 for the orientation of the

axes) is highest at this point. Due to the geometry of the tower, the standard deviation of the internal stress in z-direction is highest at 60 m. The mode shapes of the tower can influence the location of the maximum fatigue damage as well. [30]

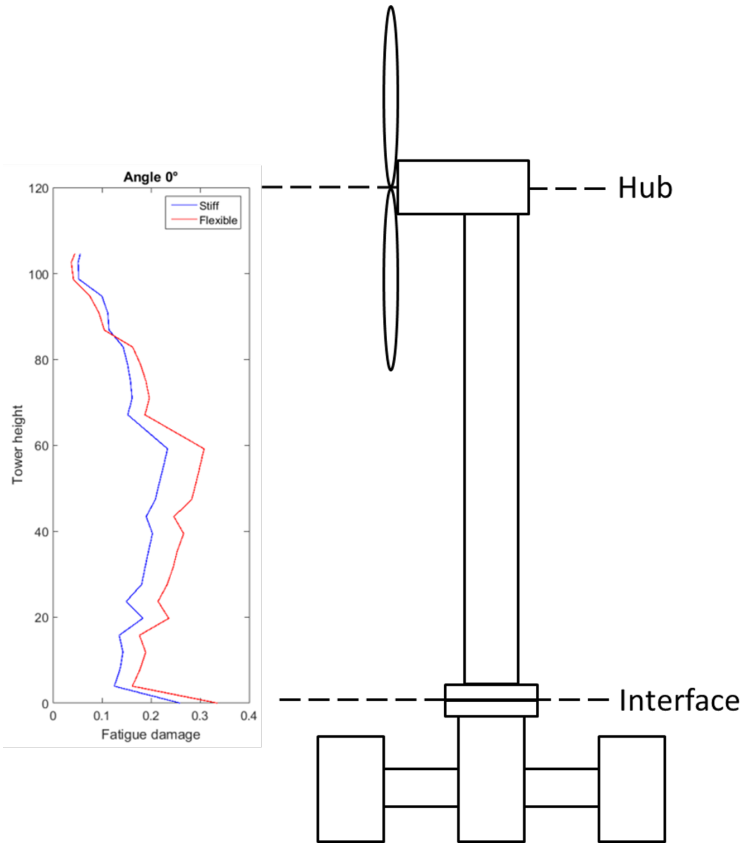

Figure 8: Change in fatigue damage along the tower of a semi-submersible wind turbine [30]

The high fatigue damage at 60 m is highly related to the geometry of the tower. A high fatigue damage somewhere midway the tower is most likely experienced at different heights for different turbines and may be less pronounced in some cases. At the tower base, the mean and the standard deviation of M_y and M_z are maximum for most designs. In addition, in real life the tower base is located at the interface, where the tower is bolted or welded to the floater. This connection may be less resilient to many and/or high load cycles than the solid material of the tower. For these two reasons, the tower base seemed to be a better choice to study in this thesis.
Other locations of interest could be welds between the columns and pontoons of the floater and the connection between the floater and the mooring lines. These locations may experience different dynamics from the tower, and therefore the fatigue damage might be different. Yet, for these reasons, a study on these locations for a semi-submersible may be hard to compare to results from previous studies on monopiles. Being able to compare the results from this study to studies on monopiles helps to identify differences or similarities in the causes for fatigue damage of a monopile and a semi-submersible. Much research has been done on monopiles. Knowledge of these differences and similarities may provide insight into whether any research done on monopiles might (partially) be applicable to semi-submersibles as well.
For these reasons, the tower base (at the interface) was chosen as the location studied in this thesis.

1.5.4 Choice of hindcast data: total sea

There are no factors regarding the hindcast that could reduce the validity of this study's result, except for the fact that the hindcast must preferably be measured at a site that is considered suitable for a wind farm. The used environmental data set is described as site 14 in a 2015 paper by Li et al. [31]. The data were measured in one-hour periods starting in January 2001 and ending in December 2010, at a location near the Norwegian coast, as shown in Figure 9. The location had a water depth of 202 m and a distance to shore of 30 km. [31]

Figure 9: Location where hindcast data was measured

This hindcast contained three sets of waves: 'total sea', 'wind waves' and 'swell'. Using multiple wave sets (both 'wind waves' and 'swell waves') was considered as the most accurate way to model the sea state. Close to no research was found on applying lumping methods on environmental data containing both wind waves and swell. Katsikogiannis [11] made a suggestion on this matter, which can be reviewed in Appendix H. As research on this topic has not been performed, it was decided to model a single set of waves.
Next, a choice between the 'total sea', 'wind wave' and 'swell' set of waves had to be made. As the swell and the wind waves are components of the total sea, the total sea wave set was the natural choice, as it most accurately represents the wave set that is experienced by the semi-submersible. Yet, as developers might wish to separate the wind waves and swell in their load simulation, one might want to lump the wind waves and swell, instead of the total sea wave set. For this reason, a short overview will now be provided of the differences between these three wave sets for this particular hindcast.
Histograms were made that depicted the distribution of different wave periods, wave heights, wave directions and wind-wave misalignments of the three wave sets, as shown in Figure 10.

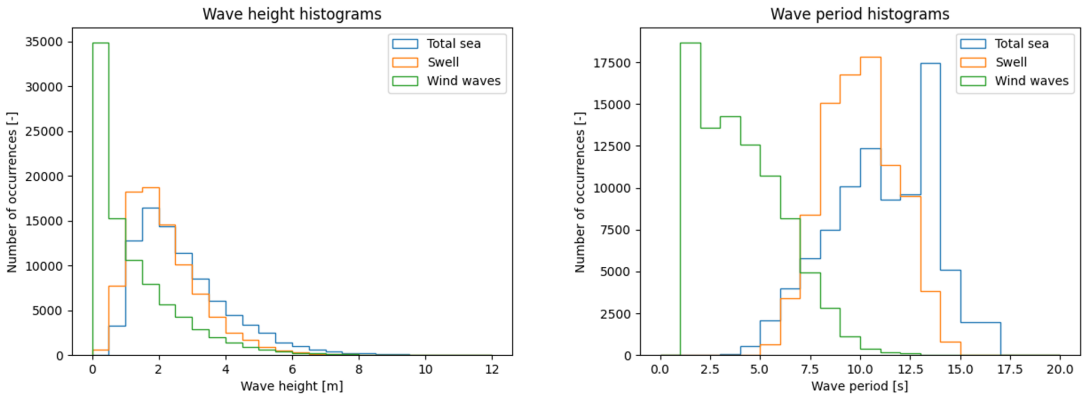

(a) H_s distributions

(b) T_p distributions

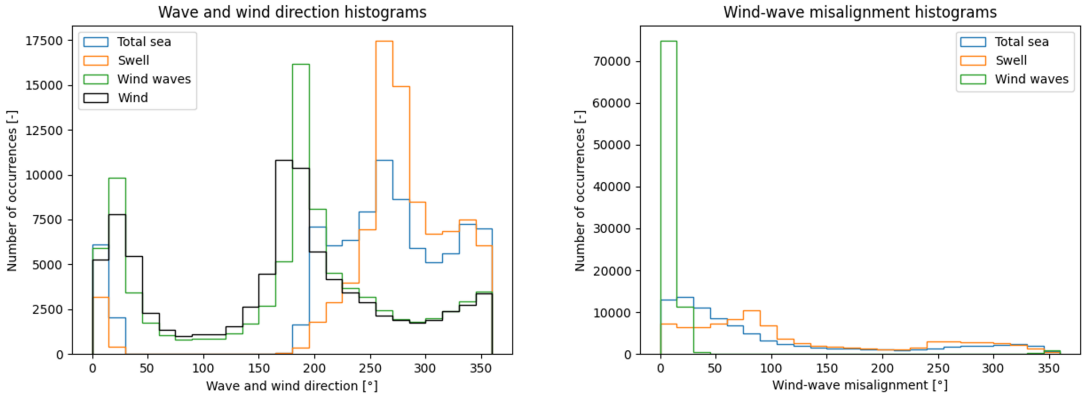

(c) Wind and wave direction distributions

(d) μ distributions

Figure 10: Histograms displaying the number of occurrences observed in the hindcast for different ranges of several hindcast parameters, for the three sets of waves

As wind waves are produced by the wind, they generally have a lower wave period and wave height than the swell and total sea and have a higher tendency to align with the wind direction. This is shown in the histograms for this hindcast as well. Figure 10.b shows that the wave period range of the wind wave set overlaps the tower natural period of the semi-submersible used in this study, of 2.39 s (as will be discussed in Section 2.4.2). This study will show that whether or not the tower natural frequency lays within the wave range of the wave set to be lumped, may affect the accuracy of a lumping method. Section 7.4 will discuss matter, based on the findings of this study.

For the total sea and the swell, the main wave direction ranges from 250° to 350°, coming from the west. This is most likely due to the shore located 30 km away in the east.

Because of this, the total sea and swell show a larger range of wind-wave misalignments. Previous research [28] has shown that a semi-submersible experiences different dynamics and therefore a different fatigue damage for larger wind-wave misalignments. As will be shown in this study, the presence or absence of large wind-wave misalignments may affect which lumping method is most suitable to use for the given wave set. Again, this will be discussed in Section 7.4.

1.5.5 Choice of scatter diagrams

Based on previous research, the following sensitivity studies were chosen (also shown in Figure 11).

- **Wind speed sensitivity study:** A wind speed sensitivity study was chosen, as the wind speed affects the damping of the system and influences the stress ranges experienced by the turbine due to turbulence. In addition, a high wind speed correlates with a higher average T_p and H_s, which may influence the fatigue damage as well. A wind speed of 6 m/s (slightly above the cut-in wind speed of 3 m/s), 14 m/s (slightly above the rated wind speed of 10.59 m/s) and 22 m/s (slightly below the cut-out wind speed of 25 m/s) were chosen. The aim was to cover the full range of wind speeds, where the turbine is operational. Wind speeds close to but not exactly equal to the cut-in, rated and cut-out wind speeds were chosen to prevent inexplicable results due to unpredictable controller behaviour. [32]
  The wind-wave misalignment and floater orientation were set to 0° for all cases.
- **Wind-wave misalignment sensitivity study:** A 2014 study by Bachynski et al. [28] shows how different wind-wave misalignments result in different dynamics and therefore a different fatigue damage, experienced by a semi-submersible. For this reason, this thesis conducts a wind-wave misalignment sensitivity study. Based on the 2014 study, wind-wave misalignments of 0°, 30°, 60° and 90° were chosen.
  The wind speed was set to 14 m/s [32] and the floater orientation was set to 0° for all cases. The wave direction was constant for all wind-wave misalignments and was set to 0°.
- **Floater orientation sensitivity study:** A 2020 study by Zhou et al. [29], shows how different floater orientations with respect to the wave direction result in different dynamics and therefore a different fatigue damage experienced by a semi-submersible. For this reason, this thesis performs a sensitivity study on floater orientation. Based on the 2020 study, floater orientations of 0°, 30° and 60° were chosen.
  The wind speed was set to 14 m/s [32] and the wind-wave misalignment was set to 0° for all cases.

A wind speed bin of 2 m/s was used and for the wind-wave misalignment and floater orientation a 30° bin was chosen.
Section 1.3.2 explained that for an axisymmetric floater wind-wave misalignment can replace either wind direction or wave direction to reduce the number of combinations, but that this is not possible for a non-axisymmetric floater. Nevertheless, wind-wave misalignment is used in this study, since the additional variable floater orientation accounts for any difference in loads and fatigue damage that may occur when wind and waves approach the floater from a different angle. The floater orientation is defined as the yaw angle of the floater with respect to the North Pole.
Combinations of different wind speeds, wind-wave misalignments and floater orientations are not computed, as doing so will increase the number of scatter diagrams significantly. If this study shows that the accuracy of lumping methods differs greatly for different wind speeds, wind-wave misalignments or floater orientations, then combinations of these variables can be studied in future research.

Note on implementation
Due to an incorrect implementation of wind directions higher than 0° in the time domain

load analysis model, all affected scatter diagrams (any scatter diagram where $\mu = 30°$, $\mu = 60°$, $\mu = 90°$, $\phi = 30°$ or $\phi = 60°$) had to be declared invalid. For this reason, the wind-wave misalignment and floater orientation sensitivity study could not be performed. **??** will discuss the cause of this error and its implications to the validity of the results in more detail.

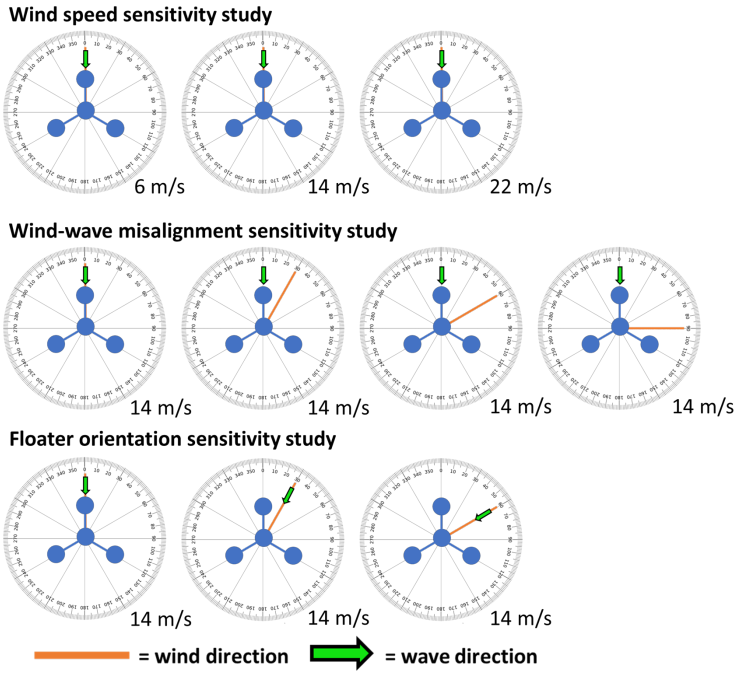

Figure 11: Selected cases to perform wind speed, wind-wave misalignment and floater orientation sensitivity studies

Part I

Fatigue Damage Analysis Model

In order to perform the experiment as shown in Figure 7, a load analysis model is needed that takes a wind and wave spectrum as an input and that yields the internal loads at the tower base as an output. This model will be discussed in Section 2. Next, Section 3 will explain the method used to compute the fatigue damage, using the internal loads as an input.

2 Load analysis model

To set up the load analysis model, several considerations had to be made. The load analysis can be performed in frequency domain or time domain, each having their own advantages and disadvantages, as discussed in Section 2.1. Then, in Section 2.2, the step size of the (time domain) computational model and the simulation length are determined. Section 2.3 will review how the scatter diagrams were constructed and which wind and wave seeds were used. Lastly, the reference turbine and reference floater are described and the time domain load computation model is checked in Section 2.4.

2.1 Comparison of time domain and frequency domain

A load analysis can be done in time domain and frequency domain. Both methods have advantages and disadvantages. For the time domain analysis, the SIMA software [33] (a software for analysis of marine operations and floating systems) was available and for the frequency domain analysis RAFT [34] (a Python package for frequency domain load analysis of offshore wind turbines) was considered.

Advantages ($+$) and disadvantages ($-$) of the time domain analysis:

- $+$ A time domain simulation takes non-linear relations between environmental factors and internal stresses into account. Specifically, it is capable of handling coupling between the wind-induced and wave-induced responses. An example of coupling would be the case when the wind force induces floater motions, which affect the hydrodynamic forces acting on the floater'and the thrust force on the rotor. These coupling effects might be of higher influence to the fatigue damage for a floating turbine than for a monopile, as a floater is susceptible to larger motions. In addition, a time domain simulation is better at modelling the interactions between the rotor controller and the aerodynamics, that affect the thrust force and the pitch motion. For these reasons, a time domain analysis is regarded as a more accurate method to determine fatigue damage, than a frequency domain analysis.
- $-$ Computing a single sea state using a time domain load analysis can take up to one hour. Computational time is reduced when multiple sea states are run simultaneously. Rerunning computations due to small input errors is time-consuming.
- $-$ The SIMA software is a black box. When unexpected results appear, one may be able to figure out the mechanics behind them by analysing intermediate output results, but one cannot check SIMA's computation step by step.

Advantages (+) and disadvantages (−) of the frequency domain analysis:

+ The load analysis of the selected scatter diagrams will take a few minutes at most. The load analysis can be redone easily if mistakes are made.

+ The RAFT script is open source and written in Python. If any unexpected result appears, its source can be deduced, using code debugging tools like breakpoints. Because of this, explanations for unexpected results might be found easier and/or faster, than when a black box software like SIMA is used.

− A frequency domain simulation assumes a linear relation between the wave PSD and the PSD's of the internal loads at the tower base. The motions and loads are not computed for every moment in time. For this reason, non-linear effects may not be computed accurately. For example, aerodynamic damping is a non-linear effect that depends on the motions of the floater and affect the thrust force experienced by the rotor (as explained in Section 4.1 in more detail). When using a frequency domain model, the dependency of the thrust force on the motions can be approximated by computing the position of the floater using iteration.

− Not much research has been done on the validity of the RAFT model when used for fatigue damage computation. A study [35] compared the internal forces and moments at the tower base resulting from RAFT to the ones resulting from a time domain load simulation model. The study concluded that RAFT is not suitable for a fatigue damage computation due to large errors its results showed, compared to a time domain simulation. The full analysis on why the simplifications done in RAFT make the code unsuitable for fatigue analysis, is done in Appendix I.

− The Katsikogiannis lumping method, one of the lumping methods selected to test in this study, is based on estimating the fatigue damage using frequency domain load simulations to find the lumped sea state. When both the validation set-up and the lumping method compute the fatigue damage using a frequency domain load simulation, both assume the same simplifications (linear relation between waves and loads, no or estimated coupling between wind and waves), and a high accuracy is expected for this lumping method. This high accuracy would be misleading as in real life non-linear forces and coupling may occur. In that case, the lumping method might not perform as well.

Considering the advantages and disadvantages stated above, a time domain simulation in SIMA was chosen. The inaccuracy of the frequency domain model RAFT (including the fact that the causes of the inaccuracy are not fully understood due to the lack of previous research) would result in unreliable results. This weighed heavier than the disadvantages of the time domain model.

2.2 Step size sensitivity and simulation length

In order to run SIMA, several time-related parameters need to be set:

- **Simulation length [s]:** The simulation length is defined as the time period for which the loads will be computed. In this study, a 400 s transient period was chosen (this has been checked manually for random cases in this project and is equal to the transient length recommended in a university assignment that performed a similar study [36]).

A transient period describes the time needed for the model to progress from its initial state (based on the model's input values) to a steady state. A sea state is as assumed to stay constant over one to three hours [5]. In accordance with previous research [11] and in agreement with the supervisors of this project [32] [7] [37], it was assumed that a one-hour time series is long enough to capture the statistical properties of the wind and sea state. The 400 s transient and the 3600 s steady state resulted in a simulation length of 4000 s.

- **Time step [s]:** The time step determines at which rate the dynamic and structural analysis is performed. The time step should be small enough to capture the effects that reasonably contribute to the fatigue damage, but should not be smaller, as this will increase the computational time unnecessarily. To find a suitable time step, a small study was performed, shown in Figure 12, where a time step of 0.01 s, 0.02 s and 0.05 s were compared to the smallest time step of 0.005 s. These time steps were derived from the university assignment [36] and in agreement with the thesis supervisors [32] [7] [37]. Considering these results, a time step of 0.02 s was chosen. When increasing the time step, modelling errors can occur at the blade tips at high wind speeds. These modelling errors can cause large load oscillations [32]. This error was ruled out by comparing the mean and standard deviation of the rotor speed, blade pitch, thrust, torque and power of the 0.02 s time step with the 0.005 s time step. In addition, a test was performed around rated wind speed (v = 14 m/s, H_s = 3 m, T_p = 15 s), where the 0.02 s case underestimated the fatigue damage of the 0.005 s case by 1.57%, which was assumed to be acceptable.

- **Time increment [s]:** The time series of the waves and first and second order wave loads are generated in SIMA using a different time step than the structural analysis [33]. This time step is called the *time increment*. The time increment should be small enough to capture the highest frequencies of these parameters. In accordance with the university assignment [36] and in agreement with a thesis supervisor [32], the time increment was set to 0.1 s.

- **Storage step size [-]:** The storage step size represents the step size of the data points that are being stored from the force response time series. Based on a sensitivity study, a storage step size of 1 was chosen. This is the smallest storage step size possible, where every computed time step is stored.

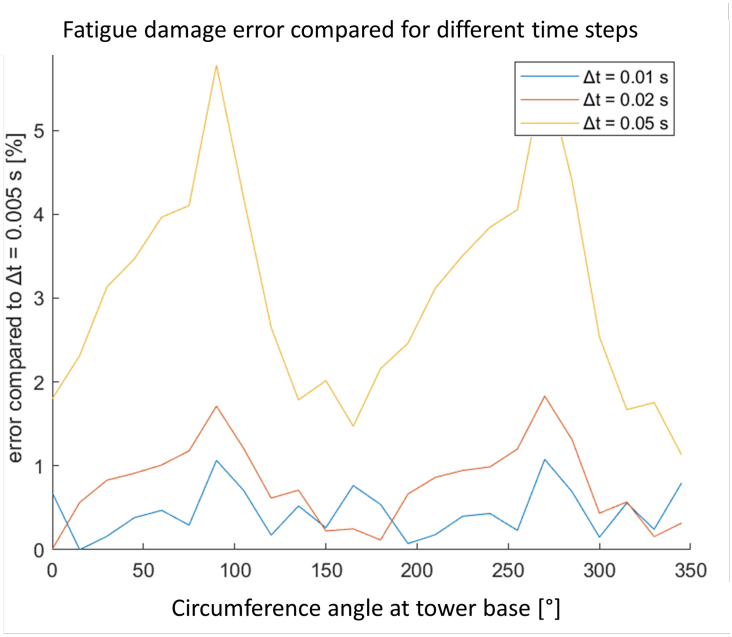

Figure 12: Error [%] for a 0.01 s, 0.02 s and a 0.05 s time step, compared to a 0.005 s time step

Table 4 shows that the computational time decreases as the time step increases, but not necessarily by the same factor. This is likely due to computations that are not dependent on the time step (like the static analysis and the generation of the wave time series), as well as background processes running on the server, that can temporarily slow down the computation. This experiment was performed using the smallest T_p present for the total sea wave set of the hindcast. This is because for a low T_p the error that occurred when increasing the time step, was expected to be larger than for a high T_p. This low T_p was combined with a low H_s and wind speed v in order to create a realistic weather condition.

Time step:	Computational time:
0.005 s	1 hour, 31 minutes
0.01 s	56 minutes
0.02 s	44 minutes
0.05 s	21 minutes

Table 4: Decrease in computational time of SIMA model as time step increases

2.3 Real-life environmental data

The environmental data had to be preprocessed by scaling up the wind speed from a 10 m height to the hub height of 150 m in order to create the scatter diagrams, as described in Section 2.3.1. Section 2.3.2 describes how different wind and wave seeds were applied, in order to compute the wind speed and wave height time series.

2.3.1 Scaling up the wind speed

From the data set, the H_s (total sea), T_p (total sea), mean wave direction (total sea), wind direction and wind speed at 10 m were used in the project. In order to create scatter diagrams for a wind speed at hub height, the wind speed is scaled up. To do this, Equation 6 is used. Here, z_{hub} is the hub height (150 m, see Table 5), z_0 (0.0003 m) is the surface roughness, z_{10} (10 m) is the height of the known wind speed, v_{10} is the known wind speed at 10 m, z_h (0 m) is the zero plane displacement which is the height above ground where the zero mean wind speed is achieved due to flow obstacles, and v_{hub} is the wind speed at hub height. [38]

$$v_{\text{hub}} = v_{10} \cdot \frac{\ln\left(\frac{z_{\text{hub}} - z_h}{z_0}\right)}{\ln\left(\frac{z_{10} - z_h}{z_0}\right)} \tag{6}$$

Scatter diagrams were created by filtering the hindcast on wind speed (2 m/s bin) and wind wave misalignment (30° bin) for the selected cases, as presented in Figure 11. The scatter diagrams are shown in Appendix J. It must be noted that the (v = 14 m/s, μ = 0°, ϕ = 0°) scatter diagram is equal to the two scatter diagrams where ϕ = 30° and ϕ = 60°, as the floater orientation ϕ refers to the orientation of the floater with respect to the North Pole. Therefore, ϕ does not affect the scatter diagrams.

2.3.2 Wind and wave seeds

For every sea state, a different wave seed was used to generate the JONSWAP spectrum, as generating the wave time series in SIMA is not computationally intensive.
The wind time series were generated using TurbSim [39], a computationally intensive process that results in large files that were used as input to the SIMA model. To decrease computational time and the usage of storage space, only a few wind time series could be computed.
A decision had to be made on the number of seeds to use when computing the loads for a single sea state. Figure 13 shows the results of computing the fatigue damage for multiple wind seeds. In this comparison, the same wave seed was used for every wind seed. This figure shows how the cumulative fatigue damage converges as the number of seeds increases.

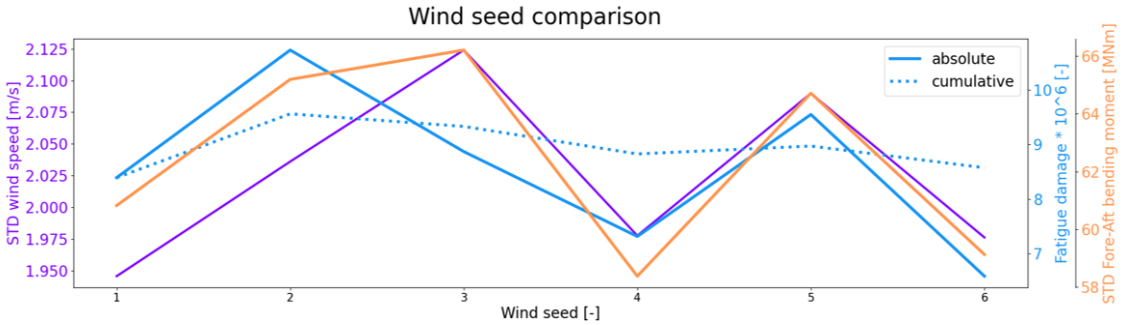

Figure 13: The standard deviation (STD) of the wind speed, the absolute and cumulative fatigue damage and the STD of the fore-aft bending moment for different wind seeds

Based on this graph and the available resources (time, computational power and storage space) it was decided to generate three wind seeds. All sea states were computed using all

three wind files, also using a different wave seed for all sea states every time, and at the end the average fatigue damage was computed. Three examples of the same scatter diagram computed using different wind and wave seeds are shown in Appendix K.
To generate the wind files in TurbSim, the Kaimal model was used. For the IEC turbulence type 'NTM' was chosen, which was defined as 'normal', compared to more extreme turbulence options. A power law wind profile was used when generating these wind files, with a power law exponent of 0.14 and a surface roughness of 0.0003 m.
It must be noted that this is opposed to the logarithmic wind profile that was used to scale up the wind speeds, in order to construct the scatter diagrams, as shown in Section 2.3.1. Figure 14 shows that the two methods result in different wind profiles for different wind speeds. Yet, at a 10 m height (where the hindcast wind speed was measured), the difference in wind speed is a little over one wind speed bin for the 22 m/s case, and even smaller for the 6 m/s and 14 m/s cases. Whether the logarithmic or power law wind profile is assumed, may result in a slight difference in the NOC's for the sea states in the scatter diagrams. This has no effect on the validity of the fatigue damage error comparison (shown in Figure 7) that will be performed in this study. For this reason, the use of different wind profiles will not affect the validity of the study's results.

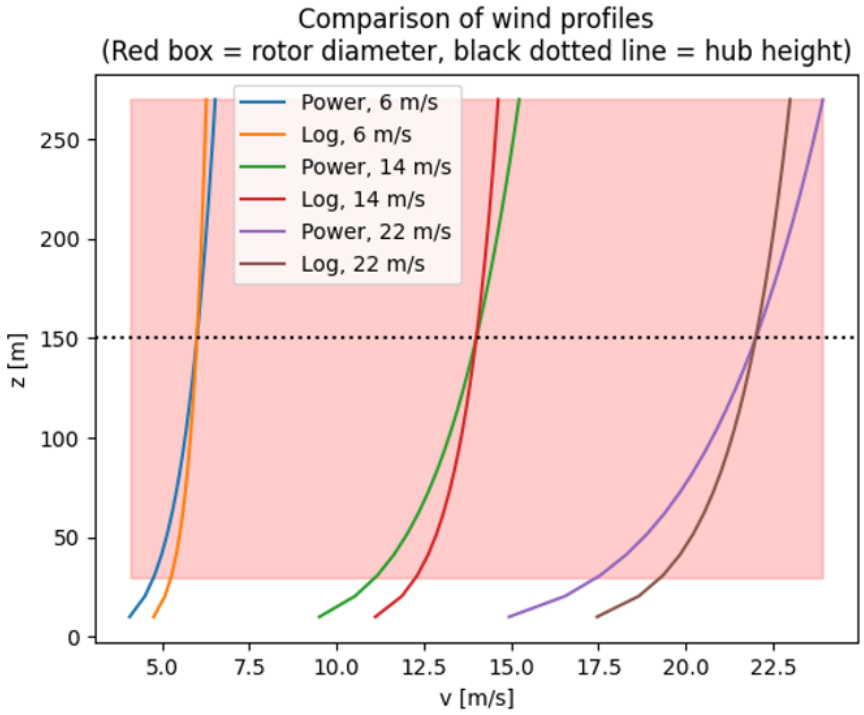

Figure 14: The logarithmic and power law wind profiles assuming a 6 m/s, 14 m/s and 22 m/s wind speed at hub height

2.4 Reference floating wind turbine model

For the turbine, the IEA 15MW reference model is used, that was created by the National Renewable Energy Laboratory of the U.S. Department of Energy, the Technical University of Denmark and the University of Maine [40]. Originally, the foundation of this turbine was a monopile. Later in the year that the turbine documentation was published, the National Renewable Energy Laboratory of the U.S. Department of Energy and the University of Maine published a documentation on a semi-submersible floater for the IEA turbine, called the

VolturnUS-S reference platform [41]. A model for this floating turbine [42] was available in SIMA.
In Table 5, the turbine details are given, as stated in the reference documentation.

Cut-in wind speed:	3 m/s
Cut-out wind speed:	25 m/s
Rated wind speed:	10.59 m/s
Minimum rotor speed:	5 rpm
Maximum rotor speed:	7.56 rpm
Power rating:	15 MW
Hub height:	150 m
Rotor diameter:	240 m
RNA mass	1,017 metric tonnes
Tower mass	1,263 metric tonnes [41]
Tower length	129.495 m [41]

Table 5: Turbine details given by the reference documentation [40]

2.4.1 Wind speed test

A wind speed test was performed to check if the rotor speed, blade pitch, generator torque, thrust and power of the SIMA model changed similarly to the documentation (obtained using OpenFAST simulations), for an increasing wind speed. The results are shown in Figure 15. The several differences in the results of the two models will now be explained.

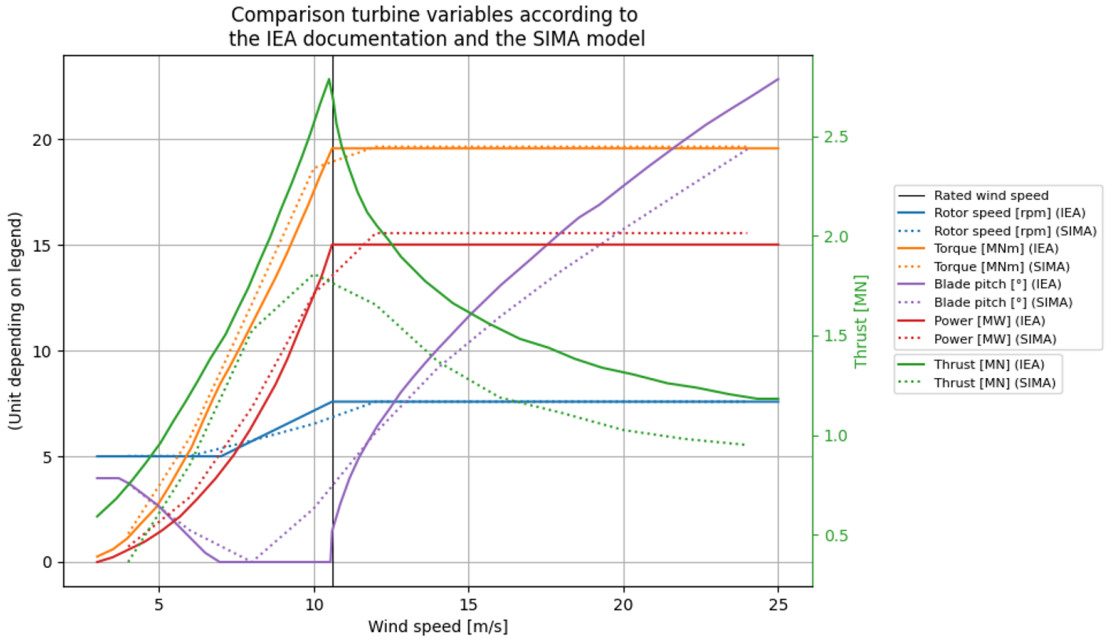

Figure 15: Comparison of rotor speed, torque, blade pitch, power and thrust between the IEA documentation [40] and the SIMA model [33]

The figure shows that the maximum thrust force in SIMA is about 1.8 MN, where in the documentation this is 2.70 MN. It must be noted that the SIMA simulation applied peak

shaving (also called thrust clipping), that may have caused a thrust force reduction of about 200 kN. Peak shaving is a method that reduces the maximum thrust force on the rotor. The blades are pitched slightly before rated wind speed, as visible in the SIMA blade pitch graph. The disadvantage of this practice, is the fact that the maximum power will be reached at a slightly higher wind speed than the rated wind speed. [43]
In addition, in the documentation, the thrust force is actually the force along the shaft. As the shaft is not horizontal but has a 6° tilt, the force along the shafts includes a small RNA weight component. This weight component adds about 700 kN to the thrust. In SIMA, the output thrust involves only the actual thrust.
Subtracting both the 200 kN and 700 kN forces of the documentation thrust force, the maximum thrust force of 1.8 MN given by SIMA seems realistic. [32]
The maximum power reached after rated wind speed equals 15.6 MW in the SIMA model, instead of 15 MW. This is due to the fact that SIMA doesn't account for any power generation losses. The documentation states a 96.5% efficiency. Accounting for the efficiency, the SIMA model gives a maximum power of 15.05 MW. [32]
Lastly, in the SIMA model, a wind speed bin size of 2 m/s was used. For this reason, expected abrupt changes in the graph might appear to happen at slightly different wind speeds. For example, due to the bin size, the rotor speed seems to become constant only after 12 m/s, instead of the rated wind speed of 10.59 m/s. It must be emphasized that in case of the SIMA simulation, peak shaving also affects at which wind speeds these abrupt changes (like the rotor speed becoming constant after rated wind speed) occur.

2.4.2 Decay test

In addition, a decay test was performed to check whether the natural frequencies of the model corresponded to the natural frequencies given in the floater documentation. The method used to perform the decay test is described in Appendix A. The results of the decay test are given in Table 6. The decay test matched the frequencies in the documentation well enough. The fore-aft and side-side frequencies were slightly too low, which might be due to a small difference in boundary condition of the floater design in the SIMA model [32].

	Documentation:	Decay test:
Surge motion:	0.007 Hz	0.007374 Hz
Sway motion:	0.007 Hz	0.007347 Hz
Heave motion:	0.049 Hz	0.04868 Hz
Roll motion:	0.036 Hz	0.03514 Hz
Pitch motion:	0.036 Hz	0.03500 Hz
Yaw motion:	0.011 Hz	0.01104 Hz
Fore-aft bending moment:	0.496 Hz	0.4181 Hz
Side-side bending moment:	0.483 Hz	0.4342 Hz

Table 6: Comparison of natural frequencies of the floater, as stated in the documentation [41] and as found during the decay test in SIMA

3 Fatigue damage analysis model

The load analysis model yields the time series of the internal forces at tower base as an output. Using these results, the time series of the axial and shear stress at the tower base can be computed. The derivation of these formulas will be explained in Section 3.1. Next, the stress ranges occurring in the axial stress time series are determined and counted using rainflow counting and the fatigue damage is computed using the Palmgren-Miner rule and the *S-N* curve, as discussed in Section 3.2.
The last step of the fatigue damage assessment during the design phase of a turbine, is the calculation of the lifetime fatigue damage. As long as the lifetime fatigue damage is smaller than one, no material failure is expected to occur at the investigated location on the turbine. This calculation is discussed in Section 3.3. Nevertheless, in this study usually the *unit fatigue damage* or the *10-year fatigue damage* are required, instead of the lifetime fatigue damage. This will be explained in Section 3.4.

3.1 Stress and shear formula derivation

Figure 16.a shows the local set of axes fixed to the tower base as defined in SIMA. This set of axes will also be used in this derivation. The angle η is defined in Figure 16.b, and represents the angle around the X-axis. Counterclockwise is defined as a positive rotation, and at the positive Z-axis, η equals zero. Figure 16.b also gives the values for sine and cosine at different values of η, as these are relevant to the derivation. Lastly, the orientations of the positive axial stress and shear stress are shown in Figure 16.c and Figure 16.d respectively.

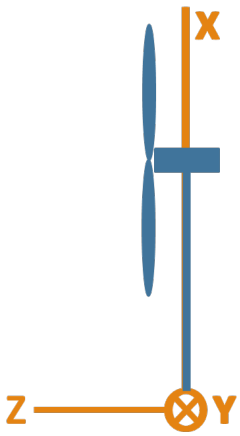

(a) Local set of axes in SIMA

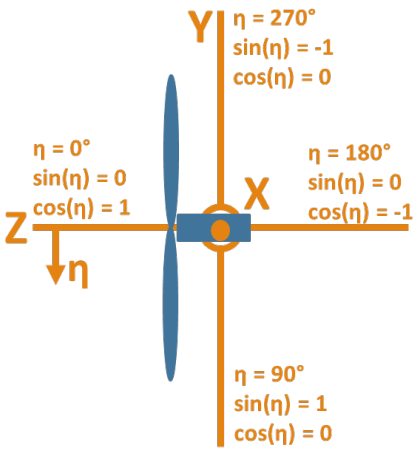

(b) Sign convention of η

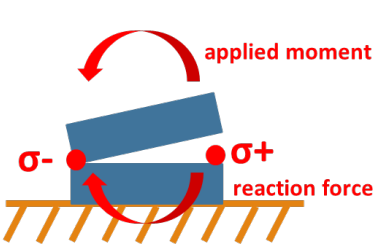

(c) Orientation of positive axial stress

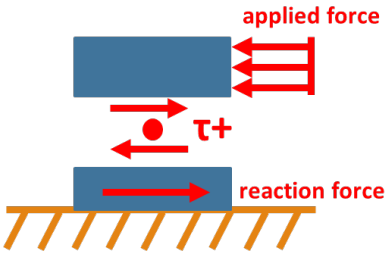

(d) Orientation of positive shear stress

Figure 16: Sign conventions used in the formula derivation of the stress and shear stress

SIMA yields an axial force (N_x), that by definition is positive when the axial stress is positive, as shown in Figure 16.c.
Furthermore, SIMA yields a shear reaction force in Y and Z direction (V_y and V_z) and a reaction bending moment around all three axes (M_x, M_y, M_z). Their positive orientation (as defined by both SIMA and this calculation) are given in Figure 17.

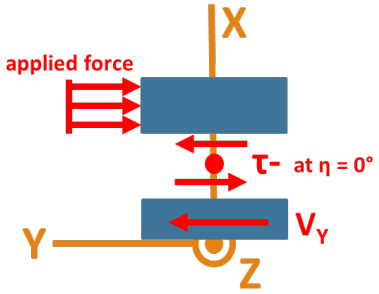

(a) Sign of τ for a positive V_y

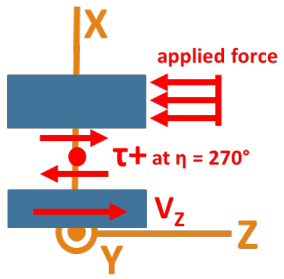

(b) Sign of τ for a positive V_z

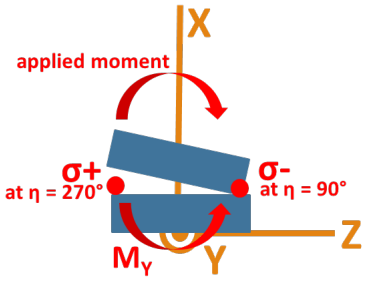

(c) Sign of σ for a positive M_y

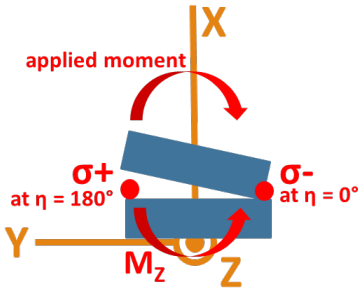

(d) Sign of σ for a positive M_z

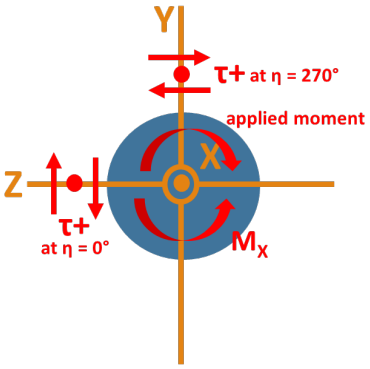

(e) Sign of τ for a positive M_x

Figure 17: Sign of the σ and τ contributions of the internal loads at different values for η

The axial stress equals the sum of the stress caused by the axial force ($\frac{N_x}{A}$), the moment around the Y-axis ($\frac{M_z}{I_z} \cdot r$) and the moment around the Z-axis ($\frac{M_y}{I_y} \cdot r$). These formulas can be derived using structural mechanics theory. The equation for the axial stress is shown in Equation 7.

$$\sigma = \frac{N_x}{A} - \frac{M_z}{I_z} \cdot r \cdot \sin(\eta) - \frac{M_y}{I_y} \cdot r \cdot \cos(\eta) \tag{7}$$

The contribution of N_x is equal for every angle η, as the pressure caused by the axial force

is assumed to be equally distributed along the tower circumference. For this reason, the N_x term in Equation 7 is independent of η.
As Figure 17.c shows, the contribution of M_y is largest at $\eta = 270°$, smallest at $\eta = 90°$ and zero at $\eta = 0°$ and $\eta = 180°$. For this reason, the stress contribution of M_y is multiplied by $\cos(\eta)$.
At $\eta = 90°$, $\cos(\eta) = 1$. Yet, Figure 17.c shows that the stress contribution of M_y has a negative sign at $\eta = 90°$. For this reason, a minus sign is placed in front of the M_y term of Equation 7.
Likewise, the term for the M_z contribution is determined. Equation 8 shows the equation to compute the shear stress, which is derived in a similar way as the σ formula.

$$\tau = \frac{M_x}{J} - \frac{2V_z}{A} \cdot \sin(\eta) - \frac{2V_y}{A} \cdot \cos(\eta) \tag{8}$$

In these formulas, r represents the outer radius at the tower base, equal to 5 m. The wall thickness at tower base t is equal to 0.083 m. [41]
I_y and I_z are the second moment of area with respect to the Y and Z axis respectively. J equals the polar moment of area.
In Appendix B, the plausibility of the resulting stress and shear time series is checked, using the structural parameters given in the documentation. Two final notes on the stress time series must be made on the implementation of these formulas in the fatigue damage calculation:

- The fatigue damage caused by the axial stress is significantly larger than the fatigue damage caused by the shear stress (a factor 10^3 larger in the example in Appendix B). This conclusion was also drawn in previous research [28]. For this reason, this thesis will only use the fatigue damage caused by the axial stress.
- As shown, axial stress time series are computed for every angle η, which represents the angle around the tower base circumference. Angle η_{max} is defined as the angle, where, on average for all sea states in the scatter diagram, the fatigue damage is highest. The fatigue damage of a scatter diagram is based on the fatigue damages of each sea state at this angle η_{max}.

3.2 Rainflow counting and the Palmgren-Miner rule

The fatigue damage is computed by the Palmgren-Miner rule in Equation 1. This formula shows that in order to compute the fatigue damage, the stress ranges that are present in the stress time series must be identified (S_i with $i \in 1, ..., k$, where k is equal to the number of identified stress ranges), and their number of occurrences n_i must be counted. This is done using the rainflow counting method. The rainflow counting is performed by the WAFO toolbox in MATLAB [44] and the Rainflow package in Python [45]. The value for N_i in Equation 1 (the maximum number of occurrences of stress range S_i before material failure occurs) is determined using the S-N curve. This curve will be explained in Section 3.2.1. The fatigue damage D_j resulting from sea state j computed by the Palmgren-Miner rule is called the *unit fatigue damage*, as it has not been multiplied by the number of occurrences of the sea state j.

3.2.1 Bilinear *S-N* curve

The *S-N* curve D [36] of the DNV-RP-C203 [46] was used, as shown in Figure 18. The *S-N* curve assumes steel as the material. An exposure to air (in contrast to seawater) is assumed at the tower base, being located at the interface between the floater and the tower just above seawater level. For this *S-N* curve, a MATLAB script is available [47], that was rewritten in Python.

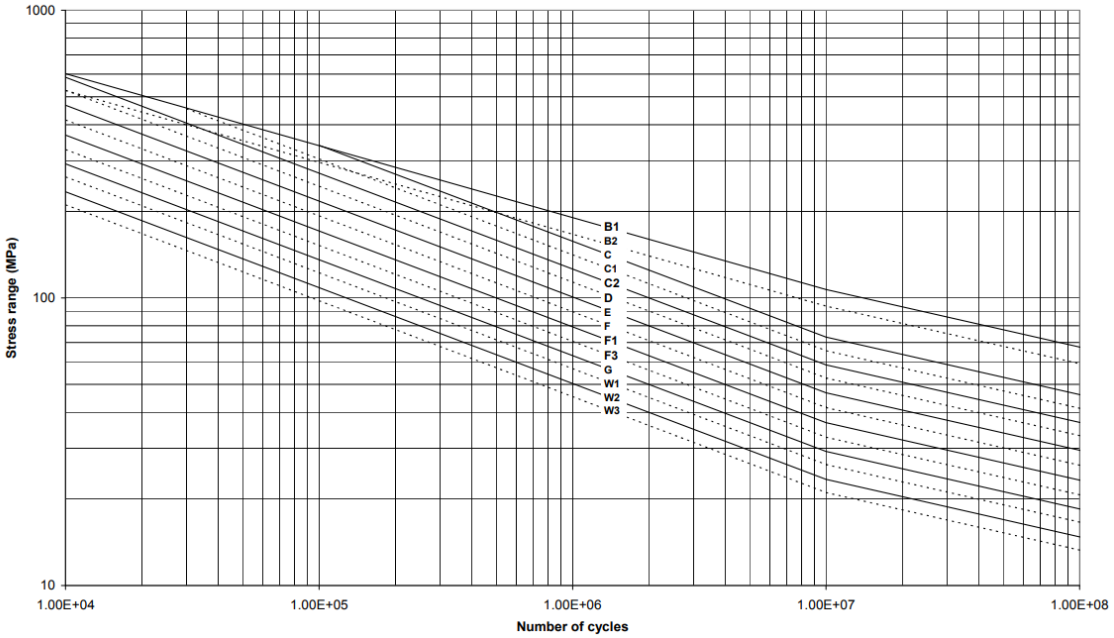

Figure 18: Bilinear *S-N* curve for steel assuming an exposure to air [46]

The *S-N* curve can be described by Equation 9.

$$\log(N) = \log(\bar{a}) - m \log\left(S\left(\frac{t}{t_{ref}}\right)^{k}\right) \tag{9}$$

Here, m represents the slope of the curve, given by Equation 10 and $\log(\bar{a})$ represents the intercept of the $\log(N)$ axis, given by Equation 11. As these formulas show, the values of m and $\log(\bar{a})$ change at $N = 10^7$. The fatigue limit S at this N is equal to 52.63 MPa. t equals the thickness of the cross-section and is set to 0.083 m [41]. t_{ref} is the reference thickness, set to 0.025 m (for welded connections [46]), and k is set to 0.2 (for this S-N curve D [46]).

$$m = \begin{cases} 3, & \text{for } N \leq 10^7 \text{ and } S \geq 52.63 \text{ MPa} \\ 5, & \text{for } N > 10^7 \text{ and } S < 52.63 \text{ MPa} \end{cases} \tag{10}$$

$$\log(\bar{a}) = \begin{cases} 12.164, & \text{for } N \leq 10^7 \text{ and } S \geq 52.63 \text{ MPa} \\ 15.606, & \text{for } N > 10^7 \text{ and } S < 52.63 \text{ MPa} \end{cases} \tag{11}$$

3.3 Calculating the lifetime fatigue damage

The fatigue damage of a scatter diagram over the turbine's lifetime is computed by Equation 12. Here, n_j equals the number of occurrences (NOC) of sea state j, t_{lifetime}

equals the turbine's lifetime (for example, 25 years) and t_{hindcast} is equal to the period covered by the hindcast (10 years in this hindcast's case).

$$D_{\text{scatter diagram, lifetime}} = \sum_{j=1}^{N_{ss}} n_j \frac{t_{\text{lifetime}}}{t_{\text{hindcast}}} \cdot D_j \tag{12}$$

If a lumping method is used, this formula becomes Equation 13, where N_{lss} equals the number of lumped sea states of the scatter diagram.

$$D_{\text{scatter diagram, lifetime, lumped}} = \sum_{k=1}^{N_{lss}} n_k \frac{t_{\text{lifetime}}}{t_{\text{hindcast}}} \cdot D_k \tag{13}$$

Now, the fatigue damage of the entire hindcast is computed using Equation 14. If $0 \leq D_{\text{lifetime}} < 1$, no material failure due to fatigue damage is expected to occur, during the turbine's lifetime, at the location on the turbine, where the fatigue damage assessment was performed. If $D_{\text{lifetime}} \geq 1$, material failure due to fatigue damage is expected.

$$D_{\text{lifetime}} = \sum_{p=1}^{N_{\text{scatter diagrams, lifetime}}} D_{\text{scatter diagram, lifetime, p}} \tag{14}$$

3.4 In this study

Whenever this thesis refers to *the fatigue damage of a sea state*, the *unit fatigue damage* (computed by the Palmgren-Miner rule, see Section 3.2) caused by the axial stress at tower base circumference angle η_{max} (see Section 3.1) is meant, unless stated otherwise. In Figure 19, this fatigue damage is shown for every sea state in a scatter diagram. In this figure, the T_p-axis is inverted. In this way, the wave energy of the sea states increases, as they are located further away from the origin (as an increase in H_s and a decrease in T_p cause the wave energy to increase). As an increase in wave energy somewhat correlates with an increase in fatigue damage (but not always, as will be explained below), inverting the T_p-axis is a more intuitive way of presenting scatter diagram figures for the purpose of this study.

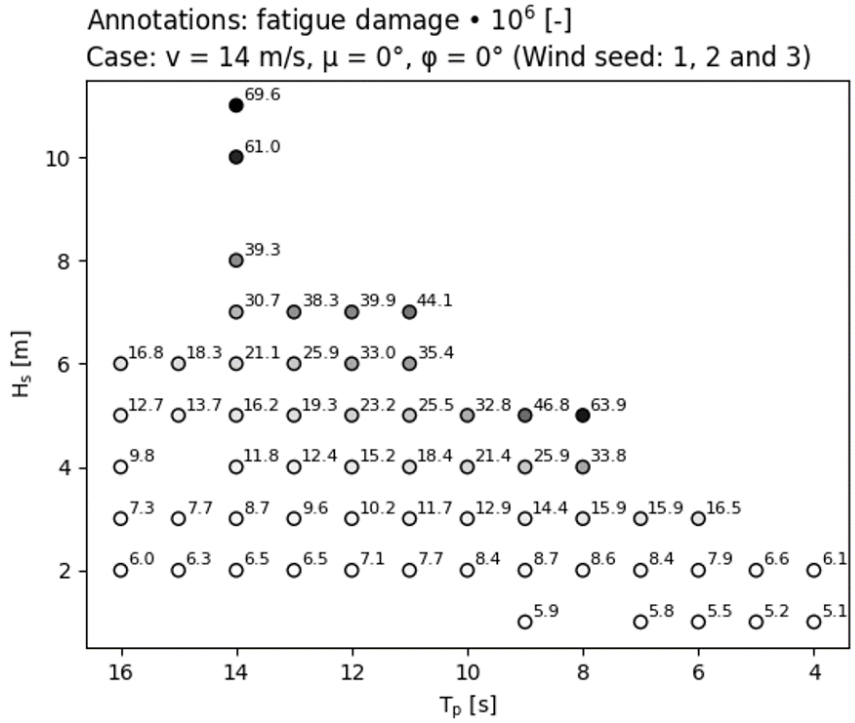

Figure 19: Unit fatigue for every sea state in a scatter diagram

This figure shows the following relations between the sea state and the fatigue damage:

- For all sea states, D increases, as H_s increases. This is due to the fact that H_s is proportional to the amplitude of the hydrodynamic loads F_{hydro} ($F_{\text{hydro}} \propto a \propto H_s$, where a is the amplitude of the water particle acceleration), causing the structure to experience higher stress amplitudes. The Palmgren-Miner rule in Equation 1 shows that increased stress amplitudes result in an increased fatigue damage.
- There are three components that influence the relation between T_p and the unit fatigue damage D:

  1. As T_p decreases, the number of load cycles experienced by the floater increases. According to the Palmgren-Miner rule in Equation 1, this increases the fatigue damage.
  2. As T_p decreases, the water particle acceleration increases, which causes the hydrodynamic loads to increase. Because of this, the tower base experiences higher stress ranges, resulting in a higher fatigue damage (see Palmgren-Miner rule).
  3. As T_p decreases, diffraction effects increase. Diffraction dissipates energy (as waves start to spread perpendicular to the wave direction) and thereby reduces the hydrodynamic loads experienced by the floater. This decreases the fatigue damage (see Palmgren-Miner rule). For low values of T_p, this effects starts to dominate the two previous effects.

  Components 1 and 2 describe the relation $T_p \propto -D$. This relation is visible in Figure 19 for high values of T_p ($T_p > 9$ s when $H_s < 3$ m, for any T_p when $H_s \geq 3$ m). Component 3 describes the relation $T_p \propto D$. This relation is visible in the results for low values of

T_p ($T_p < 9$ s when $H_s < 3$ m). At which T_p diffraction effects (causing the $T_p \propto D$ relation) start to dominate over the other two effects, depends on the structural design.

The relations between the sea state and the fatigue damage described above will be derived and explained in more detail in Section 4.2.2.

When Equation 12 and Equation 13 are substituted into Equation 5, the $\frac{t_{\text{lifetime}}}{t_{\text{hindcast}}}$ term is cancelled out. For this reason, the $\frac{t_{\text{lifetime}}}{t_{\text{hindcast}}}$ term is not taken into account in this study, and thereby the fatigue damage over a 10-year period (length of the hindcast) is computed, instead of the lifetime fatigue damage. Unless stated otherwise, whenever *the fatigue damage of a scatter diagram* is mentioned in this thesis, the 10-year fatigue damage is meant, computed by Equation 3. Equation 4 computes the 10-year fatigue damage of a scatter diagram when a lumping method is used. Figure 20 shows the 10-year fatigue damage for every sea state (equal to $D_j \cdot n_j$ for sea state j, where D_j is the unit fatigue damage of sea state j and n_j is the NOC of sea state j).

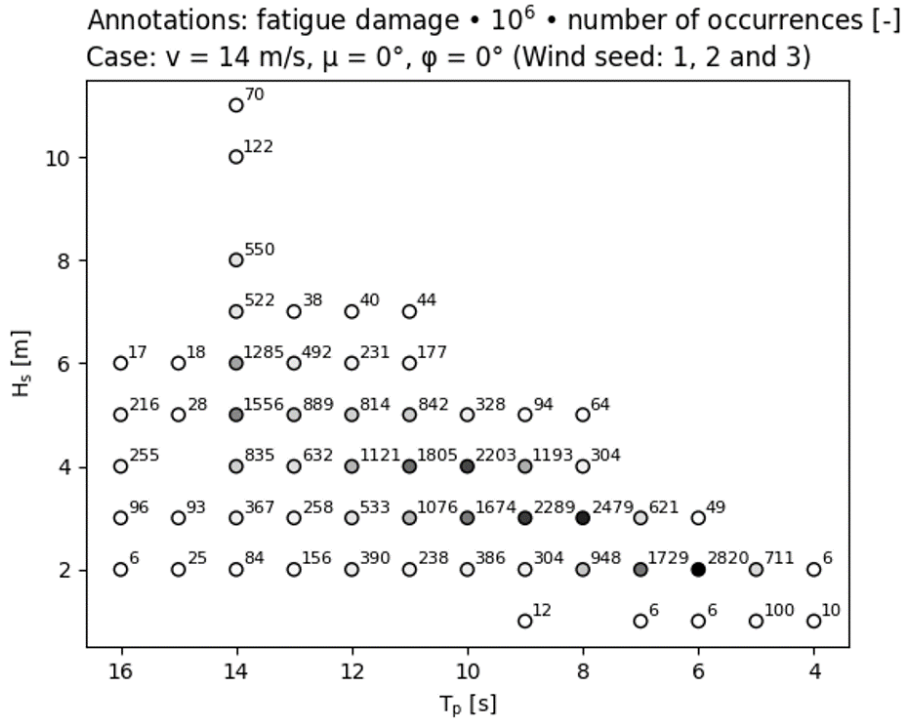

Figure 20: 10-year fatigue damage for every sea state in a scatter diagram

Part II

Explaining Lumping Method Accuracy

In this part, the first subquestion of this thesis will be studied:

1. What factors determine the accuracy of a lumping method?

This is done in preparation of explaining the results on lumping method accuracy in Section 6. Section 4 will discuss subquestion 1a:

1a. Which hydrodynamic factors influence the fatigue damage gradient at tower base most for a semi-submersible?

As this thesis aims to lump T_p and H_s, only effects that are related to either or both T_p and H_s are relevant. In practice, this involves hydrodynamic effects and potentially coupling effects between wind and waves. The fatigue damage gradient is defined as the change in fatigue damage over T_p and H_s across a scatter diagram (see the colour change in Figure 19). The reason why this gradient is studied, in contrast to the absolute fatigue damage, will be elaborated in Section 5.2.
When the hydrodynamics that affect the fatigue damage gradient are identified, they can be compared to the hydrodynamic model that is assumed by the lumping methods. This will be done in Section 5, thereby discussing subquestion 1b:

1b. Which hydrodynamic model is assumed by the lumping methods?

If a hydrodynamic factor that is of great influence to the fatigue damage gradient, is not accounted for by a lumping method, the lumping is predicted to have a lower accuracy. Lastly, Section 5.3 will provide a summary of the findings regarding both subquestion 1a and 1b.
As stated in Section 1, the overall performance of a lumping method is determined by both its accuracy and its reduction of computational time. This part will only focus on accuracy. Studying the reduction of computational time will be a part of Section 6, where the performance of the four methods will be measured.

4 Hydrodynamics influencing the fatigue damage gradient

The effects causing fatigue damage at tower base can be split up into three types:

- Hydrodynamic effects;
- Aerodynamic effects;
- Coupling effects between wind and waves.

Wind speed and wind direction (affecting aerodynamic effects) are constant for a scatter diagram, while T_p and H_s are not. By definition, effects constant for the entire scatter

diagram cannot influence the fatigue damage gradient. For this reason, only the coupling effects (see Section 4.1) and the hydrodynamic effects (see Section 4.2) are relevant to study.

4.1 Coupling effects

The motions of the floater are caused by both the aerodynamic and hydrodynamic loads. In addition, the aerodynamic loads depend on the position of the floater. This is called a coupled system. When a decoupled system is assumed, then the effect of the position of the floater on the aerodynamic loads is either estimated or neglected.
In Section 4.1.1, the findings of a previous study on coupling effects for a semi-submersible are discussed, and the influence of coupling effects on the fatigue damage will be explained. Section 4.1.2 will study how a change in T_p and H_s influences the contribution of coupling effects to the axial stress, for the semi-submersible studied in this thesis.

4.1.1 Previous research on coupling effects acting on a semi-submersible

A previous study [48] investigated the contribution of coupling effects to the fatigue damage for the DeepCWind floating turbine. This turbine has a semi-submersible floater, where the turbine is placed on the centre column, just like the floater studied in this thesis. For different values of H_s, T_p, v, the wind direction and the wave direction, the coupling effects accounted for 12.18% to 25.07% of the fatigue damage. The study compared the fatigue damage computed by a decoupled system (by adding the stress spectra of the wave-only and wind-only case) to the fatigue damage computed to a coupled system. The error that occurred ranged between 2.9% and 8.8%. The decoupled system overestimates the stress ranges at the pitch resonance, while the stress ranges at wave and the tower natural frequencies are estimated accurately.
The overestimation of the pitch resonance is likely due to the fact that aerodynamic damping decreases pitch resonance in a coupled system. As the floater is pitching forwards, due to wave excitation, the rotor is moving in the opposite direction to the wind. The rotor now experiences a higher relative wind speed (wind speed + speed of own motion) than when the floater is not moving. Equation 15 shows the equation for the thrust force, where ρ equals the air density, C_D equals the drag coefficient of the rotor, A equals the surface area of the rotor and u equals the relative wind speed experiences by the rotor.

$$F_{\text{thrust}} = \frac{1}{2}\rho C_D A u^2 \tag{15}$$

This equation shows that the thrust force increases as the relative wind speed experienced by the rotor increases. For this reason, the rotor experiences a higher thrust force when moving forwards (opposite wind direction) and lower thrust force when moving backwards (in wind direction). This effect dampens the pitch motion of the turbine, and is commonly referred to as aerodynamic damping.
Nevertheless, in a decoupled system, the pitch motion is not known when the thrust force is computed, and could either be estimated or neglected. Assuming the latter, the pitch motion is not damped in a decoupled system as it should, causing a higher peak at the pitch motion natural frequency in the axial stress PSD.
For cases with a higher wind to wave induced response ratio, this decrease in pitch resonance is less dominant and therefore the fatigue damage error of the decoupled system is lower.
This previous study [48] showed that superpositioning the stress PSD of a wind-only and

the stress PSD of a wave-only load simulation, leads to an acceptable approximation of the fatigue damage, for the semi-submersible studied in that paper. This shows that wind and waves can potentially be decoupled for fatigue damage analysis.

4.1.2 Relation between the sea state and the contribution of coupling effect to the axial stress

In this thesis, a study on coupling of wind and waves was performed, focussing on the effect that T_p and H_s have on the possibility to decouple the system. This effect is studied, as most lumping methods do not take wind or coupling effects into account. If the possibility to decouple the system varies over T_p and H_s, a decoupled model will result in an incorrect fatigue damage gradient.
Figure 21 shows two subfigures, where the axial stress PSD's are computed for different combinations of T_p and H_s, for a wind speed of 14 m/s, and a wind-wave misalignment and floater orientation of both 0°. To compute the axial stress, time domain load simulations were used, as described in Part I. For every combination of T_p and H_s, the same wind seed and wave seed was used.
The orange graphs in Figure 21.a, represent the axial stress PSD's at tower base, computed using a time domain load simulation that included both wind and wave effects. For the blue graphs in this figure, the tower shadowing and wind turbulence (the main wind effects that cause cyclic stresses) were turned off and the wave effects remained. Figure 21.b shows an enlarged version of the blue graphs in Figure 21.a. Compared to the wind-wave graphs, the high stresses at low frequencies in the wind turbulence range have disappeared in the wave-only graphs, as well as the stresses at the 3P frequency.
In order to isolate the stresses caused by the wind turbulence, the axial stress PSD's where wind turbulence is turned off (and tower shadowing is turned on) is subtracted from the axial stress PSD's where both wind turbulence and tower shadowing are turned on. This figure is shown in Figure 22.a.

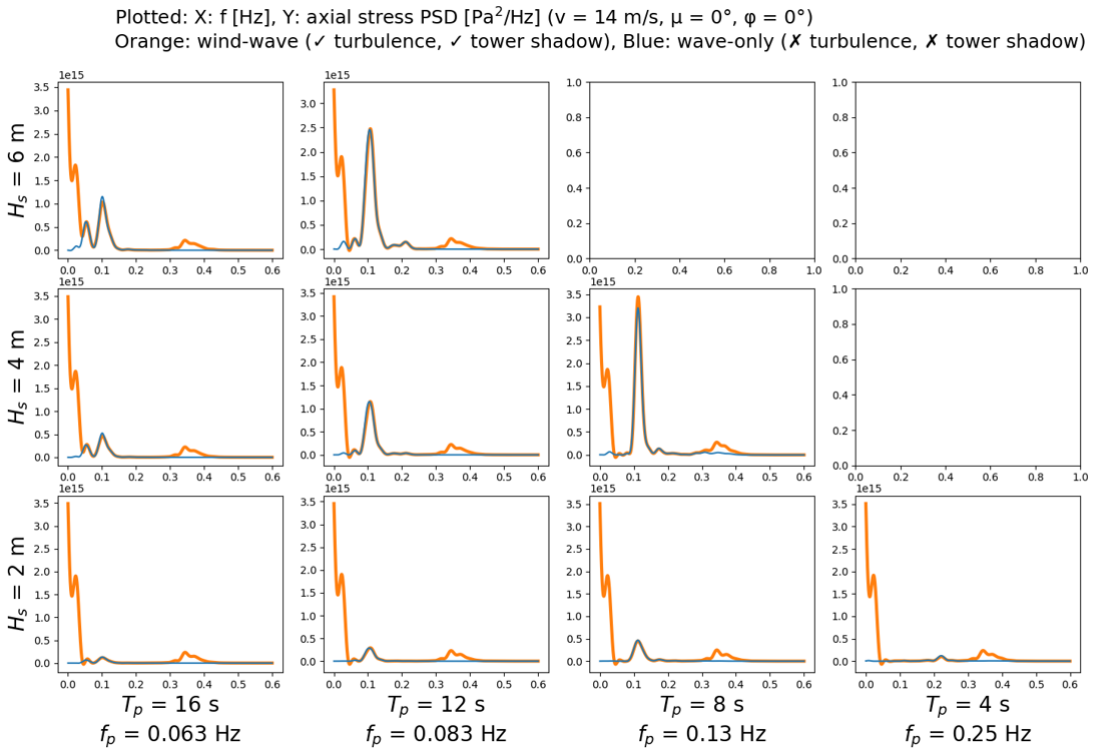

(a) Wind-wave (orange) and wave-only (blue)

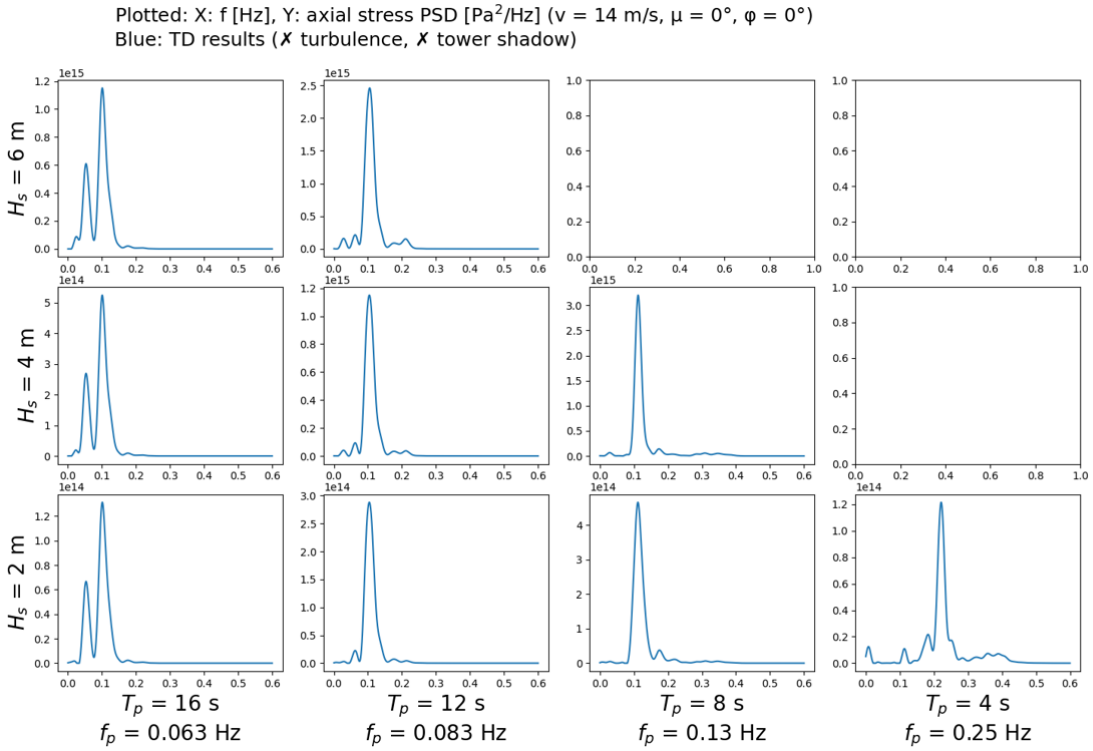

(b) Wave-only (zoomed in)

Figure 21: Axial stress PSD's for time domain simulation with wind effects turned off or turned on

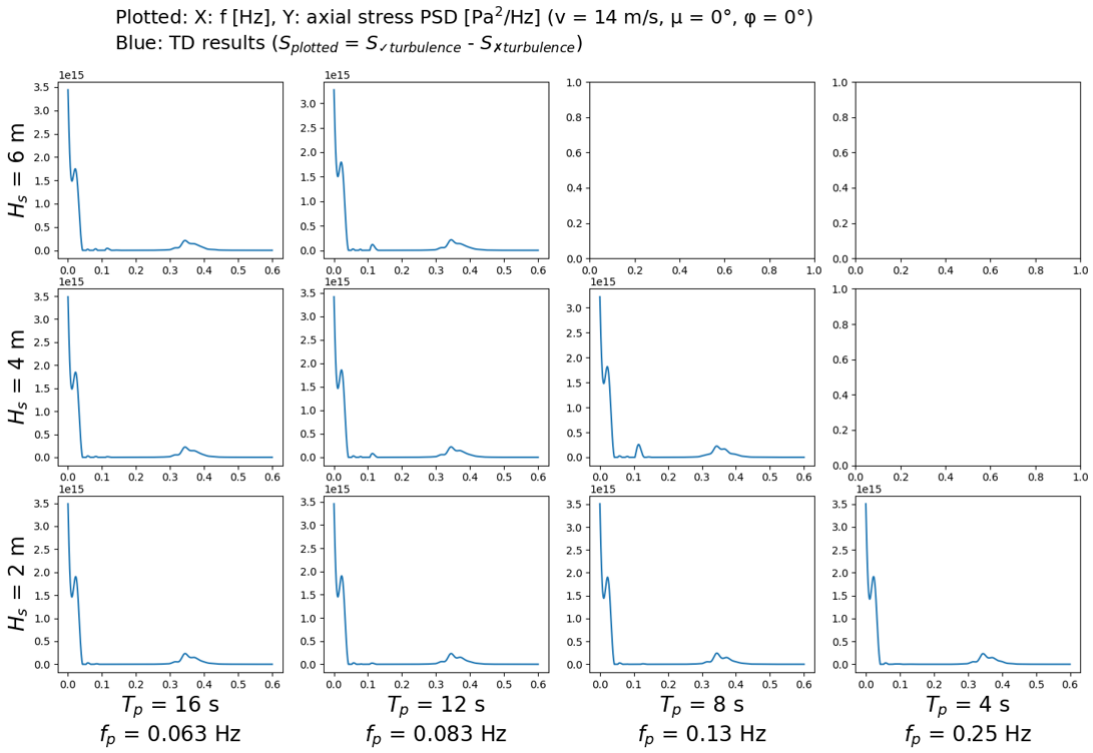

(a) Turbulence effects

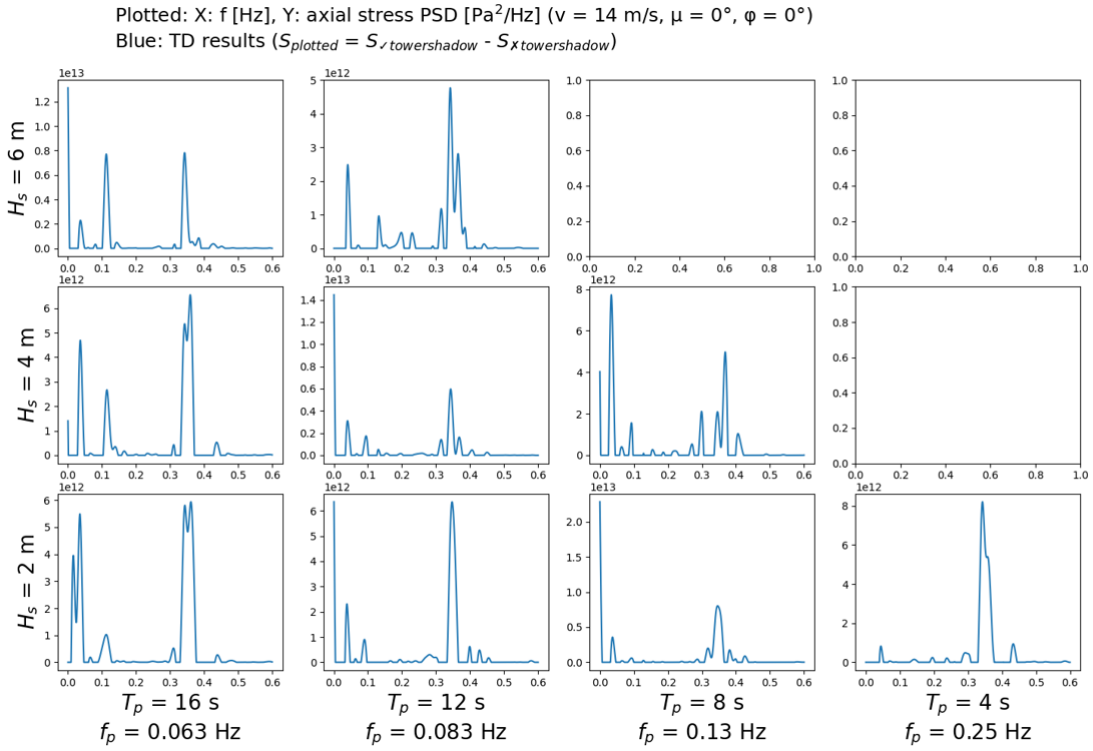

(b) Tower shadowing effects

Figure 22: Axial stress PSD's caused by just turbulence or tower shadowing effects

For a system without any coupling between wind and waves, the graphs in Figure 22 should be exactly the same for every T_p and H_s, as the wind speed and wind direction is constant for the entire scatter diagram and only wind effects are plotted here. For the turbulence

effects, small differences can be observed, especially for the height of the peak at the lowest frequencies. Yet, these differences (with an order of magnitude of 12) are relatively small compared to the wave-only stress PSD's (with an order of magnitude of 14 and 15) shown in Figure 21.b, and are therefore assumed to be negligible. In addition, Figure 22.a shows stress ranges at the 3P frequency. These stress ranges are caused by the fact that the turbulence differs across the rotor area. If there would be a location on the rotor plane that experiences a high concentration of turbulence, a blade would pass through this area in 3P frequency, causing these extra stress ranges. As the figure shows, this effect is not influenced by a change in T_p or H_s.
It must be noted that the stress ranges at 3P in Figure 22.a cannot be caused by tower shadowing, as Figure 22.a shows turbulence effects only (tower shadowing effects are subtracted from the PSD).
Figure 22.b shows that the effects caused by tower shadowing have a less consistent pattern than the effects by wind turbulence. Yet, as the tower shadowing stress PSD's are low (with an order of magnitude of 12 and 13), relative to the wave-only stress PSD's, these effects are assumed to be negligible as well. Due to the small effects of tower shadowing, the stress PSD's where turbulence was turned on and tower shadowing was turned off looked similar to the wind-wave case in Figure 21.a. When tower shadowing was turned on and wind turbulence was turned off, the stress PSD's were similar to Figure 21.b.
In conclusion, this study shows that for the (v = 14 m/s, μ = 0°, ϕ = 0°) scatter diagram, the wind and waves may be decoupled for lumping purposes.
Nevertheless, this result may differ for other scatter diagrams. Below, the effect that v, μ and ϕ might have on the possibility to decouple the system, are described based on theory:

- **Wind speed v:** Up to rated wind speed, the 3P frequency increase as the wind speed increases. For wind speeds higher than the rated wind speed, it is assumed that the turbine controller is capable of maintaining a constant mean rotor speed, as was confirmed by Figure 15. At rated wind speed, the 3P frequency of 0.38 Hz approaches the first natural tower frequency of 0.42 Hz. Yet, according to the study in Section 4.1.1, coupling effects mainly occur due to resonance with the pitch motion natural frequency. In addition, no coupling effects that are influenced by T_p and H_s were observed for the 14 m/s second case in the study described in this section. For these reasons, amplification of coupling effects due to a different wind speed is unlikely.

- **Wind-wave misalignment μ:** Section 4.1.1 concluded that in a coupled system, the pitch resonance is lower compared to a decoupled system, most likely due to aerodynamic damping. For this reason, the coupling effects might increase when wind and waves are aligned, when aerodynamic damping (in pitch direction) is aligned with the main excitation of the waves (in pitch direction as well). For a 90° wind-wave misalignment, when the waves mainly excite the roll motion, the aerodynamic damping is less influential on the floater motions, and coupling effects might be lower.

- **Floater orientation ϕ:** When the floater is orientated in such a way that the floater dimensions interact with specific wave lengths, the contribution of the waves to the fatigue damage is increased [28]. When wind and waves are aligned, the higher motions are causing a higher aerodynamic damping, resulting in more coupling between wind and waves [48].

Despite the described relations between μ, ϕ and coupling effects, the previous study [48] found only small errors between the fatigue damage, computed by a coupled model and

computed by a decoupled model, for various values of v, μ and ϕ. The results from Figure 22 confirm this result for v = 14 m/s, μ = 0° and ϕ = 0°. For this reason, it is assumed that for lumping purposes, the decoupling of wind and waves is an acceptable simplification for a semi-submersible.

4.2 Hydrodynamic effects

Hydrodynamic effects are assumed to have the largest influence on the fatigue damage gradient, as they are directly related to T_p and H_s. Equation 16 shows the equation of motion of the turbine and floater, where only hydrodynamic external forces are considered (turbulence, tower shadowing and the thrust force are neglected). This equation will be the starting point for studying the numerous ways in which the hydrodynamics of the system affects the fatigue damage gradient.

$$\{-\omega^2(M + a(\omega)) - i\omega b(\omega) + C\}X = H\zeta_a \tag{16}$$

In this formula, M equals the mass matrix, $a(\omega)$ equals the frequency dependent added mass matrix, $b(\omega)$ equals the frequency dependent damping matrix and C equals the stiffness matrix. i is the imaginary unit, X describes the position of the floater, ζ_a describes the wave amplitude of every frequency in the spectrum and H is the transfer function between the wave spectrum and the spectrum of hydrodynamic forces acting on the floater. The floater and the turbine are assumed to be a single rigid body.
The equation of motion is derived, based on the superposition of an oscillating body is still water (*radiation problem*, left side of the equation) and the restrained body in waves (*diffraction problem*, right side of the equation).
Equation 16 gives the relation between the floater motions (related to X), the rigid body eigenfrequencies (derivable from the matrices mentioned above) and the excitation forces (right side of the equation). As the internal stress at the tower base (and therefore the fatigue damage) is caused by the motions of the floater, the fatigue damage at the tower base is influenced by these four matrices and the $H\zeta_a$ term. In order to answer research subquestion 1a, this section will investigate whether (and if so, how) T_p and H_s affect these terms. If this is the case, these terms are expected to influence the fatigue damage gradient and should therefore be taken into account by lumping methods.
In addition, this section will study whether these terms are influenced by v, μ and ϕ. If so, the relation between these terms and parameters should be taken into account when applying a lumping method to different scatter diagrams.
Section 4.2.1 will study the diffraction problem using the wave excitation transfer function of the floater. Section 4.2.2 and Section 4.2.3 will describe several phenomena in more detail, that affect the wave excitation transfer functions and thereby influence the hydrodynamic excitation of the system. Section 4.2.4 will evaluate the floater's radiation problem.
Lastly, Section 4.2.5 will use the motion RAO's to validate and summarise the findings from previous sections, and will explain the effect that the findings are expected to have on the fatigue damage gradient.

4.2.1 Diffraction problem

In SIMA, the PSD that is used to generate the hydrodynamic excitation forces, is equal to the wave amplitude vector ζ_a, multiplied by the wave excitation transfer function H. This term constitutes the right side of the equation of motion in Equation 16 and relates to the

diffraction problem.
Vector ζ_a is dependent on the wave spectrum (and thereby related to T_p and H_s) and the phase of each wave frequency. Transfer function H is an input value of the time domain computation software SIMA. This transfer function has been generated using the potential flow solver WAMIT and can be obtained from the floater's documentation [41]. For each rigid body degree of freedom (surge, sway, heave, roll, pitch and yaw) and for each wave angle (from 0° to 180° with a step size of 15°), a transfer function is generated. Due to the non-axisymmetric shape of the floater, transfer functions corresponding to different wave angles show large differences.
As an example, this section will study the 0° wave angle and 90° wave angle. Table 7 shows the order of magnitude of the transfer functions corresponding to these wave angles.

Wave direction:	Surge:	Sway:	Heave:	Roll:	Pitch:	Yaw:
0°	6	-3	6	1	8	1
90°	6	6	6	8	7	8

Table 7: Order of magnitudes of the wave excitation transfer functions, corresponding to a 0° and 90° wave direction

This table shows that for a 0° wave direction, the pitch moment transfer function has the highest order. For a 90° wave direction, the roll, pitch and yaw moment transfer function have the highest order. As an example, this section will study these four transfer functions. They are shown in Figure 23. It must be noted that especially the yaw transfer function is unlikely to affect the tower base axial stress (and thereby the fatigue damage gradient).

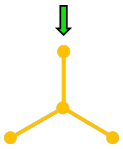

(a) 0° orientation

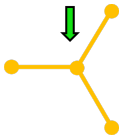

(b) 90° orientation

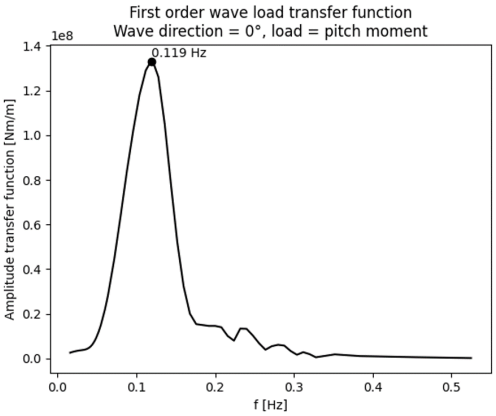

(c) Pitch moment transfer function at 0°

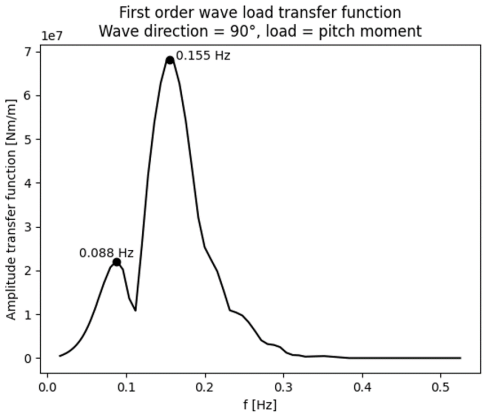

(d) Pitch moment transfer function at 90°

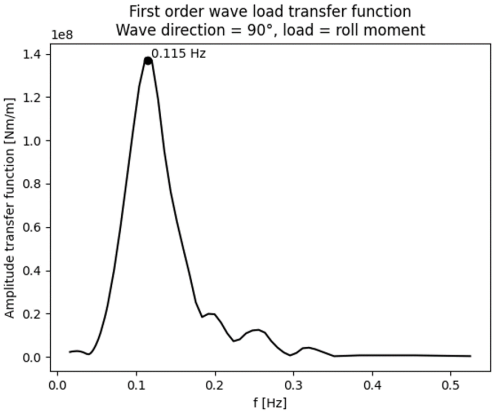

(e) Roll moment transfer function at 90°

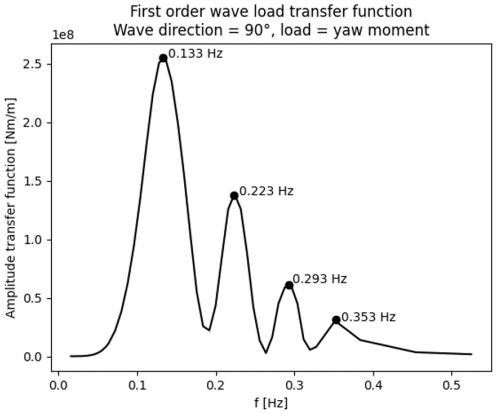

(f) Yaw moment transfer function at 90°

Figure 23: Wave transfer functions for pitch moment at a 0° and 90° wave direction. To show the orientation of the floater at these wave directions, the top view of the floater is given, where the green arrow represents the wave direction.

The fact that ζ_a from the $\zeta_a H$ term, is dependent on T_p and H_s has already been discussed. Now, the question rests whether there exists a relation between T_p, H_s, v, μ or ϕ, and the peaks in transfer function H.
This involves a complex 3D problem, usually solve by potential flow software. For this reason, a simplification called the *strip theory approach* is used to answer this question. Strip theory divides the part of the structure that is located in the water, into a finite number of horizontal cylinders rigidly connected to each other, positioned transverse to the flow, as shown in Figure 24 [49].

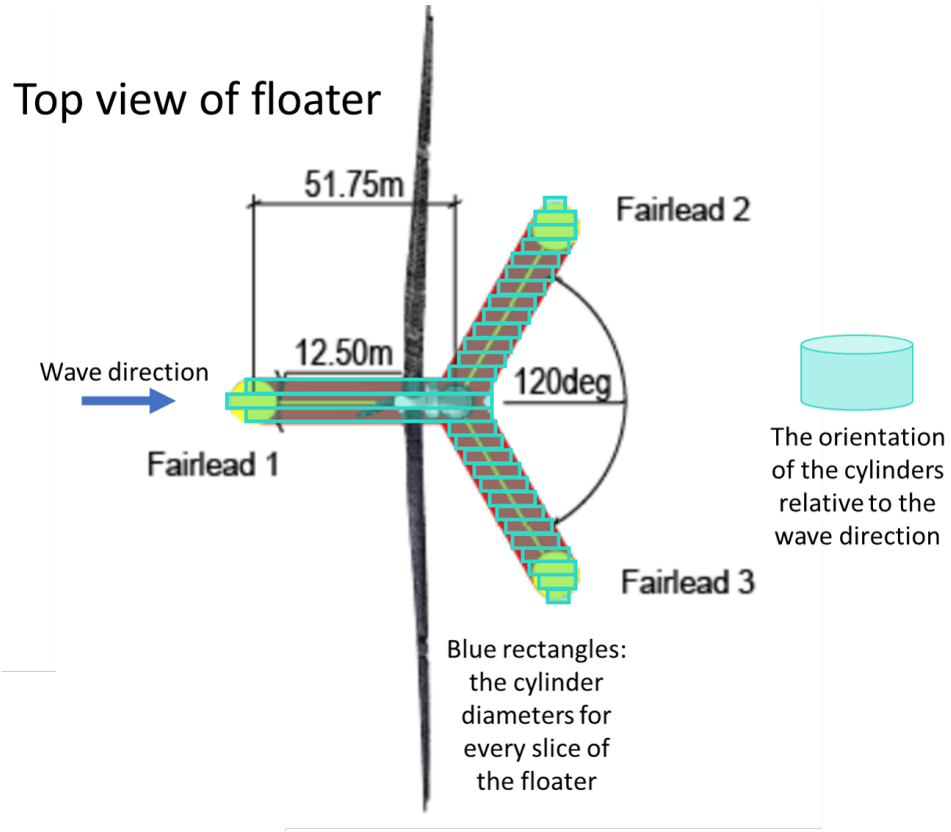

Figure 24: The slices of the floater, each representing a cylinder with a unique diameter according to the strip theory approach (background figure is retrieved from floater documentation [41])

Using this simplification, the causes for the peaks in the wave excitation transfer function will be evaluated in two ways:

- As the floater is now modelled as a series of cylinders, positioned transverse to the water flow, the inertia term of Morison's equation is used to derive several relations between wave period T and wave height H, and the hydrodynamic excitation, in Section 4.2.2.
- The wave length is compared to the diameter of strip theory cylinders (as well as other floater dimensions) to derive a relation between wave length (related to wave period T), the floater orientation ϕ and hydrodynamic excitation, in Section 4.2.3.

4.2.2 Wave frequency and Morison's equation

Equation 17 shows Morison's equation. Here, ρ is the seawater density, C_A equals the added mass coefficient, A equals the cross-sectional area of the body, a equals the water particle acceleration, C_D equals the drag coefficient, v equals the water particle velocity and d equals the structure's diameter. For inertia dominated structures, the first term is much larger than the second term. [18]

$$F_{\text{Morison}} = \rho(1 + C_A)Aa + \frac{1}{2}\rho C_D v|v|d \tag{17}$$

This section will first prove that the system is inertia dominated. Then, the relations between the sea state's wave period and wave height, and the hydrodynamic force F_{Morison}

will be deduced, assuming the second term of the Morison's equation can be neglected.

Inertia dominated structure
Whether a structure is inertia or drag dominated, is dependent on the Keulegan-Carpenter number, given in Equation 18. Here, v_{max} equals the maximum water particle velocity, T is the wave period and d is the structure's diameter. [50]

$$KC = \frac{v_{max} T}{d} \tag{18}$$

For $KC < 3$, the system is inertia dominated and the drag force can be neglected. For $3 < KC < 15$, the drag force should be linearized. For $15 < KC < 45$, both inertia and drag forces are relevant (the Morison's equation is less accurate for this range). For $KC > 45$, the system is drag dominated and the inertia force can be neglected. [49]
First, diameter d will be determined. The Morison's equation assumes that the structure has a cylinder shape. The cylinder slices shown in Figure 24 have a diameter ranging from 7 m (pontoon only) to 63 m (ranging from the front column to the centre column).
In addition, the *equivalent stick representation method* can be used to simplify the structure to a single, vertical cylinder with equivalent diameter d. [51]
When applying this method, first the equivalent diameters of all members individually are computed. Then these are summed, yielding the total equivalent diameter. For the columns, the equivalent diameter is equal to the diameter of the columns. For the horizontal pontoons, the equivalent diameter is equal to the length of the pontoons for drag dominated structures and equal to $\sqrt{dL}$ for inertia dominated structures (where d equals the pontoon diameter and L equals the pontoon length). [51]
Table 8 shows the results.

Wave direction:	Drag dominated:	Inertia dominated:
0°	59.994 m	52.694 m
90°	47.985 m	47.702 m

Table 8: Equivalent stick diameters computed for a drag and inertia dominated case at a 0° and 90° wave direction (see Figure 23.b and Figure 23.c)

Now that several estimations have been found for d, the maximum water particle velocity v_{max} will be estimated next, using the equation for water particle velocity, given in Equation 19. Here, H equals the wave height, ω equals the wave frequency, k equals the wave number, y equals the distance from the sea bed, D equals the water depth (equal to 200 m), x equals the horizontal distance away from the origin (equal to 0 m), and t equals the time.

$$v = \frac{H\omega}{2} \frac{\cosh(ky)}{\sinh(kD)} \sin(\omega t - kx) \tag{19}$$

For the wave height H, the maximum H_s observed in the hindcast is used (equal to 13 m). For the wave frequency ω, the minimum T_p observed in the hindcast is used (equal to 3 s). y is equal to 200 m, as the maximum water particle velocity occurs in between the wave crest and trough.
In linear water waves calculations, the water depth can be assumed to be deep water, if Equation 20 is true. Here, k equals the wave number and D is the water depth. [52]

$$k \cdot D > \pi \tag{20}$$

Using the dispersion relation in Equation 21, wave number k is computed. Here, g is the gravitational constant, equal to 9.81 m/s^2. [52]

$$\omega^2 = kg \tanh(kD) \tag{21}$$

According to Equation 20, a water depth of 200 m can be considered as deep water for wave periods up to 15.6 s. The total sea histogram in Figure 10.b shows that the far majority of the wave periods satisfy this requirement. Therefore, deep water will be assumed.
In deep water, the dispersion relation can be simplified to Equation 22 [52]. This definition is used for k. Here, λ equals the wave length.

$$k = \frac{\omega^2}{g} = \frac{2\pi}{\lambda} \tag{22}$$

When plotted over time, a maximum water particle velocity of 13.61 m/s is obtained.
Using the lowest equivalent diameter from Table 8 (equal to 47.702 m), a T of 3 s and the computed maximum water particle velocity (equal to 13.61 m/s), the Keulegan-Carpenter number is equal to 0.856, indicating an inertia dominated structure.
A T of 17 s (the maximum T_p present in the hindcast), results in a slightly higher KC (equal to 0.861). This is due to the fact that T is almost cancelled out in the equation for KC (not entirely, since k being dependent on T). As a different T results in such a small difference regarding KC, sometimes the dimensionless number $\frac{H}{d}$ is used to test whether the system is inertia dominated [53].
A diameter of 13.6 m yields $KC = 3$ and a diameter of 2.72 m results in $KC = 15$. This means that for any component with a diameter lower than 13.6 m but higher than 2.72 m (like the pontoon diameter of 7 m, the centre column diameter of 10 m and the outer column diameters of 12.5 m [41]), the drag force should be linearized.
To conclude, this analysis shows it may generally be assumed that the floater is inertia dominated, considering the environmental conditions present in this hindcast. Yet, if the hydrodynamics of the floater would be modelled in more detail, a linearized drag force should be taken into account for the pontoons and the columns.

Relation between wave period and wave height, and $F_{Morison}$
As it has been shown that the structure is inertia dominated, the Morison's equation can be simplified to Equation 23.

$$F_{\text{Morison}} = \rho(1 + C_A)Aa \tag{23}$$

First, the relation between wave period T and F_{Morison} is discussed. These variables are related in two ways.
First of all, the variable C_A is dependent on the wave frequency, due to diffraction. For $\frac{\lambda}{d} > 5$ (where λ equals the wave length and d equals the structure's diameter), diffraction can be neglected and $C_A = 1$. For a lower wave length, the $\frac{\lambda}{d}$-ratio decreases, diffraction increases and $C_A < 1$. Knowing this, Equation 23 shows that diffraction reduces the hydrodynamic force and therefore the fatigue damage at tower base.
Wave length λ can be computed using Equation 22. This equation shows that the wave frequency is directly related to the wave length, and therefore to the diffraction and to hydrodynamic force as well.
The second way that the hydrodynamic force and the wave frequency are related is through the particle acceleration a in Equation 23. Equation 24 shows the formula for a (here, all variables are defined the same as for Equation 19).

$$a = \frac{H\omega^2}{2}\frac{\cosh(ky)}{\sinh(kD)}\cos(\omega t - kx) \tag{24}$$

This formula shows that the amplitude of a depends on ω^2 and that the frequency of a equals ω. As $F_{\text{Morison}} \propto a$ (see Equation 23), F_{Morison} also experiences these relations to ω.
Considering these two facts, two things happen when ω increases [32]:

- First, the hydrodynamic force increases due to $a \propto \omega^2$.
- Second, the hydrodynamic force decreases once ω gets high enough so that $\frac{\lambda}{d} < 5$ and diffraction occurs.

Due to the complex shape of the floater, it is difficult to predict at which ω this turning point occurs, using hand calculation. Therefore, potential flow solvers like WAMIT are used. Yet, these two effects partially explain the peaks shown in Figure 23.
Lastly, the relation between wave height H and F_{Morison} is found by substituting Equation 24 into Equation 23, that results in the relation $H \propto F_{\text{Morison}}$. In addition, the previous section has shown (see comment on the dimensionless number $\frac{H}{d}$) that a structure becomes more inertia dominated as the wave height H decreases.

4.2.3 Wave frequency and floater shape

Using Equation 22, the wave length is computed at the peaks of the transfer functions in Figure 23. These wave lengths are given in Table 9.

Wave direction:	Load:	Frequency:	Wave length:
0°	M_{pitch}	0.119 Hz	110.25 m
90°	M_{roll}	0.115 Hz	118.06 m
	M_{pitch}	0.088 Hz	201.62 m
		0.155 Hz	64.987 m
	M_{yaw}	0.133 Hz	88.264 m
		0.223 Hz	31.396 m

Table 9: Wave lengths computed for the peaks in the first order wave load transfer functions

In Figure 25, these wave lengths are compared to the floater dimensions [41]. This figure shows top views of the floater, where the pontoon diameters are approximately on scale with the design. The green arrow represents the wave direction. The dotted line in the dark blue area represents the highest point on the wave crest and the dotted line in the light blue area represents the lowest point on the wave trough. This figure compares the wave length to the dimensions of the floater.

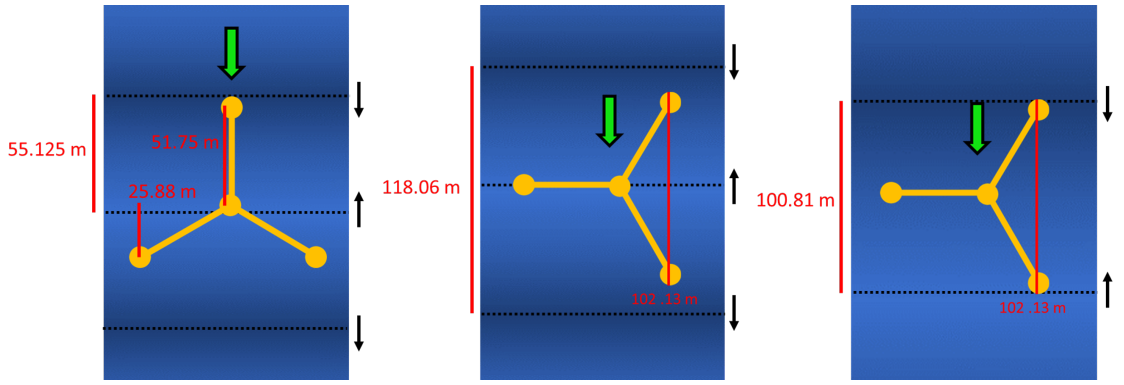

(a) wave direction: 0°
load: M_{pitch}
peak frequency: 0.119 Hz
wave length: 110.25 m

(b) wave direction: 90°
load: M_{roll}
peak frequency: 0.115 Hz
wave length: 118.06 m

(c) wave direction: 90°
load: M_{pitch}
peak frequency: 0.088 Hz
wave length: 201.62 m

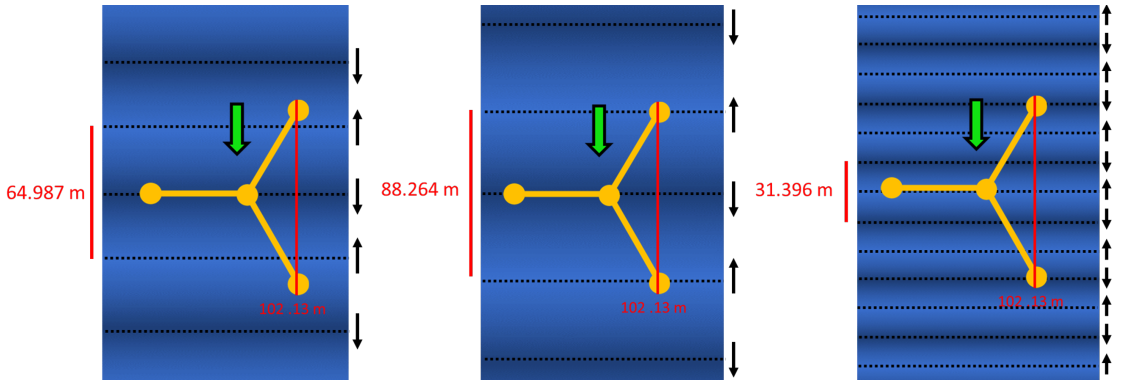

(d) wave direction: 90°
load: M_{pitch}
peak frequency: 0.155 Hz
wave length: 64.987 m

(e) wave direction: 90°
load: M_{yaw}
peak frequency: 0.133 Hz
wave length: 88.264 m

(f) wave direction: 90°
load: M_{yaw}
peak frequency: 0.223 Hz
wave length: 31.396 m

Figure 25: Floater shape (top view) compared to wave length (green arrow: wave direction, black arrows: hydrodynamic force direction) (note: in every figure, the green arrow points in the direction of the pitch motion)

In Figure 25.a, the top column is pushed upwards by the pressure field. On the contrary, the centre and bottom columns, which are more or less in line, fall into the wave trough. This creates a moment in pitch direction. In Figure 25.d, the moment in pitch direction is created by the pressure field pushing the centre column upwards, while the top and bottom columns sink into the wave trough.
In Figure 25.c, the wave length is large enough to carry the floater diagonally on the slope of the wave. The top column experiences a horizontal force in the wave direction, and the bottom column experiences a horizontal force opposed to the wave direction. This creates a coupling moment in pitch direction.
In Figure 25.b the two right columns are pushed upwards by the pressure field of the wave crest and the left pontoon sinks into the wave trough, creating a moment in roll direction.
In Figure 25.e, the middle and left column experience a horizontal force in the wave direction, while the two right columns experience a horizontal force opposed to the wave direction. This creates a moment in yaw direction. The same principle applies to Figure 25.f.
It must be noted that this section aims to show the relation between peaks in the wave

excitation transfer functions and the floater dimensions. The hydrodynamic excitation moment in yaw direction is not expected to have a high contribution to the fatigue damage at tower base.
This section shows that a different wave excitation can be expected for different wave directions (or floater orientations ϕ) and for different wave lengths (direction related to wave period T, as shown by Equation 22). These phenomena, combined with the phenomena described in Section 4.2.2, determine the shape of the transfer functions in Figure 23.

4.2.4 Radiation problem

The matrices M, $a(\omega)$, $b(\omega)$ and C in Equation 16 describe the radiation problem. These matrices are computed by WAMIT and are given in the floater documentation [41].
A characteristic of a time domain analysis is the fact that any motion at any time, is influenced by every motion that has occurred in the past. In frequency domain, this effect is captured in the added mass $a(\omega)$ and damping matrices $b(\omega)$. In time domain, this effect is captured through the retardation functions.
The matrices M, $a(\omega)$, $b(\omega)$ and C determine the rigid body natural frequencies (in other words, the natural frequencies of the floater's motions, or *motion natural frequencies*, given in Table 6). When wave frequency ω approaches one of these natural frequencies, the motion amplitude increases significantly (similarly, the tower vibrations are amplified when (wave) resonance with the tower natural frequency occurs).For example, as the surge motion generally experiences high excitation forces due to wind turbulence, and as the internal surge moment at tower base affects the axial stress (see Equation 7), resonance with the surge natural frequency is likely to increase the fatigue damage significantly.
Various factors influence the four matrices that determine the motion natural frequencies and the system's response to the radiation problem:

- To what extent aerodynamic damping is present (affected by the wind-wave misalignment μ as explained in Section 4.1);
- The mean position of the floater (mainly affected by v, as a higher v results in a higher mean pitch rotation of the system during the 1-hour simulation), which affects the mooring stiffness [7];

The volume, mass and buoyancy of the floater are not affected by any of the environmental parameters T_p, H_s, v, μ are ϕ.
The floater documentation [41] also offers a viscous damping matrix. Viscous damping accounts for the dissipation of energy due to friction between the water and the surface of the structure's outer material. Literature [49] states that viscous damping is of minor importance, as the wave damping described by $b(\omega)$ is dominating. This is due to the fact that wave damping approaches zero, only for very high and very low values of ω. In the unlikely occasion that this is the case, and if the system experiences resonance with the motion eigenfrequencies, then viscous damping will start to affect the floater's motions.

4.2.5 Motion RAO's and stress PSD's due to hydrodynamics

As the axial stress at the tower base is partially caused by the motions and accelerations of the floater, the motion RAO's give an overview of the frequencies (and the corresponding

hydrodynamic effects which are causing the motions at these frequencies), that might have a significant effect on the fatigue damage. The motion RAO's (response amplitude operators) are defined as shown in Equation 25 [54].

$$\text{RAO} = \zeta_a^{-1} X = [-\omega^2 A - i\omega B + C]^{-1} H \tag{25}$$

The RAO's for this turbine model have been created by running a one-hour time domain (wave) white noise load simulation (v = 14 m/s, $\mu = 0°$, $\phi = 0°$), where the wind turbulence and tower shadowing were turned off. Equation 26 shows how the RAO is computed.

$$\text{RAO} = \sqrt{\frac{S_{\text{white noise, motion}}}{S_{\text{white noise, wave}}}} \tag{26}$$

Figure 26 shows the resulting RAO's for the six rigid body degrees of freedom. Negative values in these graphs were caused by the smoothening function applied to the original graphs, which were positive at every frequency. Furthermore, it must be noted that the RAO's are based on a white noise wave spectrum ranging from 0 Hz to 0.6 Hz, as this provides the complete overview of all frequencies that *might* affect the floater motions. As the wave energy of frequencies lower than 0.04 Hz is usually close to zero, resonance with the motion eigenfrequencies unlikely. This will be illustrated later in this section.

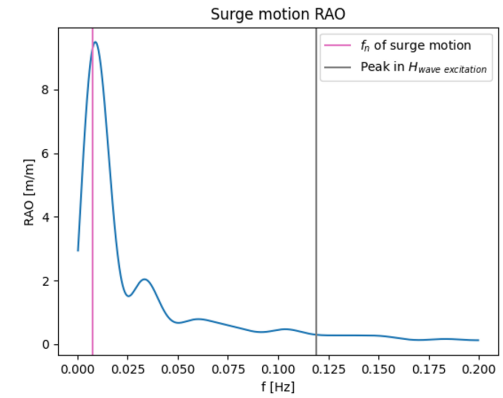

(a) RAO for surge motion

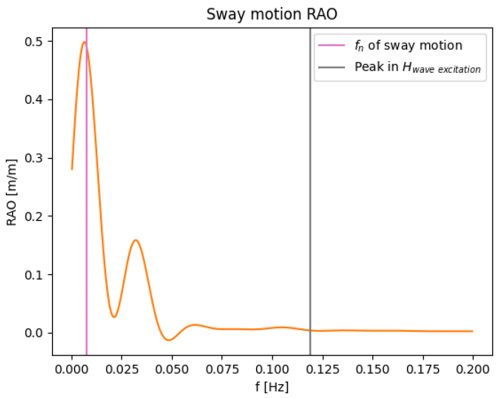

(b) RAO for sway motion

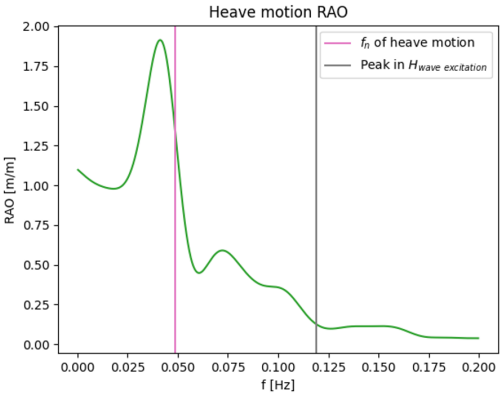

(c) RAO for heave motion

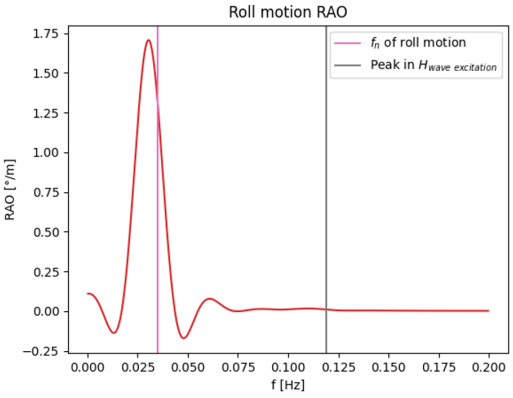

(d) RAO for roll motion

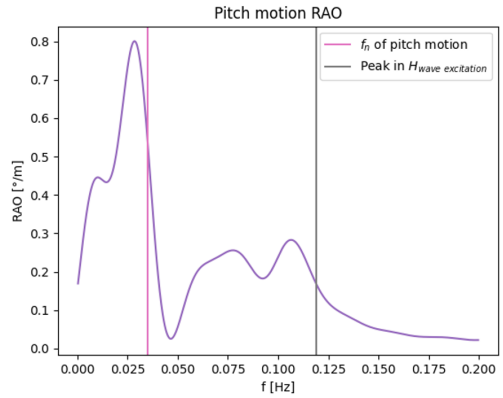

(e) RAO for pitch motion

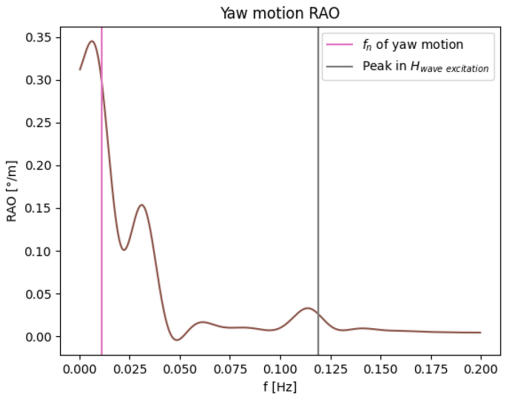

(f) RAO for yaw motion

Figure 26: Motion RAO's computed using a one-hour time domain load simulation (v = 14 m/s, μ = 0°, ϕ = 0°), using a white noise wave spectrum (with wind turbulence and tower shadowing turned off) (black line: motion natural frequency, red line: excitation transfer function peak at 0.12 Hz as shown in Figure 23.c)

Figure 26 shows that the motion RAO's have the highest peaks near the motion natural frequencies, as was predicted in Section 4.2.4. Yet, a small offset is visible. This offset is due to the fact that the motion natural frequencies were derived from the decay test, that assumed a parked turbine and a wind speed close to 0 m/s. The motion RAO's were computed using the results from an operational turbine, with a wind speed of 14 m/s. Due to

thrust, the operational turbine has a slightly different position compared to the parked turbine, and therefore experiences different mooring stiffness. In addition, the parked turbine does not experience aerodynamic damping. These factors result in slightly different matrices in the equation of motion, in Equation 16. For this reason, the motion eigenfrequencies are slightly different for the operational case. This phenomenon as been referred to in Section 4.2.4 as well.
In Figure 26.e, in addition to the pitch natural frequency at about 0.03 Hz, the pitch RAO also shows a relatively broad peak around 0.12 Hz. This peak is caused by the peak at 0.12 Hz in the wave excitation transfer function, shown in Figure 23.c. This proofs that the physics behind the diffraction problem, described in Section 4.2.2 and Section 4.2.3, can affect the motions of the floater, if the wave spectrum shows a high power spectral density at 0.12 Hz.

Analysis of a motion PSD
To illustrate this, a motion PSD is computed using the pitch RAO given in Figure 26.e. The motion RAO is computed using Equation 27, where the RAO is regarded as a transfer function.

$$S_{\text{motion}} = \text{RAO}^2 \cdot S_{\zeta\zeta} \tag{27}$$

In Figure 27, the resulting PSD is shown (labelled as 'Motion PSD FD') and compared to the pitch motion PSD, directly computed using the pitch motion time series resulting from the time domain load simulation (labelled as 'Motion PSD TD'). The sea state (T_p = 16 s, H_s = 6 m) was used for both motion PSD's. Furthermore, the pitch motion natural frequency and the 0.12 Hz peak in the pitch wave excitation transfer function are marked. Lastly, the wave spectrum is plotted.
Three peaks can be distinguished:

- A peak near the eigenfrequency of the motion, at 0.035 Hz (related to the radiation problem);
- A peak at the peak frequency, at 0.0625 Hz (related to the ζ_a term of the diffraction problem);
- A peak near the peak in the wave excitation transfer function, at 0.12 Hz (related to the H term of the diffraction problem). This peak seems to have moved to the left. This is due to the fact that the wave spectrum shows a small power spectral density at 0.12 Hz. An additional test was performed, where the wave excitation transfer functions were replaced by the ones of a spar, that did not show a prominent peak at 0.12 Hz. This causes the peak at 0.12 Hz in the axial stress PSD's to disappear, confirming its relation to the transfer function.

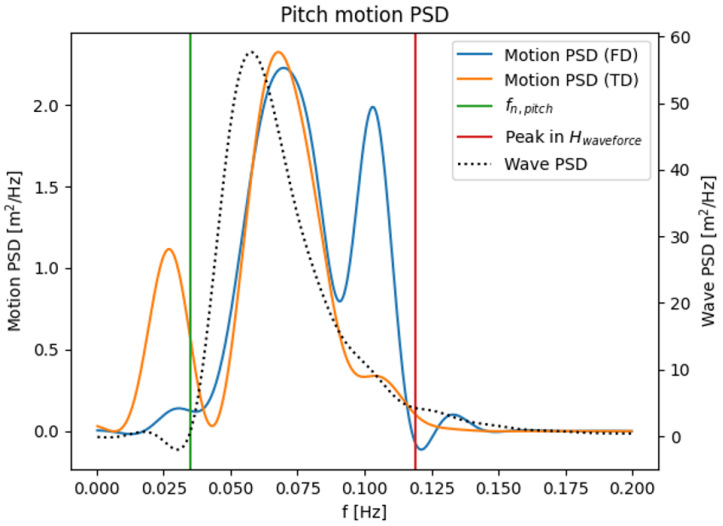

Figure 27: Pitch motion PSD (v = 14 m/s, μ = 0°, ϕ = 0°, T_p = 16 s, H_s = 6 m with wind turbulence and tower shadowing turned off)

Now, the peaks in the motion PSD in Figure 27 will be compared to the axial stress PSD's in Figure 21.b. To recap, these stress PSD's were computed using a time domain load simulation, where wind turbulence and tower shadowing were turned off as well. In the axial stress PSD, where T_p = 16 s and H_s = 6 m, the three peaks described above are visible as well.
Nevertheless, their proportions are different (compared to their proportions in motion PSD's in Figure 27). This is due to the fact that for low wave frequencies, the inertial loads on the structure are proportional to wave frequency ω^2 raised to the power of two, as was proven in Section 4.2.2. Water particle acceleration a at a frequency of 0.105 Hz (the right most peak in the 'Motion PSD FD' graph in Figure 27) will cause loads almost three times as high as the same acceleration at a frequency of 0.0625 Hz (the centre peak in Figure 27 caused by the peak period). This is confirmed by Figure 21.b.

Axial stress PSD's with 90° wave direction
Until now, Section 4.2.5 has focussed on the RAO's, motion PSD's and axial stress PSD's with the 0° wave direction. As Section 4.2.1 has shown, the wave excitation transfer function corresponding to a 90° wave direction are significantly different. For this reason, this section will discuss the axial stress PSD's of a 90° wave direction case, shown in Figure 28. These graphs are computed similarly to Figure 21.b.

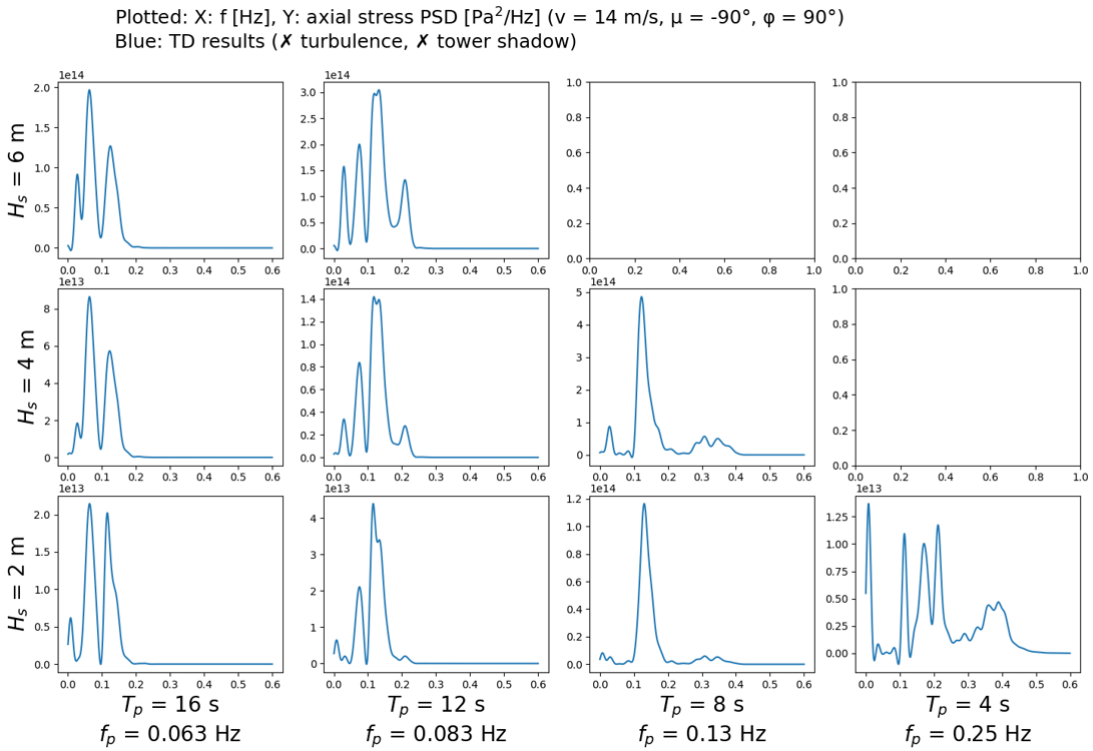

Figure 28: Axial stress PSD's for multiple sea states across the scatter diagram, computed in time domain (wind turbulence and tower shadowing turned off) using a 90° wave direction

The axial stress PSD's in this figure show a higher number of peaks, compared to the axial stress PSD's of the 0° wave direction case, shown in Figure 21.b. This corresponds to the fact that the pitch and roll wave excitation transfer functions of the 90° case show more/higher peaks than the transfer functions of the 0° case (see Table 7 and Figure 23). Like the 0° case, the peaks differ per combination of T_p and H_s for the 90° case, showing again that the hydrodynamics influences the fatigue damage gradient. This chapter has shown why this is the case. This result also confirms that the frequencies that contribute to the fatigue damage gradient may differ per wave direction due to the floater's non-axisymmetric shape.

5 Hydrodynamics accounted for by lumping methods

Section 4 has predicted that the fatigue damage gradient is influenced by wave excitation forces. If the tower and motion natural frequencies are within wave range, they may affect the fatigue damage gradient as well. The gradient is generally unlikely to be affected by aerodynamic and coupling effects.
In order to estimate the fatigue damage gradient, a lumping method assumes a simplified hydrodynamic model. Considering the conclusion in Section 4, this chapter will study whether the simplifications made by the four lumping methods are acceptable or not. It is hypothesized that a lumping method has a higher accuracy if the hydrodynamics that affect the fatigue damage gradient most, are included in its simplified hydrodynamic model. In Section 5.1, the two block partitioning methods Jia and Song & Wang will be discussed and Section 5.2 studies the two contour line methods Katsikogiannis and Seidel. Lastly, Section 5.3 provides a summary of this part's findings.

5.1 Block partitioning methods

When applying a *block partitioning* lumping method, the scatter diagram is first divided in a number of blocks. Then, a lumped sea state is determined for each of these blocks. Literature does not agree on the best method to perform block partitioning. In addition, the accuracy of a lumping method can largely vary for different block partitionings, especially when the structure's first eigenfrequency is within wave range [11].
In order to enable a fair comparison between the different scatter diagrams, a block partitioning algorithm was created. The three approaches below were considered, and the third approach was used.

1. Machine learning clustering methods AffinityPropagation, AgglomerativeClustering, Birch, DBSCAN, KMeans, MiniBatchKMeans, MeanShift, OPTICS, SpectralClustering and GaussianMixture from the Python package Scikit-learn [55] were tested to see whether they are suitable for block partitioning. Some of these method gave moderately good results in some cases, but this was never consistent when being applied to multiple scatter diagrams. Because of this, these methods were regarded as not effective.

2. As machine learning did not give consistently good results, a block partitioning algorithm was written. First, the probability of occurrence (POC) of the sea states was considered to be taken into account. Blocks that contained sea states with a high POC would contain less sea states than blocks with sea states with a lower POC. In this way, the lumped sea state would represent less sea states if these sea states had a high POC, increasing the accuracy of the resulting fatigue damage. This makes sense, as sea states with a high POC weigh heavier for the total fatigue damage of the entire scatter diagram. Nevertheless, taking POC into account would complicate the algorithm significantly. In addition, it is unknown to what extent the accuracy of the lumping method will increase if the POC of the sea states is taken into account. For this reason, the optimal weigh of the POC when performing block partitioning was unknown. Performing a study on block partitioning methods and their effect on lumping accuracy was considered to be beyond the scope of this study. Therefore, the POC of the sea states was not taken into account.

3. Not taking the POC of the sea states into account, the method described in Appendix F

was created. The goal of this block partitioning method was to divide a scatter diagram into blocks, where each block approximately contained the same number of sea states and where all sea states of a block were located together in the scatter diagram.

This latter algorithm resulted in the block partitionings as shown in Figure 29, each having a different average block size.

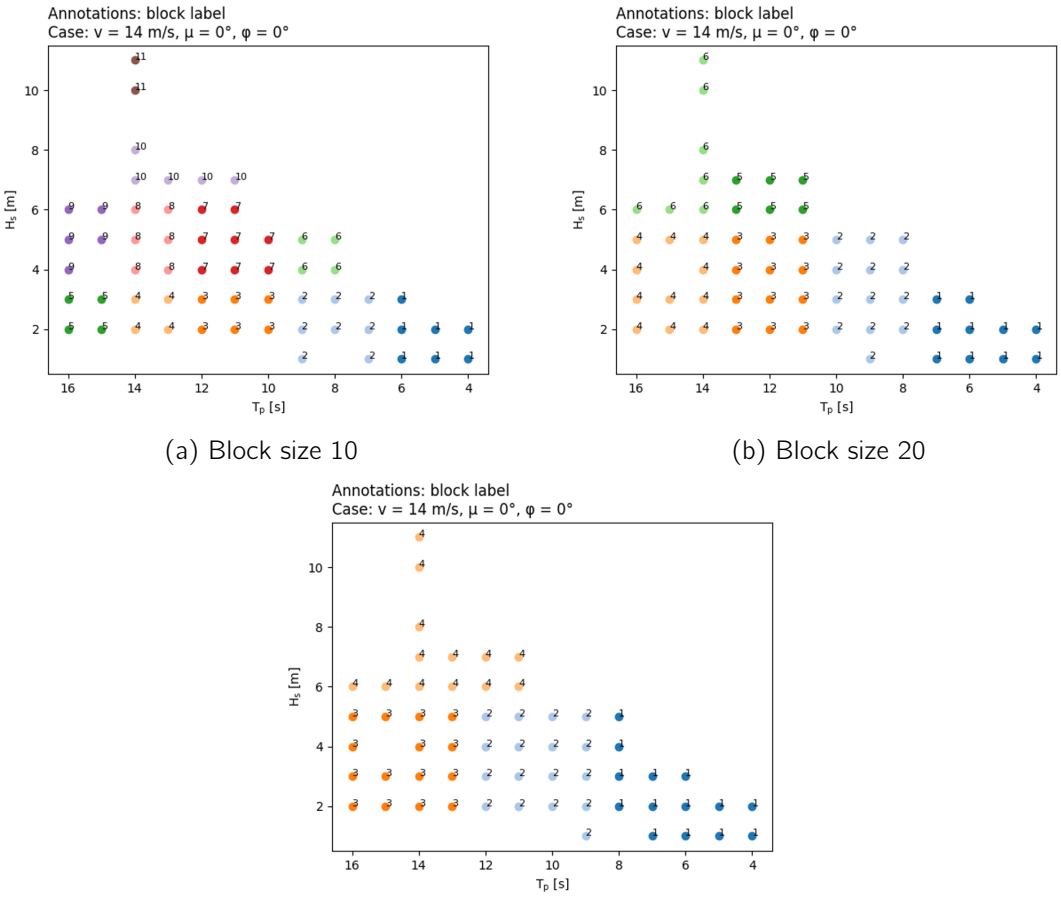

(a) Block size 10

(b) Block size 20

(c) Block size 40

Figure 29: Three ways to perform block partitioning on a scatter diagram, each using a different block size

In order to find the lumped sea state of each block, a lumping method is required, like the Jia or the Song & Wang method. These methods are called *block partitioning lumping methods*, as they are assumed to be too inaccurate to lump the entire scatter diagram at once. Now, the assumptions made by these lumping methods will be discussed and compared to the results found in Section 4.

5.1.1 The Jia method

The Jia method [18] assumes that the system is inertia dominated. Section 4.2.1 shows that this assumption is true for a semi-submersible. Therefore, Morison's equation can be simplified to Equation 23. This equation shows that the hydrodynamic force linearly depends on water particle acceleration a. The formula for a is given in Equation 24. This formula

shows that the frequency of a is proportional to ω and that the amplitude of a is proportional to ω^2 and H. The Jia method neglects the relation between ω^2 and the amplitude of a.
Using the Palmgren-Miner rule, the fatigue damage is estimated using these assumptions. To do so, the Palmgren-Miner rule is rewritten, as shown in Equation 28.

$$D = \sum_{i=1}^{k} \frac{n_i \cdot S_i}{N_i \cdot S_i} = \sum_{i=1}^{k} \frac{n_i \cdot S_i}{K \cdot S_i^{-m} \cdot S_i} = \sum_{i=1}^{k} \frac{n_i \cdot S_i^m}{K} \tag{28}$$

Here, k represents the number of stress bins, S is the magnitude of stress bin i, n is the number of occurrences of stress S as counted by the rainflow analysis and N is the number of occurrences of S that will cause the material to fail as given by the S-N graph. K equals a material parameter, defined as $K = N \cdot S^m$. $\frac{1}{K}$ is equal to $\log(\overline{a})$, which the intercept of the $\log(N)$ axis in the S-N graph (see Appendix D). m equals the slope of the S-N graph and is set to a value of 5 (this decision is justified in Appendix D).
As K is a constant, the fatigue damage is assumed to be proportional to the formula shown in Equation 29. Note that this equation shows a proportional relation. This is because, the lumping method only needs to estimate the fatigue damage gradient, instead of the absolute fatigue damage. This will be further explained in Section 5.2.

$$D \propto \sum_{i=1}^{k} n_i \cdot S_i^m \tag{29}$$

A linear relation between hydrodynamic force F_{Morison} and the internal loads at tower base is assumed. Now, it can be stated that H_s linearly relates to stress range S_i and that T_p linearly relates to the number of stress cycles n_i. According to Equation 29, this means that the fatigue damage is proportional to f_p and H_s^m. These relations are used by the Jia method to compute the lumped sea states, as shown in Equation 30 and Equation 31. The probability of occurrence (POC) of the lumped sea state is given by Equation 32.

$$H_{\text{s,lumped}} = \sqrt[m]{\frac{\sum_{i=1}^{k} n_i \cdot H_{s,i}^m}{\sum_{i=1}^{k} n_i}} \tag{30}$$

$$T_{\text{p,lumped}} = \frac{\sum_{i=1}^{k} n_i \cdot T_{p,i}}{\sum_{i=1}^{k} n_i} \tag{31}$$

$$p_{\text{lumped}} = \frac{\sum_{i=1}^{k} n_i}{n_{\text{total}}} \tag{32}$$

In these formulas, n_i equals the number of occurrences of sea state i, where $i \in \{1...k\}$ where k equals the number of sea states per block. n_{total} equals the total number of occurrences within the entire scatter diagram. $H_{s,i}$ equals the significant wave high of sea state i and $T_{p,i}$ equals the peak period of sea state i.
In summary, the Jia method makes the following assumptions:

1. The hydrodynamic force on the floater is inertia dominated. This assumption acceptable, as shown in Section 4.2.2.

2. The hydrodynamic force linearly relates to the internal loads at the tower base. This assumption is likely to be acceptable, as equation of motion theory and Newton's second law state that $\sum F = m \cdot a$. This shows that any force acting on a rigid body (in this case, the floater) is equal $m \cdot a$, plus any other external force acting on the body.

3. Diffraction (decreasing as ω increases) is neglected. This assumption may not be acceptable. As it has been shown that diffraction influences the fatigue damage, diffraction's dependency on ω shows that diffraction likely affects the fatigue damage gradient (see Section 4.2).

4. The relation between ω^2 and the amplitude of the water particle acceleration a is neglected. This assumption may not be acceptable. As it has been shown that a influences the fatigue damage, a's dependency on ω shows that a likely affects the fatigue damage gradient (see Section 4.2).

5. Load amplifications due to resonance with eigenfrequencies are neglected. This assumption might be acceptable as the eigenfrequencies tend to be outside the wave frequency range, as shown in Section 4.2.5.

5.1.2 The Song & Wang method

The Song & Wang method [20] estimates the fatigue damage according to Equation 33.

$$D \approx m_0^{\gamma m} \tag{33}$$

Here, m_0 is the zeroth spectral moment (equal to the spectral energy) and can be computed using Equation 34. $S_{\zeta\zeta}(T_p, H_s, \omega)$ represents the wave spectrum, as defined in Appendix C.

$$m_0 = \int_0^\infty \omega^0 S_{\zeta\zeta}(T_p, H_s, \omega) d\omega \tag{34}$$

Parameter m equals the slope of the S-N curve and γ is an exponent of spectral wave energy related to the S-N curve slope.
Substituting Equation 33 into Equation 4, yields Equation 35.

$$D_{\text{scatter diagram}} \approx \sum_{i=1}^{N_{ss}} m_{0,i}(T_{p,i}, H_{s,i})^{\gamma m} \cdot n_i = m_{0,\text{lumped}}(T_{p,\text{lumped}}, H_{s,\text{lumped}})^{\gamma m} \cdot \sum_{i=1}^{N_{ss}} n_i \tag{35}$$

$$m_{0,\text{lumped}}(T_{p,\text{lumped}}, H_{s,\text{lumped}})^{\gamma m} = \frac{\sum_{i=1}^{N_{ss}} m_{0,i}(T_{p,i}, H_{s,i})^{\gamma m} \cdot n_i}{\sum_{i=1}^{N_{ss}} n_i} \tag{36}$$

The study found that as the number of sea states that are lumped into a single sea state increases, the accuracy of the lumped sea state decreases. In particular, the study found that a higher number of sea states yields a lumped sea state that overestimates the fatigue damage. For this reason, a correction factor β is applied, as shown in Equation 37. Yet, this correction factor is only of small influence, as for any number of sea states per block its value will be within the range $1 < \beta < 1.02$ (for $m = 5$).

$$\beta = N_{ss}^{\frac{1}{4mN_{ss}}} \tag{37}$$

Equation 38 and Equation 39 show how a lumped sea state can now be selected. Here, $T_{\text{p,lumped}}$ can be calculated using Equation 40 [56].

$$H_{\text{s,lumped}} = 4\beta\sqrt{m_{0,\text{lumped}}} \tag{38}$$

$$T_{\text{z,lumped}} = 2\pi\sqrt{\frac{m_{0,\text{lumped}}}{m_{2,\text{lumped}}}} \tag{39}$$

$$T_{\text{p,lumped}} = T_{\text{z,lumped}} \cdot 1.29 \tag{40}$$

The value for $m_{2,\text{lumped}}$ is found in the same way as $m_{0,\text{lumped}}$, except for the fact that Equation 34 is being replaced by Equation 41.

$$m_2 = \int_0^\infty \omega^2 S_{\zeta\zeta}(T_p, H_s, \omega) d\omega \tag{41}$$

In the paper, the value of γm is found empirically, as shown in Figure 30. To compute this figure, a floating offshore platform model is used; the load calculations are performed in time domain; and the fatigue damage is computed using rainflow counting and the Palmgren-Miner rule. This method similar to the method used in this thesis. Figure 30 shows that $D = m_0^2$ and therefore $\gamma m = 2$.

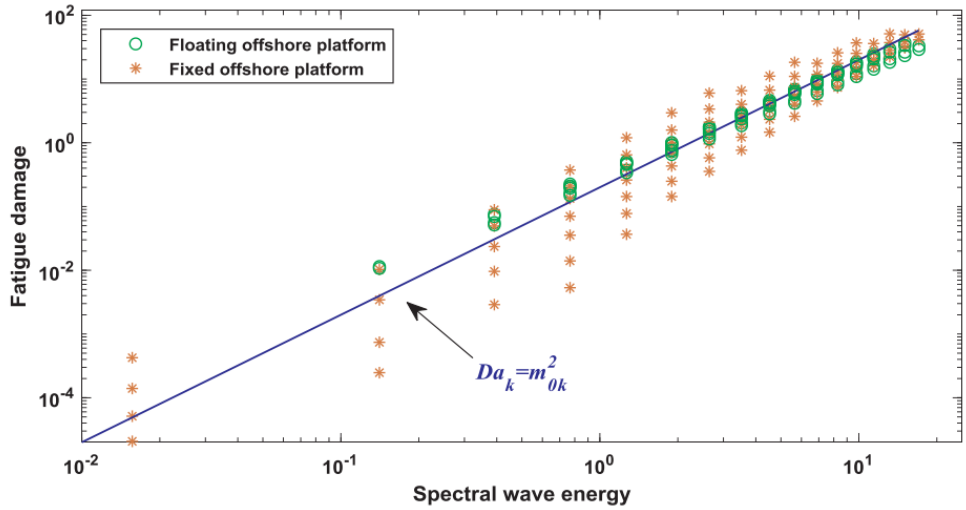

Figure 30: Relation between spectral moment m_0 and the fatigue damage, as found by the Song & Wang paper [20]

Figure 31.a shows the relation between the spectral wave energy and the fatigue damage, computed (in a similar manner as Figure 30) for the semi-submersible in this thesis. In Figure 31.b, the offset is removed (using Equation 42) for an easier comparison. The reason why it is allowed to remove this offset, will be explained in Section 5.2.

$$m_{0,\text{offset removed}}^{\gamma m} = \left(m_0 \cdot \frac{D_{m_{0,\min}}^{\frac{1}{\gamma m}}}{m_{0,\min}} \right)^{\gamma m} \tag{42}$$

This figure shows that for the semi-submersible in this study, the fatigue damage gradient can be estimated by the equation $D \propto m_0^{0.5}$. Note that due to the offset, a proportional sign ($\propto$) is used instead of an equal sign ($=$), and the fatigue damage *gradient* is mentioned, instead of the fatigue damage. In Appendix P, Figure 31.b is shown for the scatter diagrams, where v = 6 m/s and v = 22 m/s. For these scatter diagrams, γm = 0.5 as well.

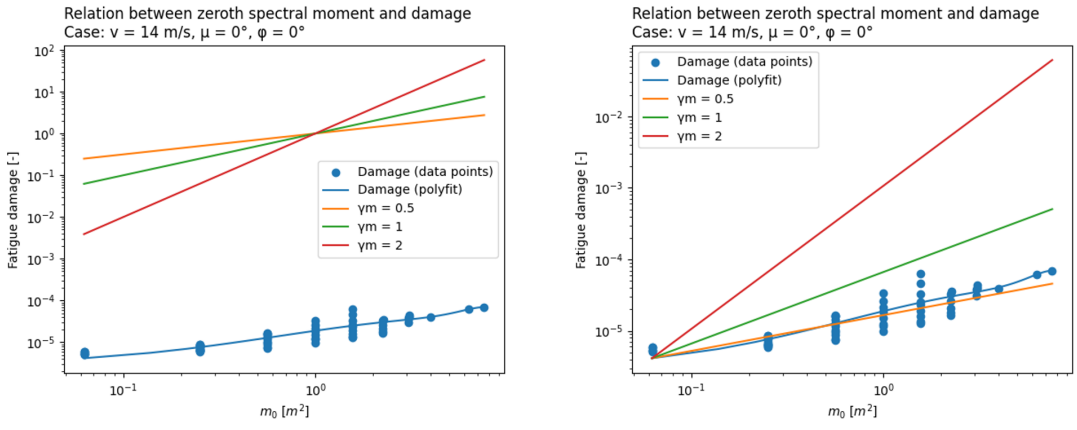

(a) m_0-D relation (original)

(b) m_0-D relation (offset removed)

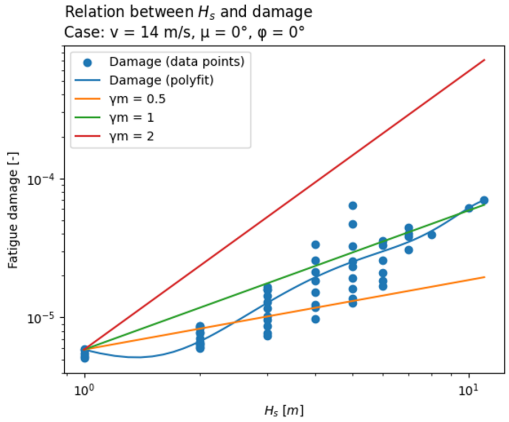

(c) H_s-D relation (offset removed)

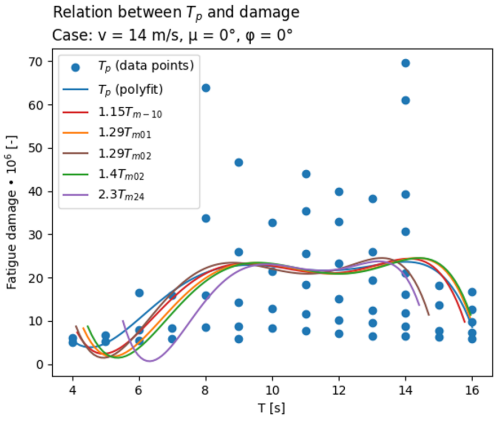

(d) T_p-D relation

Figure 31: Relation between m_0, H_s and T_p, and the fatigue damage

The relation between H_s and D can now be determined, and is shown in Equation 43.

$$D \propto H_s^{2\gamma m} \tag{43}$$

Where the Jia method assumes $D \propto H_s^5$, the original Song & Wang method assumes $D \propto H_s^4$ and the results from Figure 31 show that $D \propto H_s$. Figure 31.c shows that the relation between H_s and D indeed approaches $D \propto H_s^{2 \cdot 0.5} = H_s$, even though the graph shows that this relation is less accurate than $D \propto m_0^{0.5}$.
Lastly, the relation between the wave period and the fatigue damage was investigated. Different methods exist to define wave height: [57]

- **Spectral peak period T_p:** the period where the wave spectrum is maximum;
- **Wave energy period T_e (or T_{m-10}):** the period of a regular wave, that has the same power density and H_s as the wave spectrum, computed by $\frac{m_{-1}}{m_0}$;
- **Mean period T_m (or T_{m01}):** the average period of the wave spectrum, weighed by spectral energy, computed by $\frac{m_0}{m_1}$;
- **Mean zero-upcrossing period T_z (or T_{m02}):** the average period between the wave record upwardly crossing the mean water level, computed by $\sqrt{\frac{m_0}{m_2}}$;

- **Mean crest period T_c (or T_{m24}):** the average period between any decrease in surface elevation in the wave record (in order words, the average period where $\frac{d\eta}{dt} = 0$ and $\frac{d^2\eta}{dt^2} < 0$), computed by $\sqrt{\frac{m_2}{m_4}}$.

The Song & Wang method can compute the m_0, m_2 and m_4 (using a similar computation as used for m_0 and m_2) of the lumped sea state. In the original Song & Wang method T_z is converted to T_p using a correction factor of 1.29. Figure 31.d shows how the other definitions of the wave period approximate the relation between T_p and the fatigue damage. The correction factors were determined by trial and error, using the (v = 14 m/s, μ = 0°, ϕ = 0°) scatter diagram.
Figure 31.d shows $1.29T_{m02}$ that was proposed by the Song & Wang paper combined with the correction factor common in literature [56] resulted in one of the least accurate approximations. In addition, the T_{m24} graph tended to be too narrow, which could not be corrected by the correction factor. Any other definition of the wave period performed well. As Appendix Q shows, these correction factors also resulted in accurate approximations when applied to the v = 6 m/s and v = 22 m/s scatter diagrams.
It is hypothesized that only one scatter diagram needs to be computed in time domain, in order to find the relations $D(H_s)$ and $D(T_p)$, that can be used to approximate all other scatter diagrams accurately. Nevertheless, Section 4 has shown that coupling effects, diffraction effects and even motion natural frequencies may (slightly) change for different scatter diagrams (for different values of v, μ and ϕ). Therefore, this hypothesis cannot be assumed to be true, without further research.
In addition, another improvement could be studied, where Figure 31.c and Figure 31.d are created respectively for each value of T_p and H_s in the scatter diagrams. This is because the fatigue damage gradient, along the T_p axis, differs for different values of H_s. This is due to the fact that a decrease in H_s relates to a more inertia dominated system, that may experience more diffraction effects for lower values of T_p, as was shown in Section 4.2.2. Diffraction effects decrease the fatigue damage, and being related to T_p, they affect the fatigue damage gradient.
For this reason, establishing the $D(T_p)$ and $D(H_s)$ relations for each value of H_s and T_p respectively, may result in a higher lumping method accuracy, while no additional time domain load simulations are required.

5.2 Contour line methods

A contour line method is based on Equation 44. This equation is derived from Equation 3 and Equation 4. Here, N_{ss} equals the number of sea states in the scatter diagram, D_i and n_i respectively equal the damage and NOC of sea state i and D_{lumped} equals the fatigue damage of the lumped sea state.

$$D_{\text{scatter diagram}} = \sum_{i=1}^{N_{ss}} D_i \cdot n_i \approx D_{\text{lumped}} \cdot \sum_{i=1}^{N_{ss}} n_i \tag{44}$$

When a contour line method is used, first the D_{lumped} is computed using Equation 44, where D_i is estimated based on the simplified hydrodynamic model proposed by the lumping method. Then, a fine grid of T_p and H_s combinations is created in accordance with the T_p and H_s range of the scatter diagram. For each sea state in the grid, the fatigue damage is estimated. This can either be done by linear interpolation of D_i (that already has been computed for every sea state in the original scatter diagram) or by (again) using the estimation method

based on the simplified hydrodynamic model. Lastly, all sea states in the grid are marked, that show a fatigue damage equal to D_{lumped}. These sea states are regarded as the lumped sea states, resulting from this lumping method.
If the simplified hydrodynamic model proposed by a lumping method, is replaced by the fatigue damage computed by the time domain load simulation, then the contour line will mark the ideal lumped sea states. In this case, the fatigue damage for every sea state in the grid must be computed using linear interpolation, due to the high computational time of a time domain load simulation. The accuracy of the linear interpolation is shown in Figure 32 and in Appendix L.

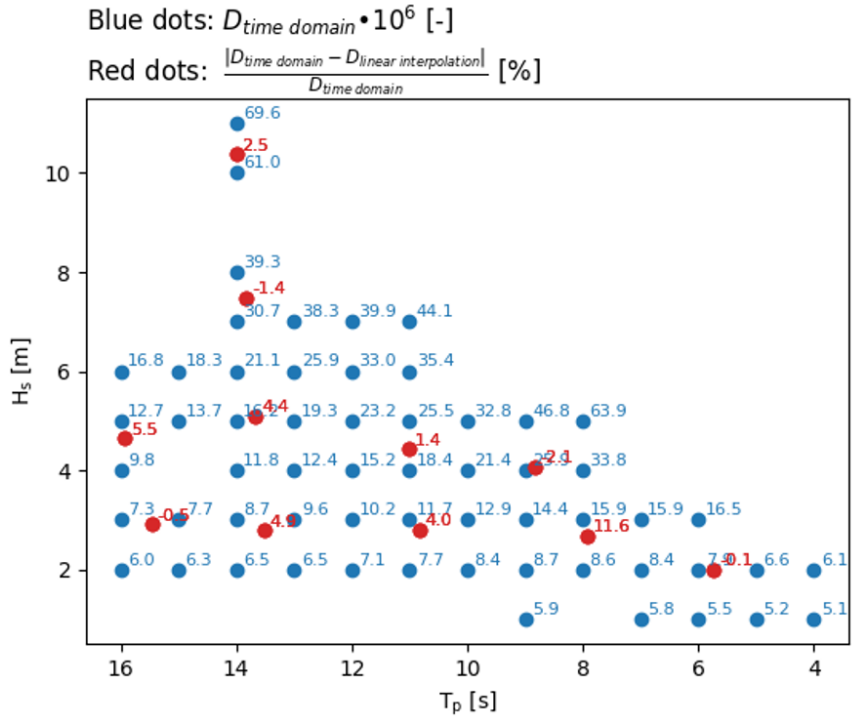

Figure 32: Error (in %) of the fatigue damage computed using linear interpolation, compared to the fatigue damage computed in time domain analysis, for eleven random points in the scatter diagram

The lumped sea states marked by this contour line are *ideal* as they will show a fatigue damage error of 0%. This can be proven when Equation 45 is substituted in Equation 5. For this reason, this contour line will be called the *control contour line*. The better that a contour line lumping method approaches this control line, the higher its accuracy.

$$D_{\text{scatter diagram}} = \sum_{i=1}^{N_{ss}} D_i \cdot n_i = D_{\text{lumped, ideal}} \cdot \sum_{i=1}^{N_{ss}} n_i \tag{45}$$

In Figure 33, the control contour line is plotted for an example scatter diagram. As this figure shows, the control line is not affected by different wind seeds. In Appendix M the contour lines of the v = 6 m/s and the v = 22 m/s scatter diagrams can be reviewed.

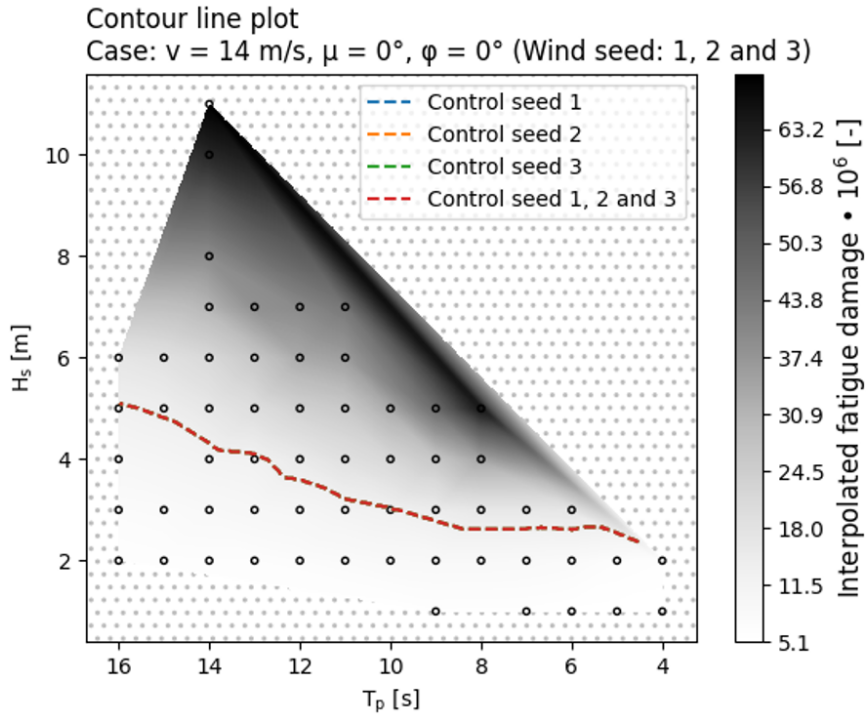

Figure 33: Control contour line for different seeds

The colour gradient visible in Figure 33 represents the fatigue damage computed for every sea state in the grid, using interpolation. The change in colour represents the change in fatigue damage over T_p and H_s, also called the *fatigue damage gradient*.
Figure 34 illustrates why a lumping method should be able to estimate the fatigue damage gradient, in contrast to the absolute fatigue damage. In this figure is for illustrative purposes only and is not based on real data. Here, the fatigue damage, named D_{real}, is plotted over H_s only, yielding a 2D figure. The lumped H_s, computed using the method described above, is marked by the dotted line. Next, several graphs are plotted that aim to estimate the D_{real} graph, as a lumping method would.

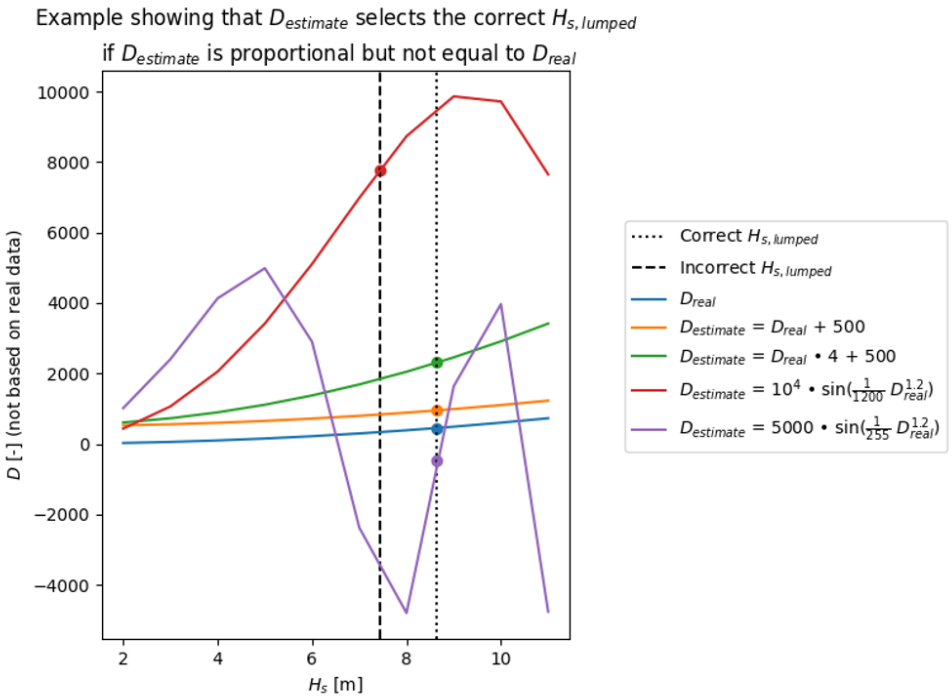

Figure 34: Accuracy of a contour line lumping method is not affected by an offset or a factor applied to the estimated fatigue damage

This figure shows that $D_{estimate}$ results in the same lumped H_s as D_{real}, when $D_{estimate}$ is equal to D_{real}, summed an offset of 500, and/or multiplied by a factor 4 (see orange and green graphs).
This illustrates that the fatigue damage estimated by the simplified hydrodynamic model of a lumping method may be *proportional*, rather than *equal*, to the absolute fatigue damage, in order to find the lumped sea state. For this reason, the offset to the fatigue damage found by the Song & Wang method (using different values of γm) when compared to the real fatigue damage, could be neglected in Figure 31.b. It must be noted, that the offset visible in the figure represents a multiplication by a factor, due to the logarithmic axes.
In addition, a pitfall is to believe that an offset between the contour line generated by a lumping method and the control contour line, is caused by an offset between the estimated fatigue damage and the real fatigue damage. The fact that this is false, is illustrated by the red graph in Figure 34. The lumped H_s of the red graph (marked by the striped line) shows an offset of about 1 m, compared to the correct lumped H_s. The figure shows that this offset is due to the different *shape* of the red graph. As explained before, an offset between the estimated fatigue damage and the real fatigue damage does not affect the resulting lumped sea state.
Finally, the purple line in Figure 34 shows that it is statistically possible that the estimated change in fatigue damage over H_s does not approach the real fatigue damage gradient at all, but still results in the correct lumped H_s. Yet, it is expected that the lumping method that generated this incorrect fatigue damage gradient will show an extremely low accuracy for other cases (like other scatter diagrams and other hindcasts). This phenomenon shows that only measuring the fatigue damage error using Equation 5 without investigating the validity of the hydrodynamic model assumed by the lumping method, is not enough to draw a conclusion on its accuracy.
In this study, Figure 33 will be shown more often with additional contour lines plotted, that

were generated by lumping methods, in order to show how these methods behave compared to the control. It must be noted that this figure may be misleading when used to compare lumping method accuracies of different methods, if the following is not taken into account:

- The fact that the contour line generated by a lumping method that approaches the control line, does not guarantee that this lumping method is capable of estimating the fatigue damage gradient accurately, as shown by Figure 34.
- The change in fatigue damage per H_s and per T_p is not equal across the entire scatter diagram. For example, as H_s increases, the increase in the fatigue damage starts to increase. For this reason, if the control contour line is located higher in the scatter diagram, a visibly small offset between contour lines represent a much larger fatigue damage error than when the contour lines are located lower in the scatter diagram. For this reason, contour lines in figures like Figure 33 cannot easily be compared among different scatter diagrams.

The Katsikogiannis method and the Seidel method offer two ways to estimate the fatigue damage gradient, without having to compute time domain load calculations for every sea state in the scatter diagram. Their methods will now be discussed.

5.2.1 The Katsikogiannis method

The Katsikogiannis method estimates the fatigue damage gradient by computing the fatigue damage in frequency domain. By substituting this fatigue damage into Equation 44, the contour line can be computed. To perform the frequency domain computation, a white noise simulation is run in time domain, in order to obtain the stress transfer function $H_{\zeta\sigma} = \sqrt{\frac{S_{\sigma\sigma,\text{ white noise}}}{S_{\zeta\zeta,\text{ white noise}}}}$. Next, any given wave spectrum can be multiplied by $H^2_{\zeta\sigma}$ in order to find the stress spectrum. Using Rainflow counting, the fatigue damage can now be determined. Appendix E describes this method in more detail.
In the white noise time domain simulation, wind turbulence and tower shadowing are turned off. This is done for the following two reasons:

- The transfer function raised to the power of two is multiplied with the wave spectrum to compute the axial stress PSD. If wind turbulence and tower shadowing would be turned on in the time domain simulation, their effects would show up in the transfer function. It cannot be physically justified to multiply these effects with the wave spectrum.
- The Katsikogiannis method assumes that coupling effects between wind and waves can partially be neglected (as the wind speed corresponding to the scatter diagram is used in the white noise load simulation, some coupling effects are included in the transfer function and are multiplied by the wave spectrum). Section 4.1 has shown that this is an acceptable simplification. Because of this, the effects of the wind turbulence and tower shadowing are assumed to be constant for every sea state in the scatter diagram, where wind speed v is constant. If they are excluded from the fatigue damage computation, the fatigue damage may end up lower than the real fatigue damage (computed using a time domain load analysis including wind effects). Yet, as Figure 34 has shown, an offset in fatigue damage does not decrease the accuracy of a lumping method. Therefore, it is valid to exclude wind effects from the white noise load computation.

Figure 35 shows the fatigue damage, computed using this frequency domain method, as well as the corresponding Katsikogiannis contour line. It must be noted that the absolute fatigue damages computed, differ significantly to the values computed in Figure 19. Yet, as Figure 34 has shown, an offset or scaling factor applied to the absolute fatigue damage does not affect the accuracy of a contour line lumping method.

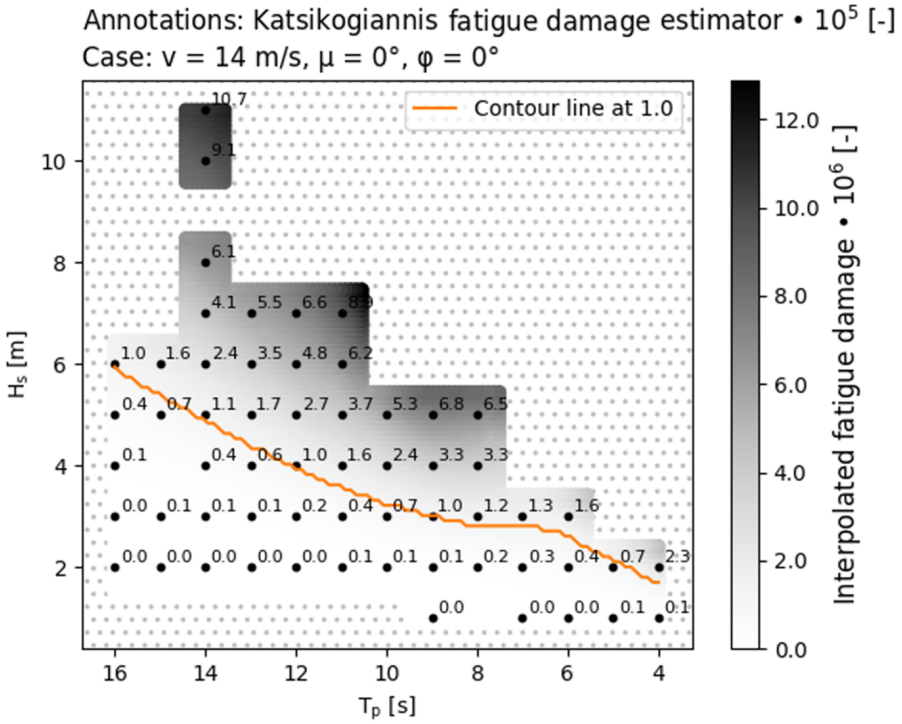

Figure 35: Contour line resulting from the Katsikogiannis method

Interestingly, in practice, the Katsikogiannis contour line increased in accuracy when wind turbulence and tower shadowing were included in the time domain simulation, as shown in Figure 36. In the case where these wind effects were not included, the contour line is less accurate for higher T_p's.

This might be due to the fact that the effect of T_p and H_s on coupling effects is partially neglected by the Katsikogiannis frequency domain method. As Section 4.1 showed, coupling effects mainly occur when wind and waves are aligned. In those cases, the aerodynamic damping reduces the pitch motion resonance in a coupled system. In the decoupled system used by the Katsikogiannis method, this effect is partially present, as the stress transfer function is computed using a time domain load simulation of a coupled system. Yet, the effect that wave period might have on the *decrease* in pitch resonance in a coupled system compared to a decoupled system, is not taken into account. In addition, in Section 4.1 previous research [48] showed that coupling between wind and waves almost does not affect the stresses in the wave frequency range and higher. The fact that mainly the pitch resonance is affected by coupling might explain why Figure 36.a shows a higher accuracy at lower T_p's, that approach the pitch natural frequency.

Nevertheless, the higher accuracy observed when turbulence and tower shadowing are included in the white noise load simulation, is likely to be a coincidence. This is because, as stated before, the multiplication of the wave spectrum with turbulence and tower shadowing effects cannot be physically justified. For this reason, the higher accuracy for the transfer function that included these wind effects cannot be guaranteed for other cases

(like scatter diagrams, hindcasts or structures), and it is still advised to exclude wind turbulence and tower shadowing from the transfer function load computation.
This theory is confirmed by the orange graphs in Figure 37 (FD results, excluding turbulence and tower shadowing from white noise simulation) and Figure 38 (FD results, including turbulence and tower shadowing in white noise simulation), as Figure 38 shows higher resonance at the pitch natural frequency, while coupling effects (resulting from including turbulence and tower shadowing) are supposed to reduce pitch resonance. This confirms that including these wind effects does not have a physical meaning.
Lastly, it must be noted that, as tower shadowing effects are small, including or excluding them from the time domain simulation did not affect the Katsikogiannis contour line. Yet, for a physically justifiable model, it is advised to exclude them.

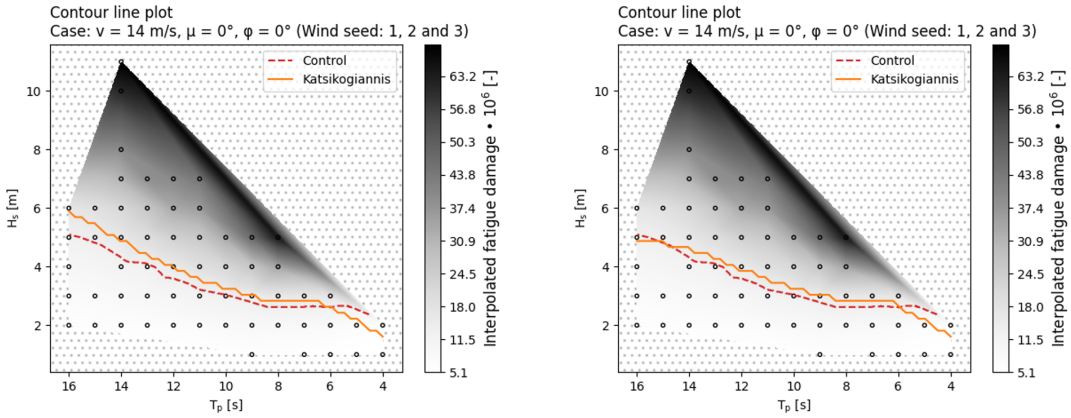

(a) Wind turbulence and tower shadowing are turned off

(b) Wind turbulence and tower shadowing are turned on

Figure 36: Katsikogiannis contour lines in case wind turbulence and tower shadowing are turned on and turned off in the white noise time domain simulation

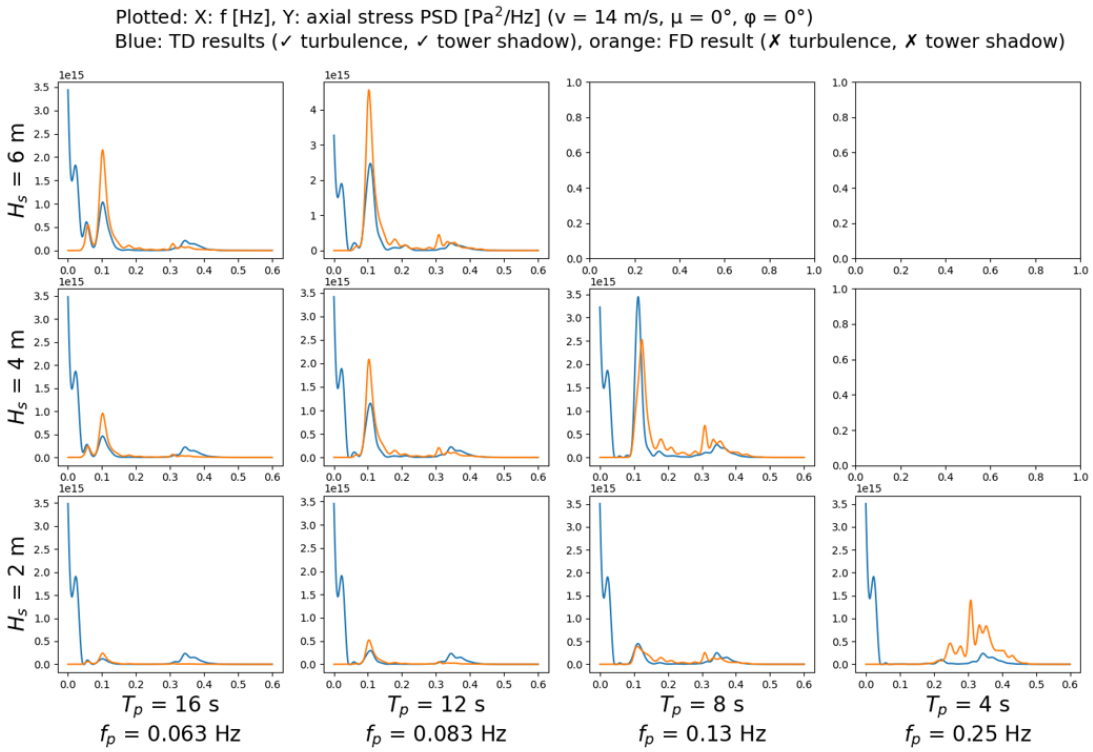

Figure 37: Axial stress PSD's for multiple sea states across the scatter diagram, computed in time domain (blue line, wind effects turned on) and in frequency domain (orange line, wind effects turned off)

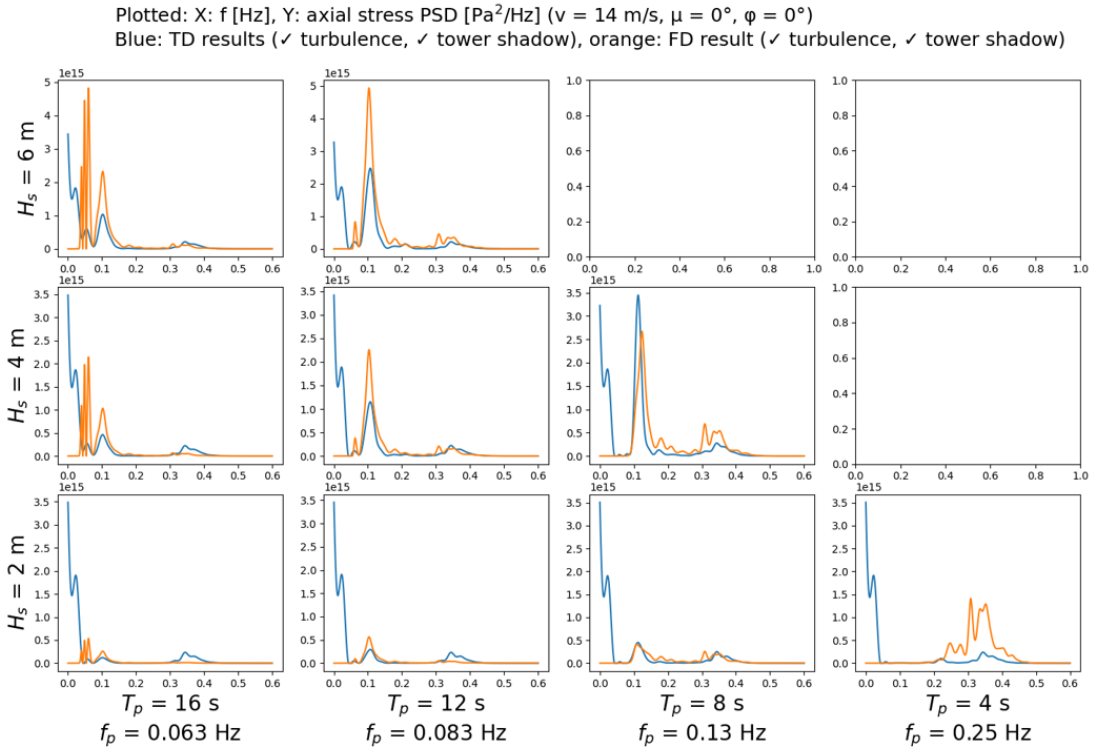

Figure 38: Axial stress PSD's for multiple sea states across the scatter diagram, computed in time domain (blue line) and in frequency domain (orange line) with wind effects turned on for both cases

5.2.2 Comparison of the Katsikogiannis method between monopile and semi-submersible

In the Katsikogiannis paper [9], the method was applied to a monopile. In this section, the contour line resulting from this monopile is compared to the contour line resulting from this semi-submersible studied in this thesis. Regarding the fatigue damage gradient, the main difference between a monopile and a semi-submersible is the fact that a monopile's natural frequency often lays within the wave frequency range. This causes the fatigue damage gradient to be dominated by the structure's natural frequency rather than the wave excitation. When offshore turbines are designed, the developer has the following three choices regarding the first natural frequency of the tower f_n:

- A soft-soft design: f_n is lower than the 1P range;
- A soft-stiff design: f_n is in between the 1P and the 3P range;
- A stiff-stiff design: f_n is higher than the 3P range.

For the semi-submersible in this study, 0.083 Hz to 0.125 Hz equals the 1P range ranges and 0.249 Hz to 0.378 Hz equals the 3P range. As the first natural frequency of the tower is equal to 0.4181 Hz, this turbine is designed according to the stiff-stiff design.
Due to the wind turbulence and wave frequency ranges, a soft-soft design is often not possible. For a floating turbine, a stiff-stiff design can be a realistic option, while for a bottom fixed monopile generally a soft-stiff design is used. This is because, a floating turbine is likely to have a higher natural frequency than a monopile. This is due to the following two reasons:

1. Figure 39 shows that an offshore wind turbine can be represented as a mass m and a rod with length L and diameter D. The mass m represents the RNA mass. In this simplified model, both m and D are assumed to be equal for both designs. Length L is much greater for the monopile than for the semi-submersible. Assuming a thrust force is applied to the rotor, the stiffness of the rod, assuming a cantilever with one fixed end (strictly seen a false assumption for a floating turbine, see the next point), is given by Equation 46, where E is the Young's modulus of the material. This formula shows the stiffness k decreases as L increases, assuming D is constant. Equation 47 shows the formula to compute the natural frequency of a system and shows that the ω_n decreases as k decreases, assuming a constant m. This shows that due to its higher L, monopiles generally have a lower stiffness k and therefore a lower natural frequency ω_n than semi-submersibles.
2. Where a fixed monopile can be modelled as a cantilever with a fixed end as assumed by Equation 46, a semi-submersible cannot. Rather, the bottom end of the semi-submersible's rod should be modelled as a collection of springs and dampers. This is because, as the semi-submersible floats, it is free to move in surge, sway, heave, pitch, roll and yaw direction. Energy in the system (for example added by external forces or an initial displacement) can be converted into elastic energy or kinetic energy. Due to its fixed end, for a monopile, the energy is mainly converted into elastic energy, in the form of tower bending and some soil deformation. In contrast, for a semi-submersible, energy is also converted into elastic energy resulting from buoyancy (acting as a spring in vertical direction), elastic energy stored by the mooring lines, and kinetic energy in the form of floater motions. Therefore, for a semi-submersible, less energy will be need to be stored as elastic energy through tower bending. This results in smaller

tower deformations for a semi-submersible compared to a monopile, even when the same amount of energy is added to the system. As stiffness is defined as the applied load divided by the resulting deformation, the semi-submersible is likely to have a higher stiffness than a monopile, even if the monopile and its tower would have the same total length as the semi-submersible's tower. Again, as shown by Equation 47, a higher stiffness leads to a higher natural frequency. It must be noted that for both the monopile and the semi-submersible, the tower deflections and/or structural motions may be damped by factors like aerodynamic damping and damping caused by the water's inertia, dissipating the elastic and kinetic energy.

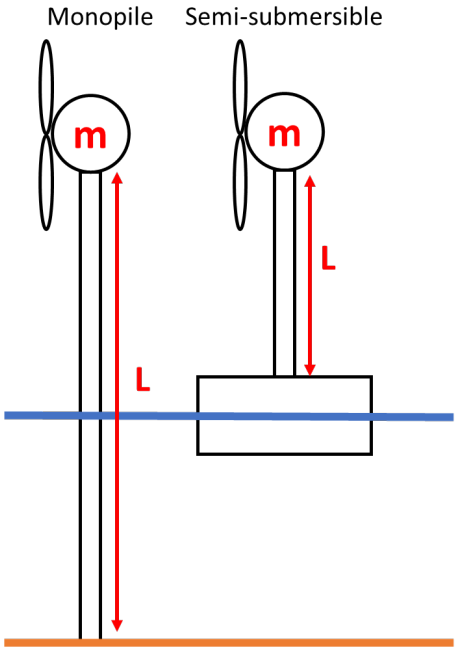

Figure 39: A monopile and a semi-submersible simplified to a rod with diameter D and length L with a point mass m on top

$$k = \frac{3\pi E D^4}{64 L^3} \tag{46}$$

$$\omega_n = \sqrt{\frac{k}{m}} \tag{47}$$

In the Katsikogiannis paper [9], a monopile was used with a soft-stiff design, where the first fore-aft tower natural frequency was equal to 0.2598 Hz. This contour line was extracted from the paper and is plotted in orange in Figure 40.a, where a clear dip is visible near at the eigenperiod.

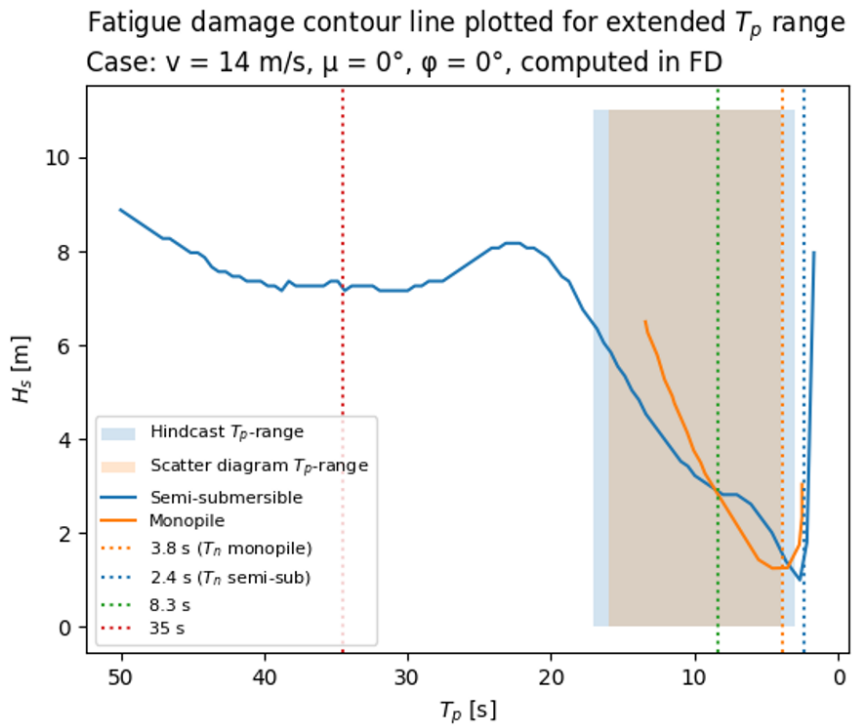

(a) Contour lines plotted against T_p

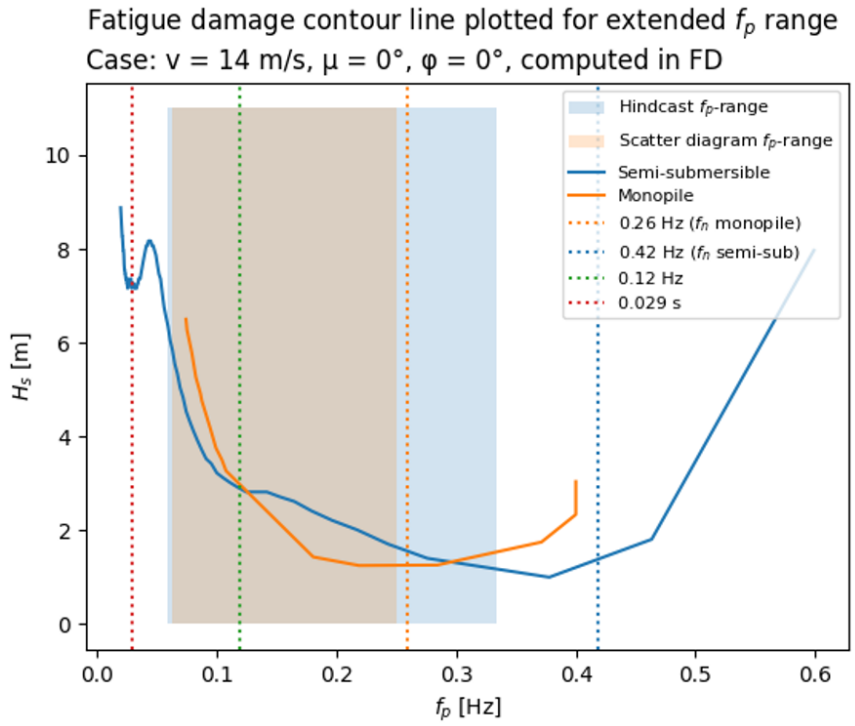

(b) Contour lines plotted against f_p

Figure 40: Fatigue damage contour lines computed in frequency domain (Katsikogiannis method) for a monopile [16] and a semi-submersible, for a manually extended (a.) T_p range and (b.) f_p range

This dip is caused by the fact that resonance of T_p with the eigenperiod results in an increased fatigue damage. Due to the increase in fatigue damage compared to other T_p's, D_{lumped}

(see Equation 44) is reached at a lower H_s. It must be noted that more recent monopiles are being designed with even lower first structural natural frequency [7]. For these monopiles, the contour line dip will be located even more towards the centre of the scatter diagram, than the orange line is showing.
The blue line represents the contour line (computed using Katsikogiannis' frequency domain method) of the semi-submersible in this study. Note that the section of the blue line within the scatter diagram's T_p-range (marked in beige) is mathematically equal to the Katsikogiannis contour line in Figure 36.a.
The T_p range has been extended to unrealistically high and low values, in order to show that, as the monopile, the semi-submersible also shows a large dip at its first tower natural frequency (see the dotted line at T_p = 2.4 s and f_p = 0.42 Hz). Nevertheless, as its first tower natural frequency is outside the T_p range of the hindcast, the lowest point of this dip is not observed in the semi-submersible contour line, when plotted for a scatter diagram.
On the other hand, the semi-submersible line does show a kink in the graph around T_p = 8.3 s. This dip corresponds to the peak in the wave excitation transfer function at 0.12 Hz, that was identified and explained in Section 4.2.1. When the T_p approaches 0.12 Hz, the wave spectrum shows a peak at 0.12 Hz as well. Now, the multiplication of the wave spectrum with the wave excitation transfer function cause the wave excitation to increase significantly. This results in an increase in fatigue damage at T_p = 0.12 Hz, resulting in a lower lumped H_s. The lowered lumped H_s causes a kink in the contour line visible in Figure 40 at T_p = 8.3 s and f_p = 0.12 Hz.
Figure 10 shows that the swell waves of this hindcast have about the same T_p range as the total sea waves. The wind waves have a much lower T_p range and do include the natural period of the semi-submersible tower. In this case, the first tower natural frequency will have a larger effect on the fatigue damage gradient of the semi-submersible.
Lastly, the dip at T_p = 35 s and f_p = 0.029 s is caused by resonance with the eigenfrequencies of the floater's motions. Yet, Figure 10 shows that this hindcast does not contain peak periods higher than 16 s. For this reason, the motion natural frequencies are unlikely to affect the fatigue damage gradient for this hindcast.

5.2.3 The Seidel method

When applying the Seidel method [25], a frequency ω_{Seidel} must be chosen. In the Seidel paper, where the lumping method was applied to a bottom fixed monopile, the first natural frequency of the structure is used. At this frequency, the power spectral density of the wave spectrum $S_{\zeta\zeta}(\omega_{\text{Seidel}})$ (as defined in section Appendix C) is computed. The Seidel paper offers an advanced mathematical derivation, that proves that the damage equivalent loads (DELs) may be assumed to be proportional to $\sqrt{S_{\zeta\zeta}(\omega_{\text{Seidel}})}$. In addition, $D = \text{DELs}^m$. Note the similarity of this equation to the Palmgren-Miner rule in Equation 28, where the fatigue damage is computed using the axial stress ranges S, raised to the power of m, where m is the slope of S-N curve (set to a value of 5, see Appendix D). Now, the fatigue damage can be estimated using Equation 48.

$$D \propto \sqrt{S_{\zeta\zeta}(T_p, H_s, \omega_0)}^m \tag{48}$$

Substituting Equation 48 into Equation 44, yields Equation 49. This equation can be rewritten as the equation stated in the Seidel paper [25], shown in Equation 50.

$$D_{\text{scatter diagram}} \propto \sum_{i=1}^{N_{ss}} \sqrt{S_{\zeta\zeta}(T_{p,i}, H_{s,i}, \omega_0)}^m \cdot n_i = \sqrt{S_{\zeta\zeta}(T_{p,\text{lumped}}, H_{s,\text{lumped}}, \omega_0)}^m \cdot \sum_{i=1}^{N_{ss}} n_i \tag{49}$$

$$\sqrt{S_{\zeta\zeta}(T_{p,\text{lumped}}, H_{s,\text{lumped}}, \omega_0)} = \left(\frac{\sum_{i=1}^{N_{ss}} \sqrt{S_{\zeta\zeta}(T_{p,i}, H_{s,i}, \omega_0)}^{m} \cdot n_i}{\sum_{i=1}^{N_{ss}} n_i} \right)^{\frac{1}{m}} \tag{50}$$

Now, a fine grid is created of T_p and H_s combinations, covering the T_p and H_s ranges of the scatter diagram. Based on the left-hand side of Equation 50, $\sqrt{S_{\zeta\zeta}(T_p, H_s, \omega_0)}$ is computed for every sea state in the grid. The right-hand side of Equation 50 is computed using the original sea states in the scatter diagram. A contour line is plotted where the grid equals the right-hand side of the equation, thereby marking the lumped sea states according to the Seidel method.
The grid, the gradient across the grid based on the left-hand side of Equation 50 and the contour line are shown in Figure 41.

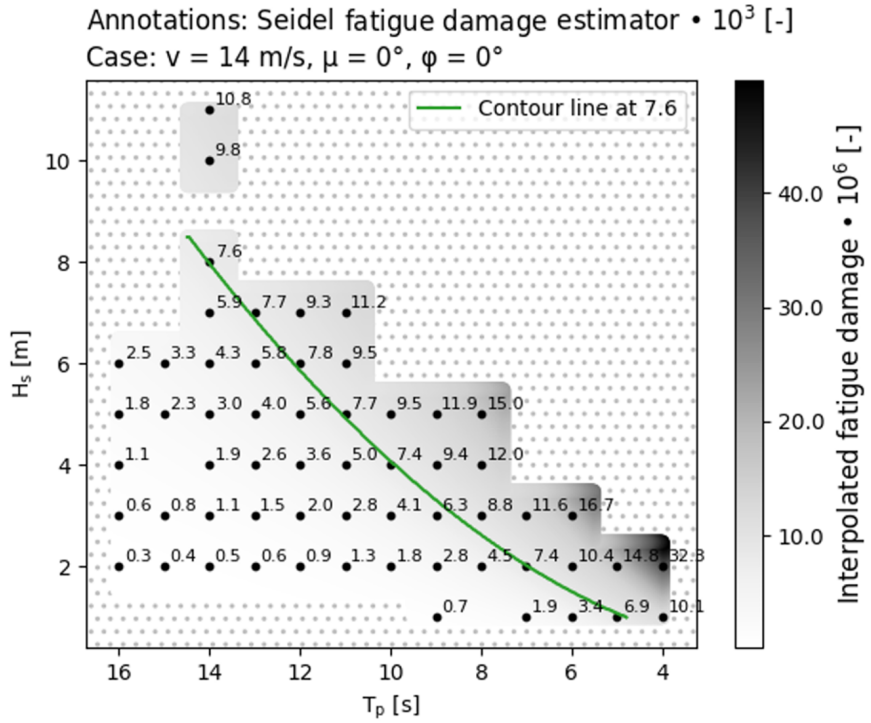

Figure 41: Contour line resulting from the Seidel method

In short, the Seidel method assumes that a single wave frequency dominates the stress PSD. Section 4.2.5 has shown that this is not the case for the semi-submersible studied in this thesis. Instead, multiple peaks are visible, originating from peaks in the wave excitation transfer function and T_p in the wave spectrum.
On the other hand, Section 5.2.2 has shown that for a monopile the structure's natural frequency does dominate the fatigue damage gradient, as it lays within the wave frequency range. For this reason, the high accuracy of the Seidel lumping method that was observed in previous research, when applied to a monopile, is a plausible result. Yet, it is unlikely that the Seidel method will perform this well, when applied to a semi-submersible.
In Figure 42, several Seidel contour lines are plotted, using different values for ω_{Seidel}. These figures show that the shape of these Seidel contour lines differs greatly.

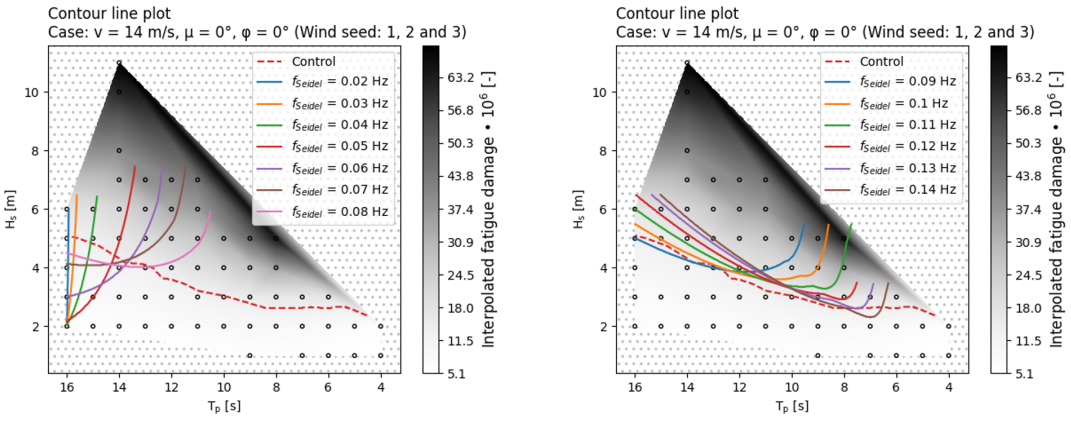

(a) Wind frequency range

(b) Wave frequency range

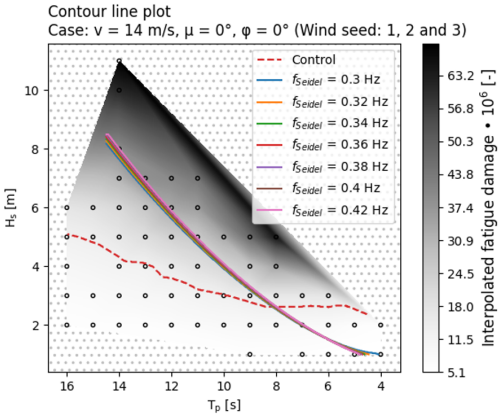

(c) 3P and tower natural frequency range

Figure 42: Seidel contour lines plotted for different values of f_{Seidel}.

Figure 42 shows that, for the ($v = 14$ m/s, $\mu = 0°$, $\phi = 0°$) scatter diagram, the Seidel contour line approaches the control contour line best, when ω_{Seidel} lays within the wave frequency range. This is due to the fact that the wave excitation transfer function corresponding to this wave direction is dominated by a single peak around 0.12 Hz, as discussed in Section 4.2.1. Yet, as Figure 21.b shows, the peak at 0.12 Hz is not the only peak showing up in the axial stress PSD's. Because of this, no contour line in Figure 42 approaches the control line with a high accuracy. It is expected that the accuracy of this lumping method will be even worse for scatter diagrams with a 90° wave direction, like the one used to generate the axial stress PSD's in Figure 28. To conclude, the Seidel method is unreliable for a semi-submersible, unless the user has in depth knowledge about Seidel's assumptions and knows how to check Seidel's validity for a specific floater design, as was shown in this section.

5.3 Summary

Before continuing to the next part, where the results of the lumping method performance tests will be discussed, the findings from Section 4 and Section 5 will be discussed in this section.

First, an overview will be provided of the relation between the fatigue damage at different wave frequencies ω and the structure's natural frequencies, for a semi-submersible and a monopile. This example will assume a semi-submersible tower natural frequency of 0.41

Hz, and a monopile structural natural frequency of 0.2 Hz. The semi-submersible's higher natural frequency is mainly due to its short tower length and its boundary condition, that allows floater motions (allowing internal energy to be converted to kinetic (motions) and elastic energy (mooring lines, buoyancy), as well as of tower vibrations).
For the semi-submersible:

- For $\omega < 0.05$ Hz, the fatigue damage is dominated by resonance with the motion eigenfrequencies, and will likely peak around 0.03 Hz. Coupling effects (dependent on v and μ) between the aerodynamic damping and the pitch motion may lower the pitch motion resonance;
- For $0.05 \text{ Hz} < \omega < 0.41$ Hz, the fatigue damage generally increases, as it approaches the tower natural frequency of 0.41 Hz;
- For $\omega > 0.41$ Hz, the fatigue damage decreases, as the wave frequency gets further removed from the tower natural frequency.

For the monopile:

- For $\omega < 0.2$ Hz, the fatigue damage increases, as it approaches the structural natural frequency of 0.2 Hz;
- For $\omega > 0.2$ Hz, the fatigue damage decreases, as the wave frequency gets further removed from the structural natural frequency.

The wave peak frequency in this study ranges from 0.06 Hz to 0.33 Hz. For this reason, for a semi-submersible, the fatigue damage gradient of a scatter diagram only shows the gradual fatigue damage increase caused by the tower natural frequency. For a monopile, the fatigue damage of a scatter diagram will peak at its natural frequency, that lays within wave range.
Due to the floater's boundary condition that allows floater motions, the floater may experience motions due to wave excitation, that are not caused by resonance with an eigenfrequency. Higher wave excitation may occur at specific frequencies, due to:

- The dimensions of the floater lining up with the wave length (dependent on ϕ);
- The fact that an increase in ω may result in both a higher water particle acceleration a (increasing the fatigue damage, and dependent on H_s) and an increase in diffraction (decreasing the fatigue damage, and dependent on H_s and ϕ). If the frequency, where both effects are equally dominating, is excited by the wave spectrum, the wave excitation is likely to peak.

As the effect of the high tower natural frequency on the fatigue damage is less influential for the wave frequency range, the fatigue damage caused by peaks in wave excitation, might affect the fatigue damage gradient of a semi-submersible. Yet, it must be noted, that the fatigue damage peaks caused by wave excitation are generally much less pronounced than the peaks caused by natural frequencies, as shown in Figure 40.
Summarized, the fatigue damage gradient of a monopile is mainly affected by its structural natural frequency, which is equal for every scatter diagram. In contrast, two factors complicate the estimation of the fatigue damage gradient for a semi-submersible:

- The gradient is affected by a wide range of wave frequencies;
- The wave frequencies that affect the gradient differ per scatter diagram, mainly due to the floater's non-axisymmetric shape.

Two of the four lumping methods seem to be equipped to handle these complicating factors:

- The frequency domain load calculation of the Katsikogiannis method is able to identify the frequencies relevant to the fatigue damage, for each scatter diagram. Katsikogiannis' limitation might be the fact that coupling effects (likely to be more prominent for semi-submersible's than for monopiles, due to their higher motions) are only partially represented.
- The Jia method neglects peaks in fatigue damage at specific wave frequencies (regardless of whether they are caused by natural frequencies or by wave excitation). Yet, the different blocks for which the Jia method is computed may suffice to capture the gradual fatigue damage increase, caused by the high tower natural frequency. As a monopile likely shows a more pronounced fatigue damage peak in its scatter diagrams, the Jia method may be more accurate for a semi-submersible. Furthermore, the fatigue damage increase caused by an increase in H_s (derived from Morison's equation) and ω (due to an increase in load cycles), is taken into account.

The Seidel method, that assumes a single frequency (that is constant for all scatter diagrams) dominates the fatigue damage, is likely to be accurate for a monopile, but very inaccurate for a semi-submersible. The Song & Wang method can potentially show a high accuracy, if the $D(H_s)$ and $D(T_p)$ relations can be correctly identified through empirical research.

Part III

Comparing lumping method performance

Section 1 addressed that the performance of a lumping method is defined by both its reduction of computational time and its accuracy. The accuracy is defined as the error between the scatter diagram fatigue damage, computed using the lumped sea states and computed using the original sea states of the scatter diagram, as shown in Equation 5. Section 4 and Section 5 identified what hydrodynamic factors influence the fatigue damage gradient and which lumping methods take these factors into account. These lumping methods were predicted to have a higher accuracy.
In this part, the accuracy and the reduction of computational time of the four lumping methods will be computed, compared, and explained, using the findings from Part II. By doing so, the second research question will be answered:

2. What is the performance of the four lumping methods when applied to a semi-submersible?

6 Results on lumping method performance

In order to compare the performance of the lumping methods, first context will be provided, regarding the computational time needed for a full hindcast fatigue damage analysis. Section 6.1 will show that this computation would take about ten weeks, using the resources that were available for this thesis.
Then, Section 6.2 will compare the performance of the different lumping methods, when applied to a scatter diagram where v = 6 m/s, v = 14 m/s and v = 22 m/s (μ = 0° and ϕ = 0° for all of them). Section 1 noted that the initial aim of this study was to perform a sensitivity test on wind-wave misalignment μ and floater orientation ϕ as well. Due to the incorrect implementation of wind directions higher than 0° in SIMA, the results from these tests were considered invalid. In addition, the results implied that the use of three wind seeds may not have been enough to draw valid conclusions on these sensitivity tests. These two matters will be discussed in Section 6.3. It must be noted that Part II has already provided a theoretical argumentation on how v, μ and ϕ affect the fatigue damage gradient and which lumping method is expected to be best equipped to represent these effects.

6.1 Computational time of fatigue damage analysis using the full hindcast

Using SIMA on a 40-core server (with 80 logical processors), 40 sea states could be computed simultaneously. Performing a single 4000 s computation lasts about 15 minutes and 40 seconds. Computing 40 4000 s simulations simultaneously lasts 40 minutes. When more simulations are added, they are computed in groups of 40 at a time.
From the hindcast used in this study, the sea states with a wind speed between 3 m/s and 25 m/s (operational range) were selected. Furthermore, 2 m/s wind speed bins, 30° wave direction bins, 30° wind direction bins, 1 s T_p bins and 1 m H_s bins were used, as stated in Section 1.5. This resulted in 10499 sea states, each with a unique wind speed, wind direction, wave direction, T_p and H_s.

Due to the floater's symmetry (every pontoon being an axis of symmetry), the wave direction range could be limited to 0°, 30° and 60°. Now, only 8138 sea states were left.
For the wave directions of 0° and 60°, the floater was symmetric with regard to the waves (the wave direction being the axis of symmetry). Because of this, only the wind-wave misalignments of 0° up to and including 180° were taken into account for these wave directions. This reduced the number of sea states to 6817.
This shows that just by the use of symmetry, one third of the sea states could be eliminated, without reducing the accuracy of the computed total fatigue damage in any way. Yet, this reduction will be a lot higher for an axisymmetric foundation, like a monopile.
Considering the fact that three wind seeds are used, this yields 20451 time domain load simulations.
Using the resources that were available in during this thesis, 10 weeks is considered an optimistic estimation of the time needed to compute, post-process and save the 20451 time domain load simulations. In Appendix G, the calculation that leads to the estimation of 10 weeks can be reviewed. It must be noted, that these 10 weeks exclude the time needed to create and check the SIMA model, to pre-process the hindcast and to identify the appropriate SIMA time step settings.

6.2 Performance comparison

Figure 43 shows the fatigue damage error and the computational time, of the lumping methods that were tested.
The fatigue damage error was computed for the three scatter diagrams (where v = 6 m/s, v = 14 m/s and v = 22 m/s), using Equation 5. In Figure 43, the average (**not** weighed by the NOC of each scatter diagram) of these errors is shown, and the computational time is given as a percentage, according to Equation 51. Here, T_{lumped} represents the computational time needed to compute all lumped sea states of the entire hindcast, as yielded by the given lumping method. T_{full} is the computational time needed to compute the full hindcast (3 wind seeds · 6817 sea states, as shown in Section 6.1).

$$T_{\%} = \frac{T_{\text{lumped}}}{T_{\text{full}}} \cdot 100\% \tag{51}$$

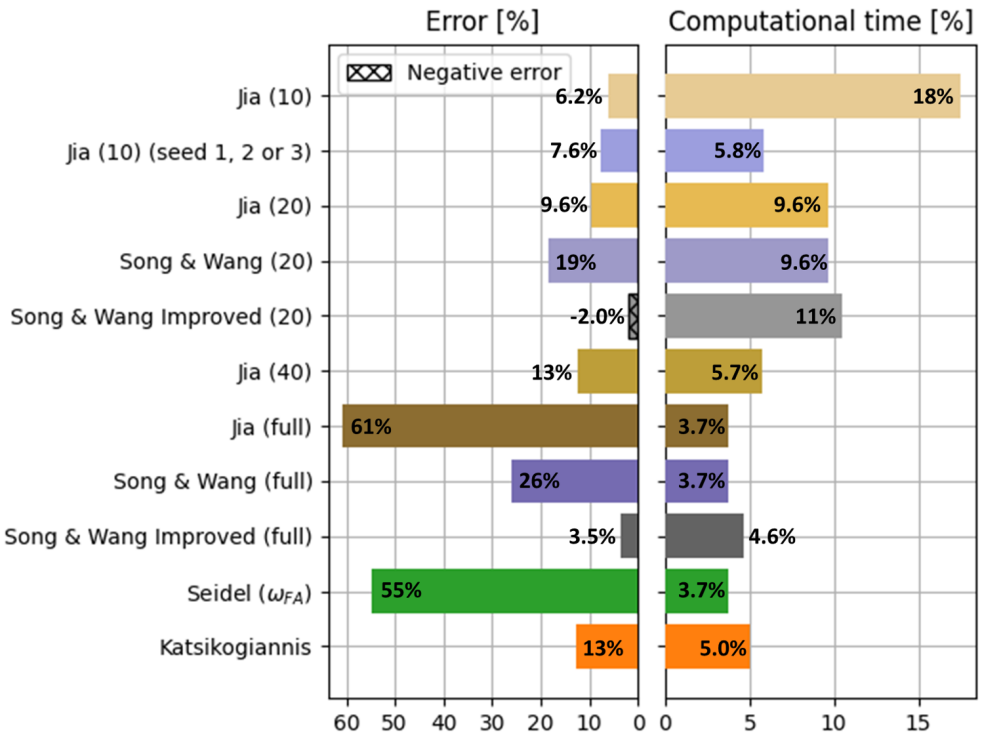

Figure 43: The average error across the scatter diagram fatigue damage computed using the lumped sea states and the original sea states (Equation 5) and the computational time compared to the full hindcast computational time (Equation 51) plotted for various lumping methods

The labels (10), (20) and (40) behind the names of the block partitioning lumping methods, represent the maximum block size that was used. The block partitionings corresponding to these block sizes can be reviewed in Section 5.1, and in Figure 44, Figure 45 and Figure 46. The label (full) refers to the fact that the full scatter diagram was considered to be a single block. In Section 6.2.1, the results of Jia (10), Jia (20) and Jia (40) are discussed in the context of a block size sensitivity study.
Regarding the remaining results, lumping methods that scored reasonably well (with an error below 30%) are discussed in Section 6.2.2, and methods with higher errors are discussed in Section 6.2.3.
In these sections, the following comparisons are performed:

- Using the results of Jia (20) and Song & Wang (20), as well as Jia (full) and Song & Wang (full), the Jia and Song & Wang methods are compared;
- The methods Jia (10) (seed 1, 2 or 3), Song & Wang Improved (20) and Song & Wang Improved (full) are variations of the original lumping methods, testing whether slight alterations could increase their performance;
- The Seidel and the Katsikogiannis method are discussed and the four main lumping methods are compared.

6.2.1 Sensitivity to block size

For small block sizes, each lumped sea state represents fewer original sea states, compared to larger block sizes. Because of this, for small block sizes, the fatigue damage resulting from the lumped sea state is likely to be quite accurate, regardless of the lumping method. A downside to a small block size, is the fact that a higher number of lumped sea states will need to be computed using time domain load simulations, which increases the computational time. The aim of this block size sensitivity study is to get an understanding of the proportion between the decrease in block size, the consequential increase in accuracy and the consequential increase in computational time.
This study is performed using the Jia method and the block partitioning is performed using the algorithm as explained in Section 5.1. The block sizes are characterized by their maximum number of sea states per block, namely 10, 20 and 40. Respectively, Figure 44, Figure 45 and Figure 46 show the lumped sea states according to the Jia method for these three block sizes. The block partitioning for the v = 6 m/s and v = 22 m/s scatter diagrams, can be reviewed in Appendix N.

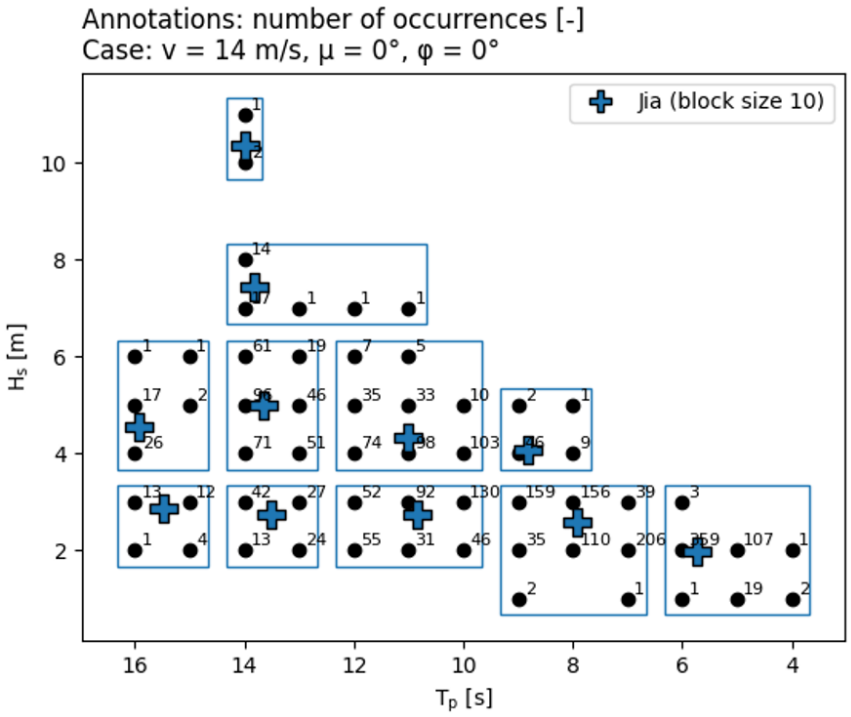

Figure 44: Jia lumped sea state using a block size 10

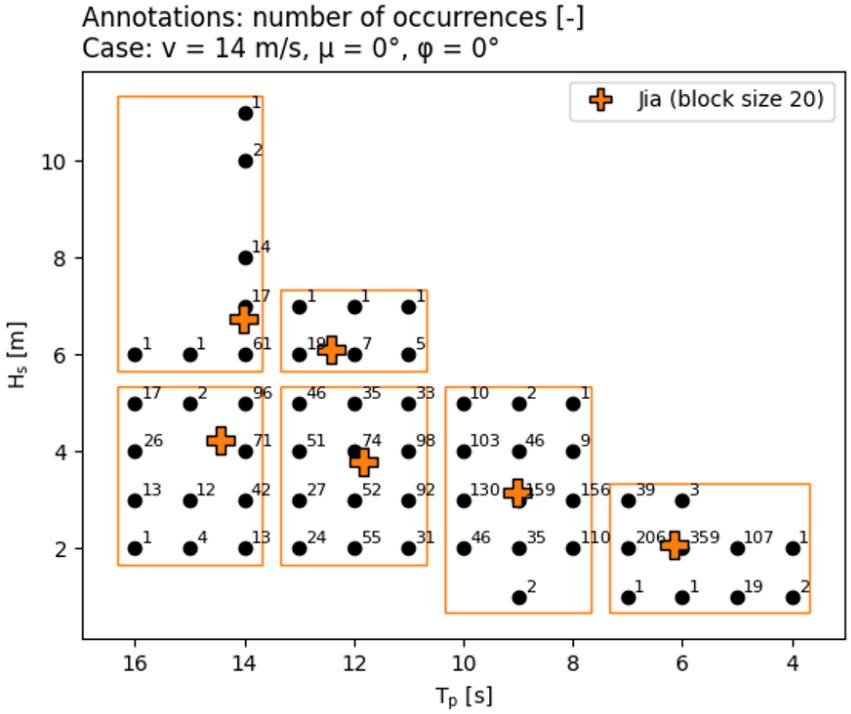

Figure 45: Jia lumped sea state using a block size 20

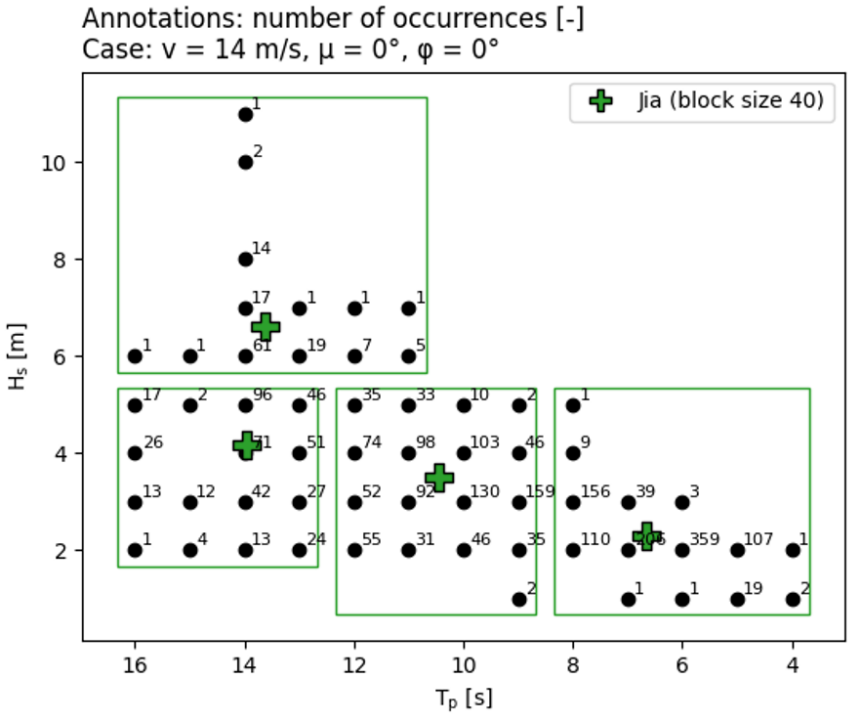

Figure 46: Jia lumped sea state using a block size 40

The reduction of computational time is computed by substituting Equation 53 into Equation 52. Equation 53 computes how many lumped sea states scatter diagram i will have, where k is the total number of scatter diagrams in the hindcast (taking operational wind speeds and symmetry into account) and where $N_{\text{Block size}}$ is the average number of sea

states per block. The floor function is used, as the block partitioning algorithm tends to add leftover sea states to existing blocks, rather than creating a new smaller block. Assuming the scatter diagram contains at least one sea state, the number of lumped sea states of a scatter diagram will always be equal or higher to one. Equation 52 takes the sum of the number of lumped sea states of every block $N_{\text{SD, i}}$ and computes what percentage this is of the total number of sea states in the hindcast N_{Total} (again, taking operational wind speeds and symmetry into account). Note that the used block sizes 10, 20 and 40 represent the maximum block size, given as an input to the block partitioning algorithm. The average block size $N_{\text{Block size}}$ for each of these settings is much lower, as shown by Table 10.

$$T_{\text{Song \& Wang, block}} = T_{\text{Jia, block}} = \frac{\sum_{i=1}^{k} N_{\text{SD, i}}}{N_{\text{Total}}} \cdot 100\% \tag{52}$$

$$N_{\text{SD,i}} = \begin{cases} \lfloor \frac{N_{\text{SD, i}}}{N_{\text{Block size}}} \rfloor, & \text{for } \lfloor \frac{N_{\text{SD, i}}}{N_{\text{Block size}}} \rfloor \geq 1 \\ 1, & \text{for } \lfloor \frac{N_{\text{SD, i}}}{N_{\text{Block size}}} \rfloor = 0 \end{cases} \tag{53}$$

Block size:	Average number of sea states per block $N_{\text{Block size}}$:
10	5.283
20	9.100
40	15.11
full	44.67

Table 10: Average number of sea states per block corresponding to the each block size label (representing the value of the maximum block size input parameter in the block partitioning function)

As the results of Jia (10), Jia (20), Jia (40) and Jia (full) in Figure 43 show, the computational time rapidly decreases as the block size increases, while the average error increases, as was predicted. For the cases tested, the Jia (40) result seems most optimal. Figure 47 shows the fatigue damage error of each scatter diagram.

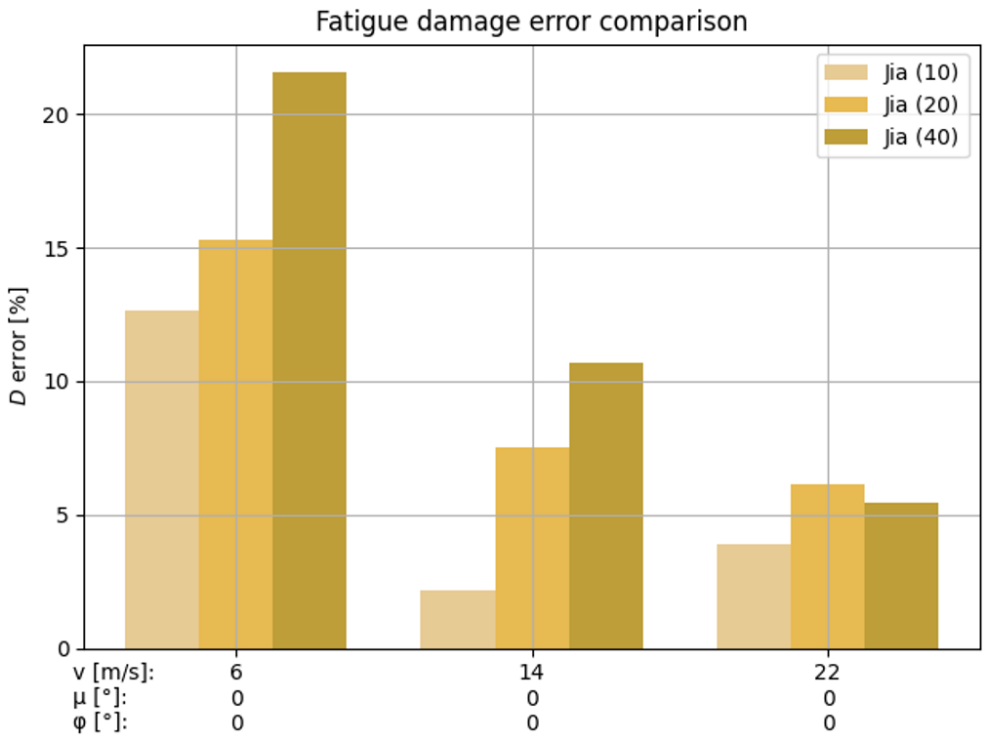

Figure 47: Accuracy of the Jia method applied to different block sizes, plotted for the three scatter diagrams

Surprisingly, for the $v = 22$ m/s scatter diagram, Jia (20) showed a higher error than Jia (40) scatter. As will be shown in Figure 50, the fatigue damage error can differ greatly among different wind and wave seeds. As there is no mathematical or physical explanation for the Jia (40) error being smaller than the Jia (20) error, this result is likely caused by too few winds seeds being used, during the fatigue damage calculation.

6.2.2 Lumping methods with a <30% error

Section 6.2.2 shows the scatter diagram fatigue damage errors computed using the lumping methods that showed a reasonably low error (<30%).

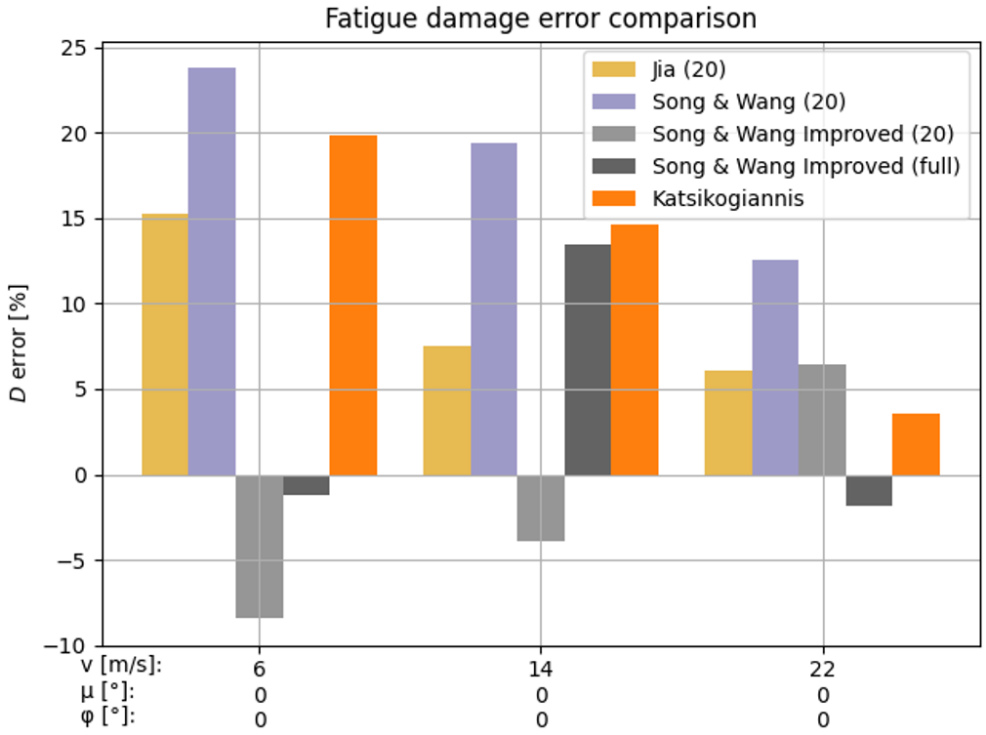

Figure 48: Accuracy of the lumping methods with a low error (<30%), plotted for the three scatter diagrams

Comparison of Jia (20) and Song & Wang (20)

A comparison was done between the Jia and Song & Wang methods, using a block partitioning of block size 20 for both. The computational time of the Song & Wang method is equal to the computational time of the Jia method, given by Equation 52. Yet, the Jia method consistently shows a lower error.

The error of the Song & Wang method is likely due to the fact that Song & Wang tends to underestimate T_p, mainly for high T_p's, as shown by Figure 49. It is unlikely that this error is due to an overestimation of H_s, as Song & Wang yielded almost the same H_s as Jia.

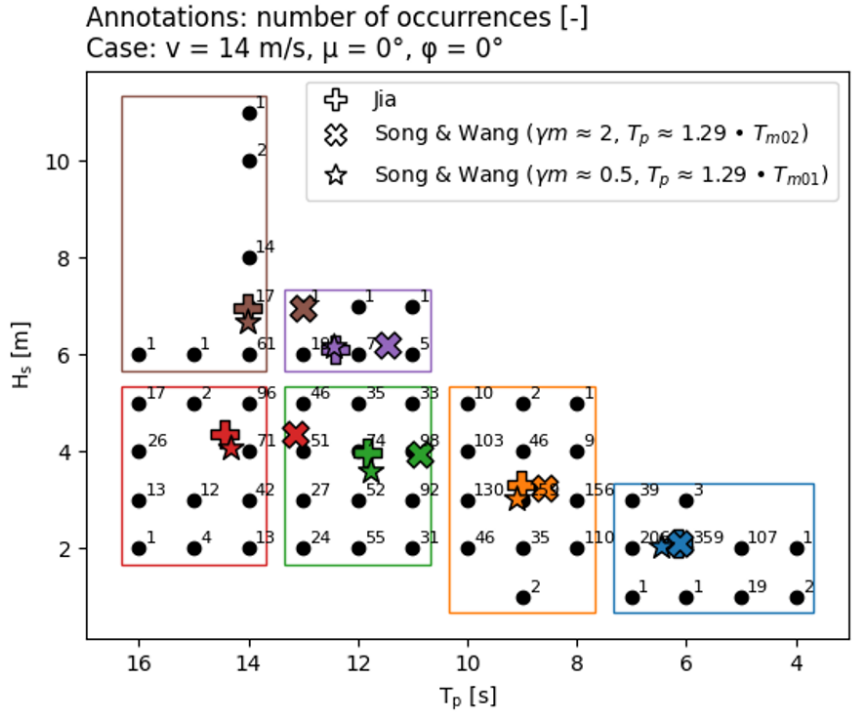

Figure 49: Lumped sea states selected by Jia (20), Song & Wang (20) ($\gamma m \approx 2$, $T_p \approx 1.29 T_{m02}$) and Song & Wang Improved (20) ($\gamma m \approx 0.5$, $T_p \approx 1.29 T_{m01}$)

The next question is, why the Song & Wang method underestimates the lumped T_p. Figure 31.d shows that for high T_p's the fatigue damage D increases as T_p decreases, as is expected due to $a \propto \omega^2$ relation. Yet, when T_p is approached by $1.29 T_{m02}$ (T_{m02} is assumed by the original Song & Wang method, 1.29 is a factor recommended by literature [56] to convert T_{m02} to T_p), the T_p range at which this increase in D occurs, is underestimated. In other words, for high T_p's, D is underestimated, causing the lumping method to select a lumped T_p that is too high. Why the increase in fatigue damage due to the $a \propto \omega^2$ relation happens at a higher T_p range for this semi-submersible than for the floating structure in the Song & Wang paper, may be due to floater shape (which affects from which peak period, D starts to decrease due to diffraction (which increases as T_p decreases)).

Lastly, the reason why both methods yield a similar H_s will be discussed. To recall from Section 5, both the Jia and the Song & Wang method assume the relation between D and H_s to be in the shape of $D \propto H_s^x$. Jia theoretically derives the value for x by assuming an inertia dominated system, neglecting diffraction and the $a \propto \omega^2$ relation, based on the Morison's equation and the Palmgren-Miner rule, yielding $x = 5$. By doing so, the stress amplifications due to eigenfrequency resonance or peaks in the wave excitation transfer function, are neglected. Yet, as Section 4 has shown, the fatigue damage of the semi-submersible mainly shows a gradual decrease, caused by T_p approaching the high tower natural frequency. It has been discussed that the lumped sea states of the blocks might be sufficient to capture this decrease. Therefore, the hydrodynamic model assumed by the Jia method, might be a particularly suitable for a semi-submersible.

The Song & Wang paper empirically finds a value of $x = 4$. As Figure 49 shows, $x = 4$ and $x = 5$ result in almost the same H_s's. This is probably due to the fact that Jia assumes that the system is inertia dominated, and that the fatigue damage does not show peaks at specific frequencies. It is likely, that these assumptions are also valid for the floating

platform in the Song & Wang paper.

Testing variations of the original lumping methods
Section 5.1.2 showed that the wave energy period T_{m-10}, the mean period T_{m01} and the mean zero-upcrossing period T_{m02} can all be used in place of T_{estimate} in $D \propto F \cdot T_{\text{estimate}}$, as long as the correct value for F is found. To find x and F, the fatigue damages of a scatter diagram consisting of 59 sea states were computed using time domain load simulations. Then, the relations $D \propto 1.29T_{m01}$ and $D \propto H_s^1$ were derived. These relationships were valid for the v = 6 m/s and v = 22 m/s scatter diagrams as well. The practice of computing a 59 sea state scatter diagram ($N_{\text{Find } x \text{ and } F}$ = 59) (using 3 wind seeds) to find F and x results in a slightly higher computational time, given by Equation 54 and shown in Figure 43.

$$T_{\text{Song \& Wang, Improved, block}} = \frac{N_{\text{Find } x \text{ and } F} + \sum_{i=1}^{k} N_{\text{SD, i}}}{N_{\text{Total}}} \cdot 100\% \tag{54}$$

Figure 48 and Figure 43 show that this method (named Song & Wang Improved (20)) results in a smaller error than both the Jia and Song & Wang method, but also tended to underestimate the fatigue damage. This is a disadvantage, as wind turbine developers prefer a slightly conservative fatigue damage analysis, to reduce the risk of material failure. The negative error is likely due to the fact that (as shown in Figure 31.c) the γm = 0.5 line does not fit the actual H_s-D relation (blue line) that well. Perhaps a polynomial fit of a higher order would be more suitable. In addition, in Figure 31.d, the $1.29T_{m01}$ approximation experiences the decrease in D due to diffraction at T_p range slightly too high, also resulting in a slight underestimation of the fatigue damage at low T_p's. To conclude, the probability of a negative fatigue damage error can likely be decreased by choosing a more conservative fit for the $D(T_p)$ and $D(H_s)$ relations, as described above.
Next, the Song & Wang Improved method was applied using a block partitioning, where the entire scatter diagram was assumed to be a single block (named Song & Wang Improved (full)). As Figure 43 shows, this decreases the computational time significantly, while it results in the lowest, positive error measured in this study. Equation 55 shows how the computation time is computed. Here, N_{SD} equals the number of scatter diagrams in the entire hindcast (taking operational wind speeds and symmetry into account).

$$T_{\text{Song \& Wang, Improved, full}} = \frac{N_{\text{Find } x \text{ and } F} + N_{\text{SD}}}{N_{\text{Total}}} \cdot 100\% \tag{55}$$

Surprisingly, Figure 48 shows that the v = 14 m/s scatter diagram showed the highest fatigue damage error, despite the fact that this scatter diagram was used to derive the $D(H_s)$ and $D(T_p)$ relations. This suggests that the Song & Wang Improved method may have a high accuracy when applied to other scatter diagrams as well.
In addition, a variation of the Jia method was tested. During wind turbine development, up to six wind seeds are used to compute the fatigue damage [7] [37]. If the Jia method yields six (or a multiple of six) sea states per scatter diagram, the computational time could be reduced by computing the fatigue damage of each lumped sea state using a different wind seed, instead of using six wind seeds for every lumping sea state. This method will be called the *seed method*. To test how this practice might affect the computational time and the fatigue damage error, the scatter diagram fatigue damage was computed by alternating the three wind seeds for every lumped sea state (LSS) of the scatter diagram (for example, LSS of block 1 uses seed 1, LSS of block 2 uses seed 2, LSS of block 3 uses seed 3, LSS of block 4 uses seed 1, etc.). Naturally, this reduced the computational time by a factor of three (as shown in Figure 43 and by Equation 56, where N_{seeds} equals the number of wind seeds used),

while the fatigue damage error only showed a slight increase.

$$T_{\text{Jia (seed 1, 2 or 3)}} = \frac{\sum_{i=1}^{k} N_{\text{SD, i}}}{T_{\text{Total}} \cdot N_{\text{seeds}}} \tag{56}$$

Figure 50 shows the difference in fatigue damage errors, when the fatigue damage is estimated by the Jia method, applying different wind seeds.

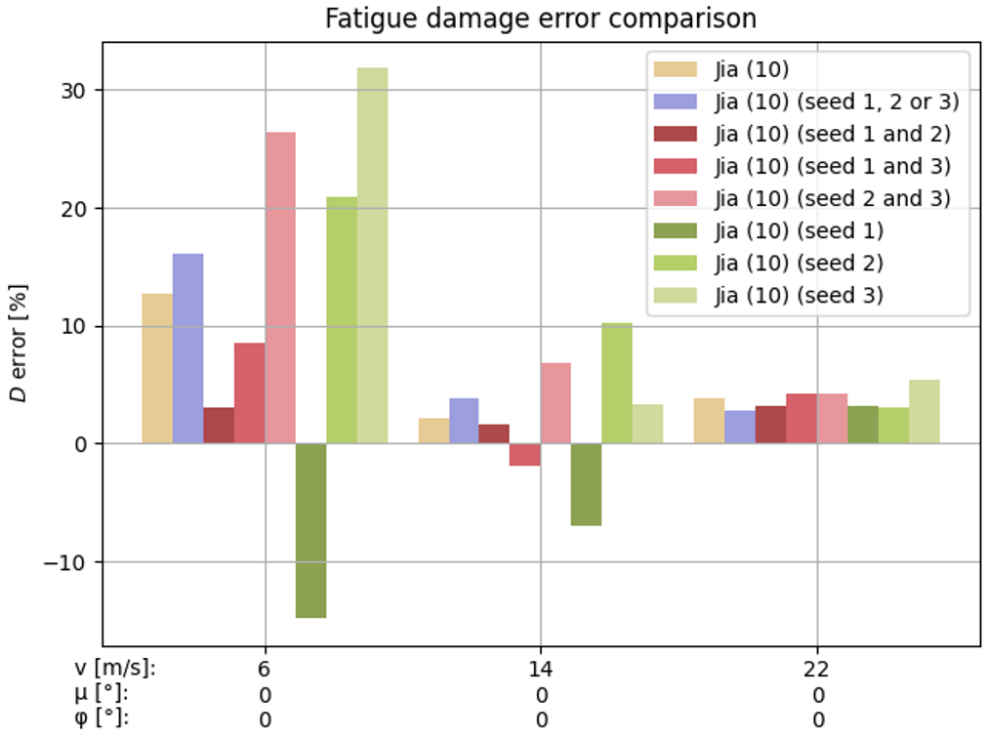

Figure 50: Fatigue damage errors resulting from the Jia method, using different wind seeds (the original Jia (10) method uses seed 1, 2 and 3)

Figure 50 shows the large difference in errors that occur for different wind seeds. This has also been hypothesized in Section 6.2.1 and will be discussed in more detail in Section 6.3.

The Katsikogiannis method
Lastly, the Katsikogiannis method showed a low fatigue damage error as well. As the Katsikogiannis paper suggests [16], the Katsikogiannis method can be used to find a single lumped sea state for multiple locations on the structure. This is done by finding the point of intersection of the contour lines of these different locations. This could not be studied in this thesis, as only the fatigue damage at the tower base had been computed. Yet, this practice assumes that the Katsikogiannis method has a high accuracy for every sea state on the contour line. Nevertheless, as Figure 51 shows, the Katsikogiannis contour line may differ in accuracy for different values of T_p.

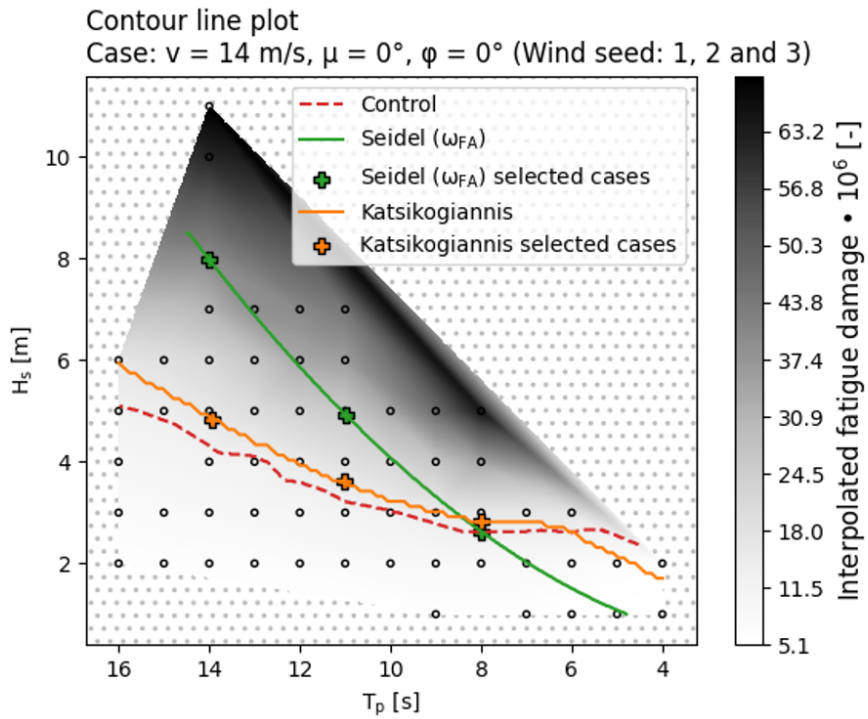

Figure 51: Seidel and Katsikogiannis lumped sea states selected to be computed in time domain

In order to provide a fair comparison of the Katsikogiannis and Seidel method with the other lumping methods, three peak periods were selected (T_p = 8 s, T_p = 10 s and T_p = 14 s). The fatigue damage of the lumped sea states at these peak periods was computed, using three wind seeds per sea state. Then, the fatigue damage error was computed for each sea state, and the mean error was calculated. This error is shown in Figure 48 per scatter diagram. This figure shows that the Katsikogiannis error was positive for every tested scatter diagram. This is due to the fact that the Katsikogiannis contour line tends to suggest a higher H_s than the control line, as shown in Figure 51, which results in an overestimation of the scatter diagram fatigue damage. The overestimation of H_s is caused by the error in the shape of the Katsikogiannis contour line gradient. The shape of the contour line is determined by any factor influencing the fatigue damage. Therefore, the error is not simply caused by an offset in the estimated fatigue damage, and it can be complicated to derive which parameter(s) is/are causing this error in the gradient. This is illustrated by Figure 34.
To ensure a conservative fatigue damage estimation, the location of the Katsikogiannis contour line must be checked before applying this method, as it cannot be guaranteed that the fatigue damage is overestimated for other structures. This is done, by creating a T_p-H_s graph with an inverted T_p axis (as shown in Figure 51), and checking if the contour line is located above the control line for every T_p. Naturally, this practice would require addition time domain load simulations.
The Katsikogiannis method gave a short computational time, given by Equation 57.

$$T_{\text{Katsikogiannis}} = \frac{N_{N_{SD}>1} + N_{\text{SD}} \cdot N_{\text{seeds}}}{N_{\text{Total}} \cdot N_{\text{seeds}}} \cdot 100\% \tag{57}$$

Here, $N_{N_{SD}>1}$ equals the number of scatter diagrams with more than one sea state. The latter term represents the white noise time domain calculation that needs to be performed for every scatter diagram with more than one sea state, in order to find the Katsikogiannis

contour line. This leads to a computational time of 4.98%, as shown in Figure 43. If it is decided to only apply the Katsikogiannis method on scatter diagrams with more than ten sea states, the computational time reduced to 4.79%. In this case, the lumped sea state of smaller scatter diagrams could be found using a less time-consuming lumping method, like the Jia method. This practice is unlikely to significantly increase the average scatter diagram fatigue damage error, as small scatter diagrams often have much lower probability of occurrence than larger scatter diagrams. In addition, the Jia (20) method had an average block size of 9.1 sea states and showed a fatigue damage error even slightly lower than Katsikogiannis (see Figure 43). Therefore, it may be assumed the Jia method is capable of lumping small scatter diagrams.
Lastly, the relation between v and Katsikogiannis' accuracy will be discussed. The Katsikogiannis method assumes a partially decoupled system, where the coupling effects are estimated. Figure 48 shows that the accuracy of the Katsikogiannis method increases as v increases. This corresponds to the findings in the study [48] discussed in Section 4.1, where a decoupled system resulted in a more accurate fatigue damage at higher wind speeds. This may be due to the fact that a lower wind to wave induced response ratio results in more coupling effects. A lower wind to wave induced response ratio is more likely to occur at lower wind speeds, when the load cycles caused by wind turbines are relatively small. In addition, lower wind speeds are more likely to occur in combination with higher peak periods, that approach the pitch natural frequency. As discussed, more resonance with the pitch natural frequency results in more coupling effects, and thereby, for these cases, the fatigue damage error increases, when a decoupled system is assumed.
Yet, it must be noted that the fact that the results from Figure 48 align with the results from the previous study [48], could be a coincidence. This will be further explained in Section 6.3.

6.2.3 Lumping methods with a >30% error

Section 6.2.3 shows the scatter diagram fatigue damage errors computed using the lumping methods that showed a high error (>30%).

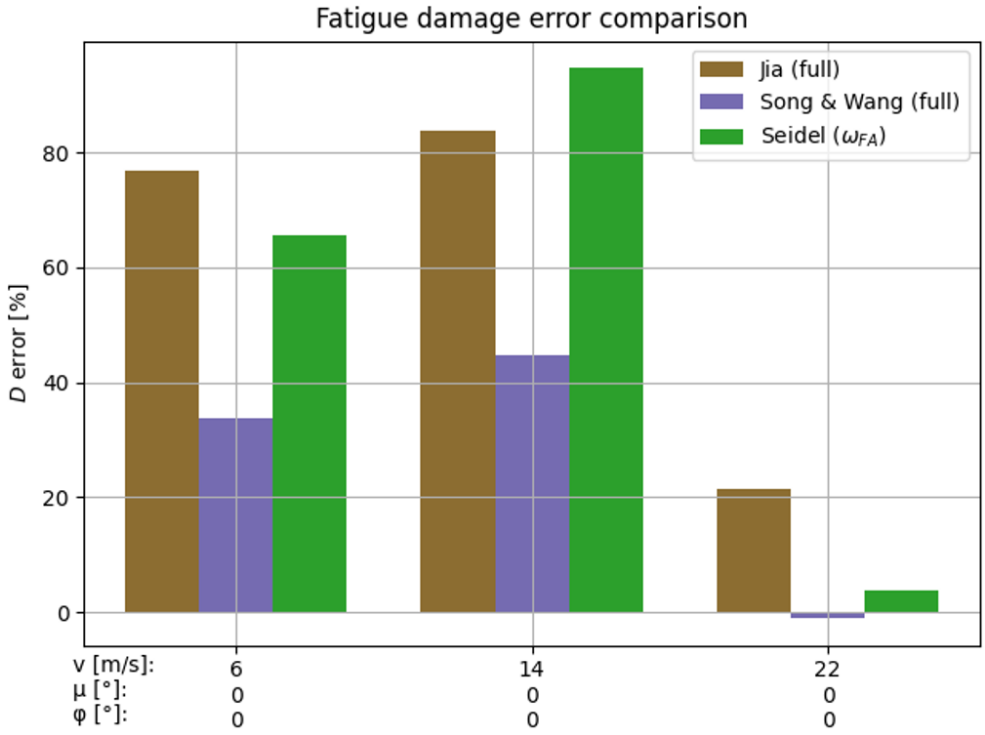

Figure 52: Accuracy of the lumping methods with a high error (>30%), plotted for the three scatter diagrams

Comparison of Jia (full) and Song & Wang (full)
As the Jia and Song & Wang methods are block partitioning methods, they were not expected to show a high accuracy when the entire scatter diagram was assumed to be a single block. Figure 52 confirms this hypothesis. This shows that, besides the physics on which the methods are based, they also rely on the mathematical principle that the fatigue damage of a small group of sea states may be represented by the average damage of every sea state in this group (weighed by the probability of occurrence), if this group is small enough. The computational time of Jia (full) and Song & Wang (full) is computed by Equation 58.

$$T_{\text{full}} = \frac{N_{\text{SD}}}{N_{\text{Total}}} \cdot 100\% \tag{58}$$

The Seidel method
Section 5.2.3 predicted that Seidel would show a low accuracy when applied to this semi-submersible as the axial stress PSD's showed, that there is not just one frequency that dominantly contributes to the fatigue damage gradient. In this study, the first fore-aft tower natural frequency was used as ω_{Seidel}. As expected, the results show that the accuracy of the method is low. Yet, the Seidel method had the lowest computational time (shared with Jia (full) and Song & Wang (full), computed by Equation 58). For structures that are suitable for applying the Seidel method (as explained in Section 5.2.3), this method can be very effective in reducing computational time.

6.3 The v, μ and ϕ sensitivity tests

A significantly limiting factor in this study were the available resources (available time, computational power, storage space). Ideally, the lumping methods would have been tested

for every scatter diagram in the hindcast using a time domain load calculation. Yet, due to the excessive computational time and storage space that this computation requires, this was not possible. For this reason, first, the use of a (much faster) frequency domain load computation had been considered as the main method to compute the internal loads. Nevertheless, after further studying the frequency domain, this method was invalidated for the purpose of this study (see Section 2.1). Now that the decision was made that the use of a time domain load computation would be the only valid way to perform this experiment, two compromises were made to reduce computational time and storage space:

- The intention was to perform a sensitivity test, where several scatter diagrams with different values of wind speed v, wind-wave misalignment μ and floater orientation ϕ (approximately covering the ranges in the hindcast), would have been studied. The aim was to make a prediction on the accuracy of the lumping methods, when applied to the entire hindcast, based on measured data, instead of only a theoretical argumentation;
- A lower number of wind seeds would be used, than common in the industry (six wind seeds [7] [37]). A small study (see Section 2.3.2) showed that three wind seeds would give a reasonable accuracy. Yet, it was known that in order to properly examine the effect of the number of wind seeds, a study testing more, different wind seeds (for example, several cases where one wind seed is used, compared to several cases where two wind seeds are used, etc.) would be required. Nevertheless, such a study would require a lot of computational time and storage space. Due to the limited resources, it was decided to use three wind seeds, as the small study had suggested.

Subsequently, all three sensitivity studies were performed using three wind seeds. Yet, the μ and ϕ studies were regarded as invalid, for the following reason.
Wind directions higher than 0° were incorrectly implemented in SIMA. It was assumed that the rotor would align with the wave direction automatically. Instead, it stayed at the 0° wind direction, unless it was rotated by manually changing the model's input variables. This may result in high yaw angles and a significantly lower or an absent thrust, affecting the dynamics of the entire system. As both the μ and ϕ sensitivity study involved a change of wind direction, both studies had to be regarded as invalid.
After further examination of the results, the conclusion was drawn that stochastic variance was present in the results, due to the lowered number of wind seeds. This conclusion was drawn, based on the following results:

- Section 6.2.1 has shown that in some cases the Jia method shows a higher accuracy for a larger block size. This observation could not be physically explained. Therefore, it is assumed that this result is caused by stochastic variance due to the use of only three wave seeds.
- Figure 50 shows that the fatigue damage error can differ greatly when using different wave seeds or when using different combinations of two wave seeds. Because of this, it is unlikely that three wave seeds is sufficient to eliminate stochastic variance entirely.

As a consequence of the present stochastic variance, the fatigue damage errors given in this thesis may be several percentages off. It is difficult to estimate the average size of the error caused by stochastic variance. To investigate this, one should perform a study where the fatigue damage is computed using numerous sets of three different wind seeds each. This study has not been performed, due to the limited resources. Based on the differences in fatigue damage errors for two wind seeds, shown in Figure 50, it is estimated that this

error (i.e., the error of the fatigue damage error) will not exceed 20% and is more likely to within 3% and 10%. As the findings based on v, μ and ϕ sensitivity tests would likely show up as smaller differences in fatigue damage errors, these tests were assumed to be more vulnerable to the errors caused by stochastic variance, than the comparison of different lumping methods. Nevertheless, the Katsikogiannis results plotted over v showed a trend that could be explained using similar results from a previous study (see Section 6.2.2). Yet, this result could also be a coincidence. It must be noted that Part II provided a theoretical argumentation for the relation between v, μ and ϕ, and the fatigue damage gradient.
Regarding the fact that this study assumes a lumping method to be accurate when its fatigue damage error is lower than 30%, the conclusions drawn from the lumping method comparison in this chapter are generally not much affected by a 3% to 10% stochastic variance error (i.e., error of the fatigue damage error). The cut-off point of 30% was chosen based on the literature study (see Section 1.5.1), that showed that the accuracy of a single lumping method could vary significantly between different studies (due to different hindcasts and structures). This shows that the exact fatigue damage error of a lumping method does not hold as much meaning as the global trend of its accuracy across different studies. In addition, the conclusions from this chapter correspond to the predictions made in Part II based on theory. For these reasons, the lumping method comparison performed by this thesis is regarded as valid.

7 Conclusion

This study aims to answer the question, which lumping method shows the highest performance (involving both accuracy and reduction of computational time), when applied to a non-axisymmetric floating turbine. This question has been divided into three subquestions. The conclusions regarding these three subquestions will be listed in this section.

- Section 7.1 lists the conclusions regarding subquestion 1a, by giving an overview of the factors influencing the fatigue damage gradient.
- Section 7.2 discusses subquestion 1b and 2, by listing the conclusion regarding accuracy and reduction of computational time for the four studied lumping methods.
- Section 7.3 answers the main research question of this thesis by giving a final recommendation for a lumping method.

The time domain load calculation results with a wind direction higher than 0° have been invalidated due to an incorrect setting in the model. Thereby, the sensitivity studies on μ and ϕ were regarded as invalid. The sensitivity study performed on wind speed v is likely to be less accurate, due to a low number of wind seeds used. The low number of wind seeds is not expected to invalidate the lumping method comparison performed by this study, due to the large difference in fatigue damage errors between the accurate and inaccurate lumping methods, as well as the fact that the experiment's results align with the hypotheses, that were constructed based on theory.
All conclusions in these sections are valid assuming:

- The semi-submersible studied in this thesis;
- The tower base as the location where the fatigue damage is computed;
- An operational turbine load case;
- The eight scatter diagrams studied in this thesis.

Yet, in the introduction several assumptions were mentioned, for which a lumping method should be valid, that are broader than the assumptions listed above. For this reason, Section 7.4 will discuss to what extent the conclusions from this study can be generalized to meet these assumptions. Lastly, Section 7.5 will provide suggestions for future research.

7.1 Conclusions on the fatigue damage gradient for a semi-submersible

The accuracy of a lumping method is determined by its capability to estimate the fatigue damage gradient. The fatigue damage gradient describes how the fatigue damage changes over the T_p and H_s axes of a scatter diagram. For the semi-submersible floating turbine used in this study, the fatigue damage gradient is affected most by the factors listed below. Preferably, these factors are taken into account by the lumping method's hydrodynamic model, as this will likely increase its accuracy.

- Resonance with the first fore-aft tower natural frequency, because:

  - It has been shown that the hydrodynamic load on the structure increases quadratically as the wave excitation frequency increases. In addition, a higher frequency increases the fatigue damage, as it increases the number of load cycles. For these two reasons, any resonance that may occur due to a slide overlap of the tower natural frequency and the wave spectrum, will result in a relatively high fatigue damage, compared to resonance occurring with the lower motion natural frequencies. As the first fore-aft tower natural frequency is higher than the wave range, the scatter diagram experiences a gradual increase in fatigue damage along the peak frequency axis.

- Excitation forces caused by peaks in the wave excitation PSD (the wave transfer functions multiplied by the wave spectrum), because:

  - It has been shown that the fatigue damage increases is T_p is equal to the wave period of high peaks in the wave excitation transfer function. As the natural frequencies of the structure are generally located outside the wave range and therefore do not result in fatigue damage peaks, fatigue damage peaks caused by wave excitation (which are generally a lot smaller than peaks caused by natural frequencies) may show up in the scatter diagram.

The fatigue damage gradient is less dependent on the following factors. For the semi-submersible floating turbine used in this study, these factor may be neglected by the lumping method.

- Wind turbulence and tower shadowing, because:

  - It has been shown that aerodynamic effects are constant for the entire scatter diagram, since a scatter diagram only includes sea states that all occur at the same wind speed and wave direction.

- Coupling effects between wind and waves, because:

  - Coupling effects mainly occur at the pitch natural frequency, when wind and waves are aligned. In this case, the aerodynamic damping decreases pitch resonance in a coupled system. As the pitch natural frequency is likely lower than the wave range, coupling effects are not expected to be significant. This has been confirmed by a previous study [48] and by a small study performed on the semi-submersible in this thesis.

- Resonance with the motion natural frequencies, because:

  - The motion natural frequencies are generally lower than the wave spectrum. Therefore, resonance with the wave is less likely to occur. In addition, it has been shown that the water particle accelerations of lower frequencies is lower and that low frequencies result is less load cycles. Both these factors decrease the fatigue damage.

The main differences between a monopile and a semi-submersible regarding the fatigue damage gradient, are the following:

- A monopile is more likely to have a first structural natural frequency within the wave frequency range, while the tower natural frequency of a semi-submersible is generally

higher. Because of this, for a monopile, the fatigue damage across a scatter diagram is likely to show a high peak at f_p equal to the monopile's structural natural frequency. Because of this, as well as the fact that a monopile is bottom-fixed, fatigue damage peaks due to wave excitation are unlikely to show up for any f_p.

- For a monopile, the wave excitation transfer functions are the same for every wave direction. For a semi-sumbersible, they differ, due to the floater's non-axisymmetric shape. For this reason and the fact that the fatigue damage gradient of a monopile is unlikely to be affected by peaks in the wave excitation PSD, the fatigue damage gradient of a semi-submersible is more likely to differ per wave direction than the gradient of a monopile.

7.2 Conclusions on lumping methods for a semi-submersible

The Seidel method shows a low performance when applied to the semi-submersible in this study, due to its extremely low accuracy. Its reduction of computational time is good. Its low accuracy is caused by the following:

- The Seidel method assumes that a single frequency dominates the shape of the fatigue damage gradient, while the fatigue damage gradient of the semi-submersible may be affected by multiple frequencies, that may change per floater orientation.

The Jia method may show a high performance for some block cases, but cannot be regarded as the best lumping method for the semi-submersible. This is due to the following advantages $(+)$ and disadvantages $(-)$:

$+$ The Jia method neglects fatigue damage peaks due to natural frequencies or peaks in the wave excitation PSD. Yet, the lumped sea states of the different blocks may capture the gradual increase of the fatigue damage for higher values of f_p, due to the tower natural frequency. The motion natural frequencies do not affect the fatigue damage gradient and the peaks in the wave excitation transfer function only have a minor effect. Therefore, Jia's simplifications of the hydrodynamic model are acceptable.

$-$ The Jia method requires a block size to be selected. It has been shown that the accuracy and the reduction of computational time highly depends on the chosen block size. Yet, conducting a study on the relation between an increase in block size, the decrease in accuracy and the decrease in computational time, is computationally intensive. A turbine developer will have to decide between trusting that the results from previous research on block size are valid for their structure, or performing a block size sensitivity study themselves (which will increase Jia's short computational time).

$+$ When the fatigue damage is computed using by dividing the lumped sea states over the wind seeds (in this thesis referred to as the *seed method*), Jia's computational time decreases significantly, while its accuracy remains relatively high. Yet, due to the limited number of scatter diagrams tested in this study and due to the lack of previous studies on this method, more research is necessary to ensure that this method's high accuracy is consistent.

The Katsikogiannis method performs well, when applied to the semi-submersible used in this study, due to the following reasons:

- Coupling effects by wind and waves are partially neglected by the Katsikogiannis method. Yet, it has been shown that this assumption is valid.
- The fatigue damage gradient of the semi-submersible is affected by multiple frequencies. Katsikogiannis' fatigue damage estimation, based on a frequency domain load calculation, is able to identify these frequencies.
- It has been shown that the frequencies significantly affecting the fatigue damage gradient, may differ per μ and ϕ, due to the floater's non-axisymmetric shape. The Katsikogiannis method is the only tested method that is capable of identifying the different frequencies per scatter diagram.

Song & Wang method as described in the paper did not perform well, as the empirically found relations $D(T_p)$ and $D(H_s)$ by the paper, were not valid for the semi-submersible in this study. Yet, when these relations were adjusted to the semi-submersible, the Song & Wang (Improved) method showed the highest accuracy in this study, while the computational time only slightly increased. Nevertheless, the Song & Wang Improved method is not considered as ready to be applied, for the following reasons:

- Further research must be performed on the accuracy of the $D(T_p)$ and $D(H_s)$ relations, when applied to different scatter diagrams, as this study has shown that the fatigue damage gradient is dependent on v, μ and ϕ.
- The Song & Wang Improved method showed a tendency to underestimate the fatigue damage, due to the fact that $D(T_p)$ and $D(H_s)$ were not chosen conservatively. Through research, a method must be designed to ensure $D(T_p)$ and $D(H_s)$ are conservative enough, to minimise the risk of fatigue damage underestimation.

7.3 Final recommendation for a lumping method suitable for the semi-submersible floating turbine

To conclude, this thesis does not recommend applying the Seidel method or the Song & Wang method on the semi-submersible studied in this thesis. The Song & Wang Improved method requires further research. While the Jia method may be accurate, no method has been described on how to find the correct block size, and performing a block size sensitivity study is time-consuming. The seed method might offer a solution to this problem, but requires further research as well.
The fatigue damage gradient of the semi-submersible floating turbine in this study is characterised by multiple frequencies that could be of influence. These frequencies may differ for diverse wind-wave misalignments and floater orientations. Because of its fatigue damage gradient estimation in frequency domain, the Katsikogiannis method is the only evaluated lumping method, that is capable of identifying these frequencies for each scatter diagram. For this reason, the use of the Katsikogiannis method is the final recommendation of this study.

7.4 Generalizing the conclusions

Several assumptions have been identified that ideally should be valid for a lumping method. As the conclusions in the sections above were drawn for more limiting assumptions, this

section will evaluate to what extent this thesis' conclusions can be generalized to meet the ideal assumptions.

7.4.1 Foundation design and small structural changes

The first assumption states that a lumping method is tailored for a specific floater type. The research question of this thesis focusses on a non-axisymmetric floating turbine specifically. In this study, only the Volturn semi-submersible has been tested, so no definitive conclusion may be drawn on the accuracy of this thesis' conclusions, when applied to another non-axisymmetric floating turbine. Therefore, only a prediction will be made, based on the following three structural difference that may occur between different floaters:

1. The motion natural frequencies of floating turbines are generally lower than the wave frequency range and it has been shown their first tower natural frequency tends to be on the higher end of or even exceed the wave spectrum. Because of this, the conclusion that the tower natural frequency results in a gradual fatigue damage increase for higher values of ω and the conclusion that peaks in the wave excitation PSD may affect the fatigue damage gradient, are likely valid for other non-axisymmetric floating turbines as well.
2. Whenever a structure has a non-axisymmetric shape, the wave excitation transfer functions will differ per wave direction. For this reason, differences in the fatigue damage gradient per scatter diagram are excepted for other non-axisymmetric floating wind turbines as well.
3. As the pitch natural frequency of this study's semi-submersible is lower than the wave range, coupling effects did not affect the fatigue damage gradient significantly. Models with higher pitch natural frequency located at a site with generally lower peak frequencies are more prone to coupling effects. For these models, the Katsikogiannis method may be less accurate.

The second assumption states that both a lumping method and a lumped sea state are still valid if a small structural change (like a change in column diameter) is applied. Regarding the arguments listed above, this assumption is likely valid for a lumping method. To what extent a change in dimensions changes the lumped sea state, has not been studied.

7.4.2 Location on structure

The third assumption states that a lumping method should be specific to a (range of) locations on the structure. This study has focussed on the fatigue damage at tower base. Yet, the fatigue damage gradient differs across the tower length, and is likely to be different in the mooring lines and for locations on the floater as well. Using the Katsikogiannis method, as recommended by this thesis, the contour line at multiple locations along the tower can be determined. A point of intersection of these contour lines marks the lumped sea state that is valid for at least all the tested locations. For this reason, the recommended method allows for at least two tower locations to be studied at once. The other lumping methods tested in this study, do not take the fatigue damage location into account. For this reason, their accuracy will likely change when applied to a different location. This has not been further studied.

7.4.3 Turbine's load case

The fourth assumption states that a lumping method should show a high accuracy, regardless of the turbine's load case. In this study, only the operational load case has been studied. Other load cases, like parked, fault conditions, emergency shut-downs and maintenance, have not been evaluated. Yet, the majority of the time that the turbine is not operational, the turbine will experience the parked load condition. The main differences of the parked load case, compared to the operational load case, are the following:

- No thrust force;
- No aerodynamic damping;
- A different mean displacement and mean rotation (the main difference is that an operational floating turbine has a larger mean pitch angle than a parked one, due to the presence of thrust);
- A different mooring stiffness (due to a different mean displacement and mean rotation);
- Slightly different eigenfrequencies (due to the lack of aerodynamic damping and a different mooring stiffness).

Due to the fact that the Katsikogiannis method is capable of identifying the system's eigenfrequencies and as it takes the (lack of) thrust force and aerodynamic damping into account, a high accuracy is expected when applied to a parked turbine. Moreover, as a parked turbine approaches a wave-only load case, almost no coupling effects between wind and waves occur and the accuracy of the Katsikogiannis method might even improve, compared to the operational load case. In addition, it has been shown that aerodynamic effects and coupling effects have close to no influence on the fatigue damage gradient for this semi-submersible turbine. For this reason, it is expected that the other tested lumping methods will show a similar accuracy for a parked load case, as for an operational load case.

7.4.4 Hindcast data set and scatter diagrams

The fifth assumption states that the lumping method should be able to lump any hindcast data set and any scatter diagram with a high accuracy. This thesis only studied a hindcast data set measured at the coast of Norway and tested just three scatter diagrams. For this reason, no definitive conclusion can be drawn on the validity of this assumption. Nevertheless, the ranges of wave heights and wave periods that can possibly occur, are limited by physics and are unlikely to become much higher than wave heights and wave periods from this hindcast. In addition, this thesis' turbine's operational wind speed range (from 3 m/s to 25 m/s with a rated wind speed of 10.59 m/s) is typical for wind turbines. For these reasons, it is expected that generally this thesis' conclusions are still valid when other hindcast data sets are used, if the following caveats are taken into account:

- For hindcasts with extremely low peak periods, resonance with the tower natural frequency may start to dominate the fatigue damage gradient. In this case, the Seidel method may show more accurate results.
- For hindcasts with extremely high peak periods, resonance with the pitch natural frequency may occur, increasing coupling effects. This might negatively affect the accuracy of the Katsikogiannis method.

- The reduction of computational time may vary for different hindcasts. For example, when the scatter diagrams are created, filtering on wind speed v only, the number of scatter diagrams will be smaller and the computational time of the non-block-partitioning methods will decrease, compared to the block partitioning one.

Lastly, it must be noted that a turbine developers might consider implementing a swell wave set and a wind wave set in their time domain model, rather than using the total sea wave set. The caveats listed above, also apply when a different wave set is being lumped.

7.4.5 Floater orientation

Due to the floater's non-axisymmetric shape, the wave excitation frequencies that dominate the fatigue damage gradient, differ per floater orientation. The sixth assumption states that a lumping method should be valid for every floater orientation. From the studied lumping methods, only the Katsikogiannis method is capable of identifying these frequencies for every scatter diagram.

7.5 Suggestions for further research

Suggestions on improving the Katsikogiannis method:

- The Jia method can be used to lump very small scatter diagrams (without applying block partitioning), for which performing the white noise computation is relatively costly in time.
- The fatigue damage load calculation could be performed by existing software. In this way, the white noise calculation does not have to be performed for every scatter diagram. This would mean that the Katsikogiannis method is just as fast as the Seidel method (the faster method tested: one time domain load simulation per scatter diagram). This improvement has already been tested on monopiles in previous research [9]. An example of such software designed for floating wind turbines, is the Python package RAFT [34]. Yet, the current version of RAFT makes assumptions that are unacceptable for fatigue damage calculations (see Appendix I). A research suggestion is to improve the RAFT model on these assumptions and to test if the program can be used as a substitute of the Katsikogiannis white noise calculation.
- For monopiles, it has been shown that the simulation length of the white noise load calculation can be reduced to ten minutes, without a notable loss of accuracy [9]. This practice reduces the computational time significantly. Yet, as the motion natural frequencies of floating turbines generally are low, further research must ensure that these low frequencies are captured, when such a short simulation time is used.
- It might be acceptable to assume that the white noise transfer function is constant as long as the wave direction is constant. This would save computational time, as much few white noise time domain load computations will need to be performed.

The seed method seemed to improve the performance of the Jia method significantly. More research is needed, to ensure that the high performance is consistent for various scatter diagrams.

In addition, further research on the Song & Wang method is highly recommended, for the following reasons:

- In this study, the $D(T_p)$ and $D(H_s)$ relations determined for the v = 14 m/s scatter diagram, were valid for the v = 6 m/s and v = 22 m/s scatter diagrams as well. This may suggest that only a small number of sea states need to be computed in time domain, in order to find one or multiple $D(T_p)$ and $D(H_s)$ relations that represent the entire hindcast. This may result in a higher computational time than the Katsikogiannis method.
- A high accuracy was found, even when the entire scatter diagram was assumed to be a single block. This implies that once $D(T_p)$ and $D(H_s)$ are known, this method can be used as a non-block-partitioning method, yielding a single lumped sea state per scatter diagram.

Further research on the improved Song & Wang method would include:

- Further testing if the $D(T_p)$ and $D(H_s)$ relations are valid for different values of v, μ and ϕ.
- Creating a method to minimise the risk that the fatigue damage is underestimated, by choosing $D(T_p)$ and $D(H_s)$ to be slightly conservative.

This study did not investigate the effects of combining different values for v, μ and ϕ. An example of such an effect could be the following. When μ = 90°, almost no aerodynamic damping of the waves occurs. This may amplify the differences in fatigue damage gradients for scatter diagrams with a different ϕ, caused by the differences in their wave excitation transfer functions. Further research needs to be done on this topic.
Lastly, the conclusions drawn by this study could be tested for different non-axisymmetric structure, for different locations on the structure, for different turbine's load cases, for different hindcasts and scatter diagrams, and for different floater orientations, in order to prove the hypotheses made in Section 7.4.

Bibliography

[1] Henrik Bredmose. 'Lecture 1 of Part 1 of course 46211 Offshore Wind Energy at DTU'. In: (2021).

[2] IRENA. *World Energy Transitions Outlook 2022: 1.5°C Pathway*. International Renewable Energy Agency, Abu Dhabi, 2022.

[3] Antonio Pegalajar-Jurado. 'Lecture 1 of Part 5 of course 46211 Offshore Wind Energy at DTU, source of figure cited as 'Equinor''. In: (2021).

[4] Zhen Gao and Erin Bachynski-Polić. 'Lecture slides of 'Installation of bottom-fixed and floating wind turbines' of TMR03 course at NTNU'. In: (2022).

[5] Erin Bachynski-Polić and Zhen Gao. 'Lecture slides of 'Introduction to offshore wind power and technology' of TMR03 course at NTNU'. In: (2022).

[6] Amir M. Kaynia et al. 'Seismic response of floating wind turbines due to seaquakes'. In: *Wind Energy* 26.2 (2023), pp. 145–162. DOI: https://doi.org/10.1002/we.2791. eprint: https://onlinelibrary.wiley.com/doi/pdf/10.1002/we.2791. URL: https://onlinelibrary.wiley.com/doi/abs/10.1002/we.2791.

[7] Jasper van den Broek-de Bruijn. *During oral discussion*.

[8] Lizet Ramírez et al. *Offshore Wind in Europe Key trends and statistics 2021*. Wind Europe, 2021.

[9] George Katsikogiannis, John Marius Hegseth and Erin E. Bachynski-Polić. 'Application of a lumping method for fatigue design of monopile-based wind turbines using fully coupled and simplified models'. In: *Applied Ocean Research* 120 (Mar. 2022). ISSN: 01411187. DOI: 10.1016/j.apor.2021.102998.

[10] Espen Engebretsen, Herbjørn Haslum and Olav Aagaard. 'Distributed potential theory and its application for spar-type floating offshore wind turbines'. In: *Proceedings of the International Conference on Offshore Mechanics and Arctic Engineering - OMAE* 1 (2020). DOI: 10.1115/OMAE2020-18284.

[11] George Katsikogiannis. *During oral discussion*.

[12] Zhen Gao and Erin Bachynski-Polić. 'Lecture slides of 'Statistical, spectral and fatigue analysis based on stress time series' of TMR03 course at NTNU'. In: (2022).

[13] Michiel van der Meulen. *Presentation at Siemens Gamesa Renewable Energy*.

[14] Zhen Gao. *During oral discussion*.

[15] *European Wind Energy Association (EWEA) webpage*. URL: https://www.ewea.org/wind-energy-basics/faq/#:~:text=A%20modern%20wind%20turbine%20produces,known%20as%20its%20capacity%20factor..

[16] George Katsikogiannis et al. 'Environmental lumping for efficient fatigue assessment of large-diameter monopile wind turbines'. In: *Marine Structures* 77 (May 2021). ISSN: 09518339. DOI: 10.1016/j.marstruc.2021.102939.

[17] Hui Min Hou, Guo Hai Dong and Tiao Jian Xu. 'An improved lumping block equivalent method for predicting fatigue damage of mooring system for fish cage'. In: *Ocean Engineering* 193 (Dec. 2019). ISSN: 00298018. DOI: 10.1016/j.oceaneng.2019.106567.

[18] Junbo Jia. 'An efficient nonlinear dynamic approach for calculating wave induced fatigue damage of offshore structures and its industrial applications for lifetime extension'. In: *Applied Ocean Research* 30 (3 July 2008), pp. 189–198. ISSN: 01411187. DOI: 10.1016/j.apor.2008.09.003.

[19] John M. Sheehan et al. 'Characterizing the wave environment in the fatigue analysis of flexible risers'. In: *Journal of Offshore Mechanics and Arctic Engineering* 128 (2 May 2006), pp. 108–118. ISSN: 08927219. DOI: 10.1115/1.2185129.

[20] Xiancang Song and Shuqing Wang. 'A novel spectral moments equivalence based lumping block method for efficient estimation of offshore structural fatigue damage'. In: *International Journal of Fatigue* 118 (Jan. 2019), pp. 162–175. ISSN: 01421123. DOI: 10.1016/j.ijfatigue.2018.09.016.

[21] Martin Kühn. 'Dynamics and design optimisation of offshore wind energy conversion systems'. Technische Universiteit Delft, 2001. URL: https://www.researchgate.net/publication/34768668.

[22] Xiancang Song et al. 'An innovative block partition and equivalence method of the wave scatter diagram for offshore structural fatigue assessment'. In: *Applied Ocean Research* 60 (Oct. 2016), pp. 12–28. ISSN: 01411187. DOI: 10.1016/j.apor.2016.08.005.

[23] Ying Min Low and Sai Hung Cheung. 'On the long-term fatigue assessment of mooring and riser systems'. In: *Ocean Engineering* 53 (Oct. 2012), pp. 60–71. ISSN: 00298018. DOI: 10.1016/j.oceaneng.2012.06.017.

[24] Patrik Passon. 'Damage equivalent wind-wave correlations on basis of damage contour lines for the fatigue design of offshore wind turbines'. In: *Renewable Energy* 81 (Sept. 2015), pp. 723–736. ISSN: 18790682. DOI: 10.1016/j.renene.2015.03.070.

[25] Marc Seidel. 'Wave induced fatigue loads: Insights from frequency domain calculations'. In: *Stahlbau* 83 (8 2014), pp. 535–541. ISSN: 14371049. DOI: 10.1002/stab.201410184.

[26] Patrik Passon and Kim Branner. 'Condensation of long-term wave climates for the fatigue design of hydrodynamically sensitive offshore wind turbine support structures'. In: *Ships and Offshore Structures* 11 (2 Feb. 2016), pp. 142–166. ISSN: 17445302. DOI: 10.1080/17445302.2014.967994.

[27] Aaron Henskens. 'Literature study in preparation to thesis on the topic 'Examination of environmental lumping methods for fatigue assessment of floating wind turbines'. In: (2022).

[28] Erin E. Bachynski et al. 'Wind-wave misalignment effects on floating wind turbines: Motions and tower load effects'. In: *Journal of Offshore Mechanics and Arctic Engineering* 136 (4 Nov. 2014). ISSN: 1528896X. DOI: 10.1115/1.4028028.

[29] Shengtao Zhou et al. 'Importance of platform mounting orientation of Y-shaped semi-submersible floating wind turbines: A case study by using surrogate models'. In: *Renewable Energy* 156 (Aug. 2020), pp. 260–278. ISSN: 18790682. DOI: 10.1016/j.renene.2020.04.014.

[30] Helen Ege. 'Investigation of the Tower Design for the Offshore Wind Turbine Concept OO-Star Wind Floater'. In: (2019). URL: https://ntnuopen.ntnu.no/ntnu-xmlui/handle/11250/2622953.

[31] Lin Li, Zhen Gao and Torgeir Moan. 'Joint distribution of environmental condition at five European offshore sites for design of combined wind and wave energy devices'. In: *Journal of Offshore Mechanics and Arctic Engineering* 137 (June 2015).

[32] Erin Bachynski-Polić. *During oral discussion*.

[33] SINTEF. *SIMA documentation*. https://www.sima.sintef.no/doc/4.4.0/sima/index.html. Accessed on: 2023-06-28.

[34] Matthew Hall et al. *RAFT Documentation*. https://openraft.readthedocs.io/en/latest/. Accessed on: 20/09/2022.

[35] Joep Van der Spek. 'The response of a semi-submersible floating offshore wind turbine under misaligned wind and waves'. In: *repository.tudelft.nl* (Oct. 2022).

[36] Erin Bachynski-Polić and Zhen Gao. 'Course Project 'Integrated Dynamic Analysis of Wind Turbines' of TMR03 course at NTNU'. In: (2022).

[37] Anastasios Stampoultzoglou. *During oral discussion*.

[38] John D. Holmes. *Wind Loading of Structures*. Spon Press, 2001.

[39] *TurbSim download webpage*. https://www.nrel.gov/wind/nwtc/turbsim.html. Accessed on: 2023-06-28.

[40] Evan Gaertner et al. 'IEA Wind TCP Task 37: Definition of the IEA 15-Megawatt Offshore Reference Wind Turbine'. In: (Mar. 2020). DOI: 10.2172/1603478. URL: https://www.osti.gov/biblio/1603478.

[41] Christopher Allen et al. 'Definition of the UMaine VolturnUS-S Reference Platform Developed for the IEA Wind 15-Megawatt Offshore Reference Wind Turbine'. In: (July 2020). DOI: 10.2172/1660012. URL: https://www.osti.gov/biblio/1660012.

[42] Shun-Han Yang. URL: https://homepage.ntu.edu.tw/~ntuesoe/en/faculty.html.

[43] Boris Fischer and Martin Shan. 'A survey on control methods for the mitigation of tower loads'. In: (Sept. 2013).

[44] Pär Johannesson. *tp2rfc from WAFO toolbox for MATLAB*. https://github.com/wafo-project/wafo. Accessed on: 2023-07-01.

[45] Piotr Janiszewski. *Rainflow package for Python*. https://pypi.org/project/rainflow/. Accessed on: 2023-07-01.

[46] Det Norske Veritas. *DNV-RP-C203 Fatigue design of offshore steel structures*. June 2014.

[47] Erin Bachynski-Polić and Pär Johannesson. *cc2dam_2slope MATLAB script*.

[48] Kunpeng Wang et al. 'Fatigue damage characteristics of a semisubmersible-type floating offshore wind turbine at tower base'. In: *Journal of Renewable and Sustainable Energy* 8 (5 Sept. 2016). ISSN: 19417012. DOI: 10.1063/1.4964366.

[49] J.M.J. Journée and W.W. Massie. *Offshore Hydromechanics*. Delft University of Technology, Jan. 2001.

[50] Zhen Gao. 'Lecture slides of 'Hydrodynamic analysis of offshore wind turbines' of TMR03 course at NTNU'. In: (2022).

[51] Jeroen Hoving. 'Lecture notes of 'Multi-member structures' lecture of Offshore Wind Support Structures (OE44135) course at TU Delft'. In: (2022).

[52] David Fuhrman. 'Lecture slides of 'Potential flows: Linear water waves' lecture of Hydrodynamics 2 (41111) course at DTU'. In: (2021).

[53] S.K. Chakrabarti. *Hydrodynamics of offshore structures*. WIT press, 1987.

[54] Sebastian Schreier. 'Lecture slides of 'Hydromechanic loads' lecture of Floating Structures Offshore Moorings (OE44100) course at TU Delft'. In: (2022).

[55] F. Pedregosa et al. 'Scikit-learn: Machine Learning in Python'. In: *Journal of Machine Learning Research* 12 (2011), pp. 2825–2830.

[56] *Environment: Modelling design waves*. OrcaFlex. URL: https://www.orcina.com/webhelp/OrcaFlex/Content/html/Environment,Modellingdesignwaves.htm.

[57] Colin MacFarlane. *Wikipedia contribution of Lloyds Register of Shipping Professor of Subsea Engineering at Strathclyde University, Glasgow from 1986 until 2005, Department of Naval Architecture Marine*. https://en.wikipedia.org/wiki/Talk%3AWave_period. Accessed on: 30/10/2023.

[58] SINTEF. *SIMA documentation SIMO theory JONSWAP formula*. https://www.sima.sintef.no/doc/4.4.0/simo/theory/environment.html. Accessed on: 2023-07-27.

[59] SINTEF. *SIMA documentation RIFLEX input data JONSWAP formula*. https://sima.sintef.no/doc/4.4.0/riflex/userguide/inpmod/environmental_data.html. Accessed on: 2023-07-27.

[60] B. Evans. 'Lumping of Fatigue Load Cases'. In: *RECOFF Document No. 16a.* (2004).

[61] Det Norske Veritas. *DNV-RP-C205 Environmental Conditions and Environmental Loads*. Oct. 2010.

[62] *scipy.signal.filtfilt() documentation*. https://docs.scipy.org/doc/scipy/reference/generated/scipy.signal.filtfilt.html. Accessed on: 2023-07-26.

[63] *scipy.signal.butter() documentation*. https://docs.scipy.org/doc/scipy/reference/generated/scipy.signal.butter.html. Accessed on: 2023-07-26.

[64] Charles R. Harris et al. 'Array programming with NumPy'. In: *Nature* 585.7825 (Sept. 2020), pp. 357–362. DOI: 10.1038/s41586-020-2649-2. URL: https://doi.org/10.1038/s41586-020-2649-2.

[65] George Katsikogiannis. *Estimation of Long-Term Fatigue and Extreme Responses of Large-Diameter Monopiles for Offshore Wind Turbines*. NTNU, To be published February 2024.

[66] Lin Chen and Biswajit Basu. 'Fatigue load estimation of a spar-type floating offshore wind turbine considering wave-current interactions'. In: *International Journal of Fatigue* 116 (Nov. 2018), pp. 421–428. ISSN: 01421123. DOI: 10.1016/j.ijfatigue.2018.06.002.

Appendix

A Decay test

In this study, the decay test is used that was designed for an NTNU course [36]. In this test, a force or moment is applied at the start of the simulation. For the first 100 s, the force or moment increases from zero to its final magnitude. For the next 100 s the force stays constant. After a total of 200 s, the force is removed. This force or moment is applied at the tower base. Table 11 shows the force and moment magnitudes and the simulation lengths that are used for each motion. In this table, $\hat{v}$ represents the unit vector that defines the direction of the force or moment, according to the global set of axes in SIMA (see Figure 53).

Direction:	Force [MN]:	Moment [MNm]:	Simulation length [s]:	$\hat{v}_x$	$\hat{v}_y$	$\hat{v}_z$
Surge	2.25	0	1200	1	0	0
Sway	2.25	0	1200	0	1	0
Heave	10	0	800	0	0	1
Roll	0	530	800	1	0	0
Pitch	0	530	800	0	1	0
Yaw	0	10	1200	0	0	1

Table 11: Input values used during the decay tests

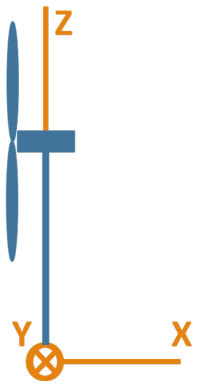

Figure 53: Global set of axes in SIMA

Next, the frequency of each motion was obtained at which the floater oscillated after the force was removed. These frequencies are the natural frequencies of the motions. The fore-aft and side-side natural frequencies were obtained in the same way, from the M_y and M_z graphs respectively (using SIMA's local set of axes shown in Figure 16.a). The decay test results are shown in Figure 54 and Figure 54. Here, the red dots mark the peaks that were taken into account when determining the natural frequency f_n of each motion. In Table 6, the natural frequencies observed in these tests are compared to the natural frequencies in the floater documentation [41].

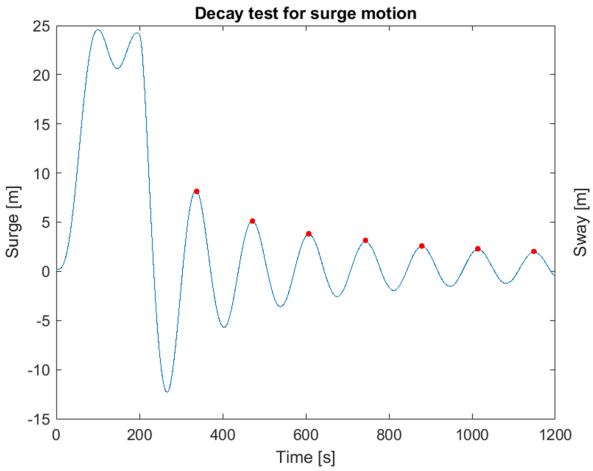

(a) Surge decay test ($f_{n,surge}$ = 0.007374 Hz)

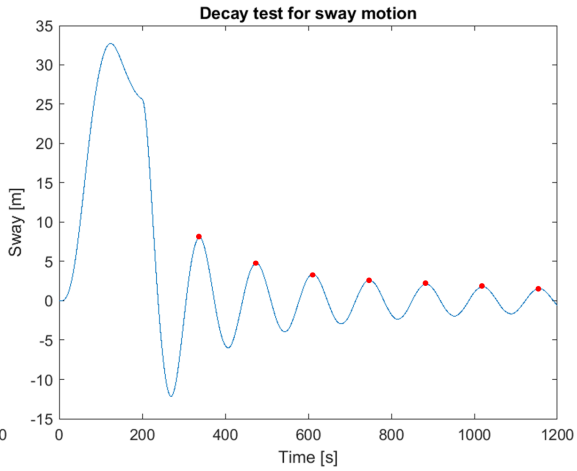

(b) Sway decay test ($f_{n,sway}$ = 0.007347 Hz)

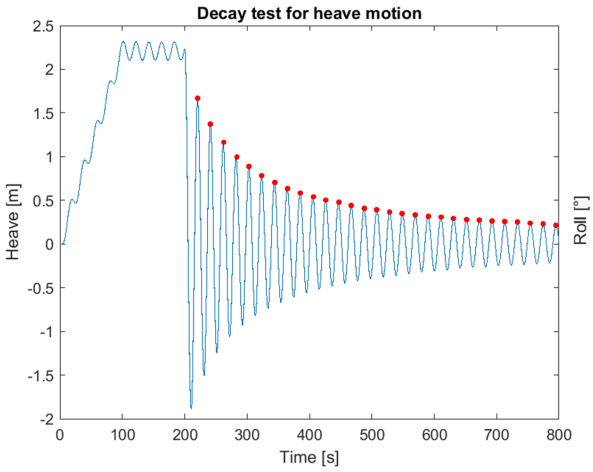

(c) Heave decay test ($f_{n,heave}$ = 0.04868 Hz)

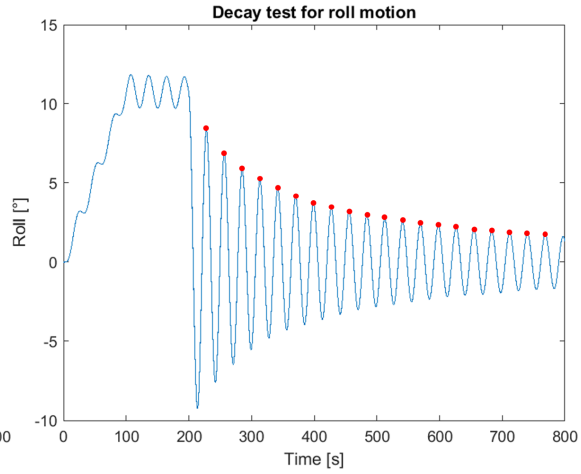

(d) Roll decay test ($f_{n,roll}$ = 0.03514 Hz)

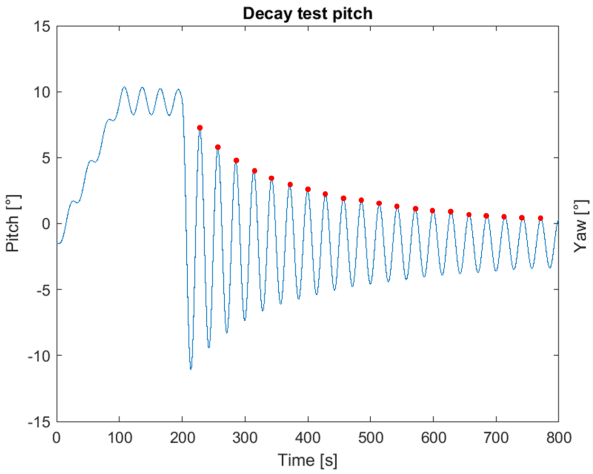

(e) Pitch decay test ($f_{n,pitch}$ = 0.03500 Hz)

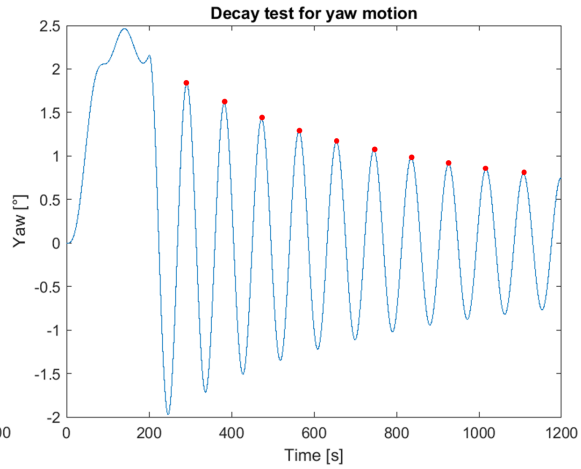

(f) Yaw decay test ($f_{n,yaw}$ = 0.01104 Hz)

Figure 54: Results of the decay tests

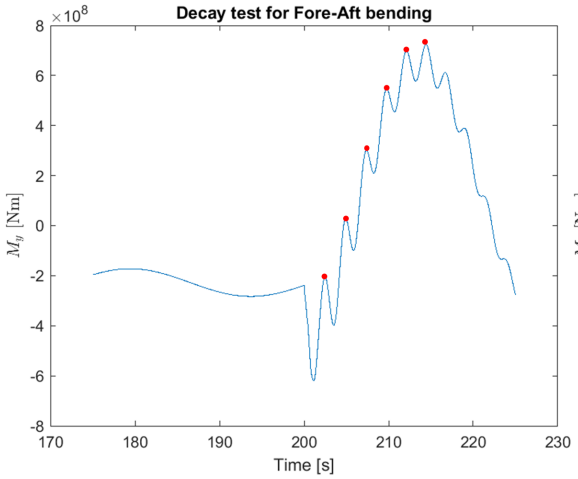

(g) Fore-aft decay test ($f_{\mathrm{n,FA}}$ = 0.4181 Hz)

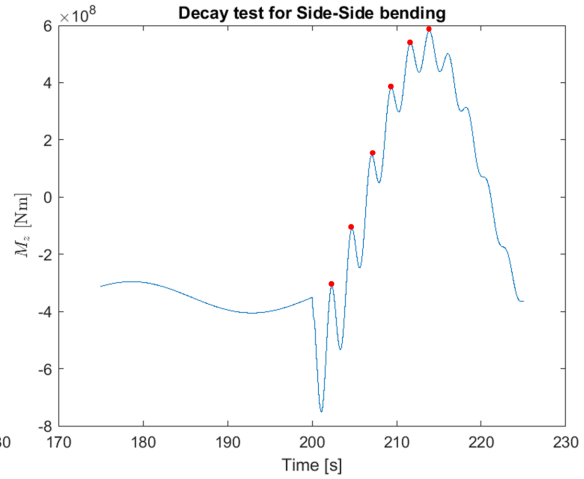

(h) Side-side decay test ($f_{\mathrm{n,SS}}$ = 0.4342 Hz)

Figure 54: Results of the decay tests (cont.)

B Checking the stress formulas on plausibility

After removing the 400 s transient, the SIMA time series of the internal forces are substituted into Equation 7 and Equation 8, yielding the axial and shear stress time series for every value of η. For every axial and shear stress time series, the fatigue damage can be computed using the method described in Section 3.
These results will now be checked on plausibility. To do so, the one-hour time series are computed for a weather condition with a wind speed of 14 m/s and where the wind and wave directions are equal to $\tau = 0°$.
The internal load results will be discussed first. The purpose of this study is to check whether the loads from SIMA roughly fit the turbine characteristics, described in the documentation [40] [41]. Slight differences are allowed, due to small differences in the assumptions made by the two models. It is not the goal of this study to derive how SIMA computed these loads in great detail.

- The mean N_x is -10.2 MN at the tower top and the mean N_x is -21.8 MN at the tower base. N_x should be relatively large compared to other loads as it is dominated by the weight of the RNA and tower. As the weight is a downward force causing compression, N_x is negative. These N_x's result in an RNA mass of 1,040 tons (1,017 tons according to documentation [40]) and a tower mass of 1,182 tons (1,263 tons according to documentation [41]).
- The mean M_x is 0.438 MNm. M_x is the same for the tower top and the tower base, as no torsion can be applied along the tower due to its circular cross-section. The M_x is relatively small compared to other loads, as no major external forces or moments contribute to this internal moment.
- The mean M_y is -181 MNm at the tower base. This force is large and negative, as the thrust force creates a large positive moment around the Y-axis. Assuming a 130 m tower length [41], the thrust force resulting from M_y has a magnitude of 1.39 MN. SIMA shows a mean thrust force of 1.37 MN and the documentation [40] shows a thrust force of 1.7 MN at 14 m/s. The thrust force according to the documentation is an overestimation, as explained in Section 2.4.1).
- The mean M_z is -41.7 MN at tower base. This value is significantly smaller than M_y as the thrust force generally does not affect M_z.
- The mean V_z is 1.67 MN at tower top and 2.10 MN at tower base. V_z at tower top includes the thrust force (about 1.37 MN) and perhaps some more aerodynamic drag effects. The increase in V_z along the tower is most likely due to the drag of the tower.
- The mean V_y is 0.143 MN at tower top and 0.226 MN at tower base. These values are significantly smaller than V_z, as V_y is generally not affected by the thrust force and drag effects are small, since the wind direction is equal to $\eta = 0°$.

Figure 55 shows how the standard deviation (STD) of the axial and shear stress time series and the corresponding fatigue damages fluctuate for different values of η. The plausibility of these graphs will now be analysed.

- The fatigue damage is computed by Equation 1 and increases for larger stress ranges. As stress ranges increase, the STD of the stress time series increases as well. This is why the STD graph and the fatigue damage graph have similar shapes.

- M_y is much larger than M_z. As Equation 7 shows, M_y's contribution to the axial stress is multiplied by the cosine of η. Physically, this is because the M_y is largest at $\eta = 0°$ and $\eta = 180°$. For this reason, its STD shows a cosine-like shape.

- V_z is much larger than V_y. As Equation 8 shows, M_z's contribution to the shear stress is multiplied by the sine of η. Physically, this is because the V_z is largest at $\eta = 90°$ and $\eta = 270°$. For this reason, its STD shows a sine-like shape.

- The peaks of the shear stress STD have different heights. This is due to the fact that the positive M_x causes the shear stress caused by M_x to be positive for both $\eta = 90°$ and $\eta = 270°$ (see Figure 17.e). On the other hand, the negative V_z causes V_z's shear stress to be negative for $\eta = 270°$ (see Figure 17.b). For $\eta = 90°$, as the Z-axis flips to the left, the positive V_z also points left, causing the shear stress contribution of V_z to be positive. Because of this, at $\eta = 90°$ the positive shear stress caused by M_x and V_z are summed. At $\eta = 270°$, a positive value for the M_x's shear stress and a negative value for the V_z's shear stress are summed. This results in a lower shear stress at $\eta = 270°$ than at $\eta = 90°$. For this reason, the STD graph of neither the axial stress nor the shear stress is symmetrical at any angle η. For the axial stress STD graph, the difference between the peaks is much smaller, due to M_y dominating over N_x.

- The M_y moment is the largest internal load. As only the axial stress if affected by M_y, the fatigue damage of the axial stress is a factor 10^3 larger than the fatigue damage of the shear stress.

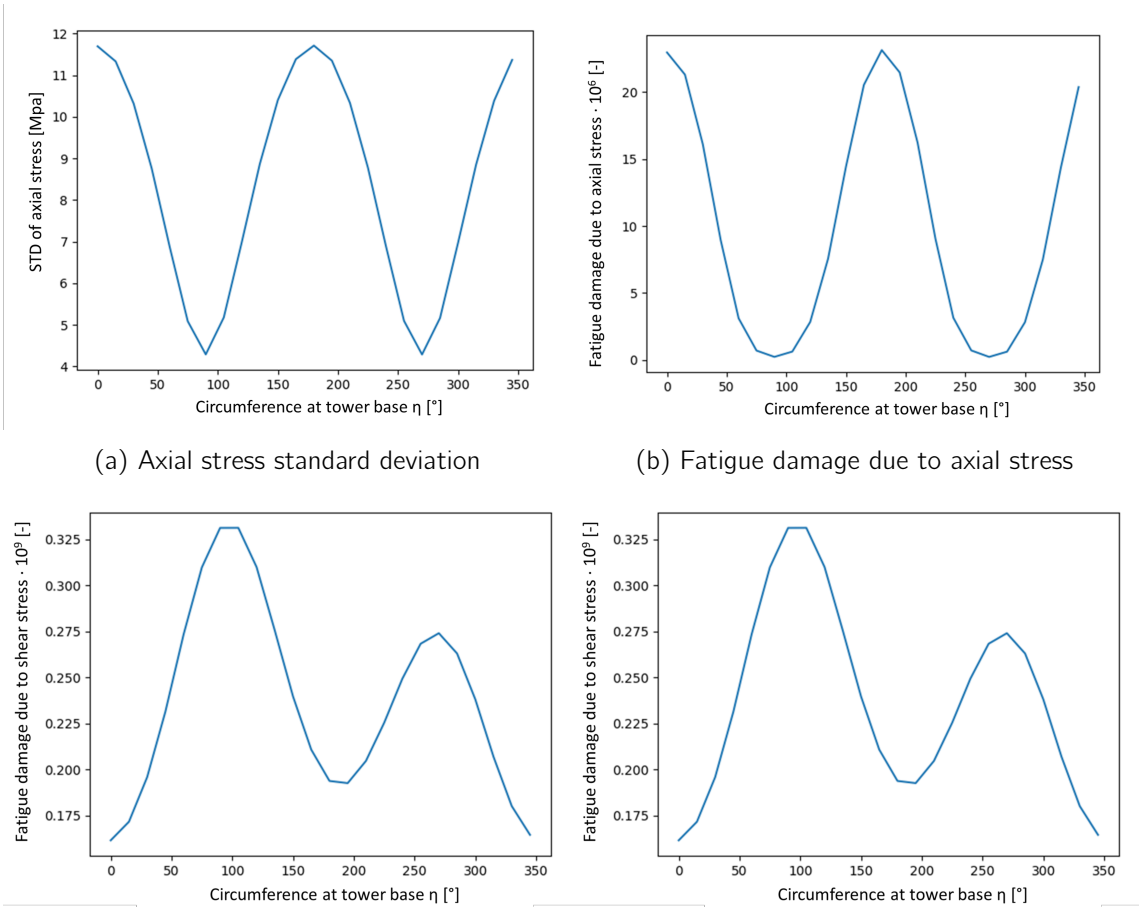

(a) Axial stress standard deviation

(b) Fatigue damage due to axial stress

(c) Shear stress standard deviation

(d) Fatigue damage due to shear stress

Figure 55: Graphs showing the standard deviations of the axial and shear stress time series at the tower base and the resulting fatigue damages, for different values of η

C JONSWAP spectrum

The JONSWAP model used to perform the time domain load simulations is computed by SIMA, as explained in its documentation [33].
In order to apply some of the lumping methods, a JONSWAP spectrum is needed as well. Many variations on the JONSWAP spectrum and its parameters are defined in research. Using a different JONSWAP spectrum from the spectrum used in SIMA may result in lumping method inaccuracies that can be explained by the use of a different JONSWAP spectrum. For this reason, the same JONSWAP spectrum was used to apply the lumping methods, as the spectrum used by SIMA. It must be noted that the SIMA documentation gives different JONSWAP formulas. The formula given in the SIMO theory guide [58] approaches infinity. The formula given in the RIFLEX guide (input to INPMOD) [59] approximates the JONSWAP spectrum that SIMA gives as an output. Therefore, the latter spectrum is used. This spectrum is similar to the spectrum given in another recent paper [60], that studied the optimisation of the JONSWAP spectrum.
This spectrum is described by Equation 59, Equation 60 and Equation 61. Here, g (gravitational acceleration) is set to 9.81 m/s^2 and dimensionless factor β is set to $\frac{5}{4}$. ω equals $2\pi \cdot f$, where f is the frequency. In this study, f ranges from 0 Hz to 0.7 Hz as motivated in Appendix E. ω_p equals $2\pi T_p$.

$$S_{\zeta\zeta} = \frac{\alpha g^2}{\omega^5} \exp\left(-\beta \left(\frac{\omega_p}{\omega}\right)^4\right) \gamma^{\exp\left(-\frac{(\omega-\omega_p)^2}{2\sigma^2\omega_p^2}\right)} \tag{59}$$

$$\sigma = \begin{cases} 0.07, & \text{for } \omega \leq \omega_p \\ 0.09, & \text{for } \omega > \omega_p \end{cases} \tag{60}$$

$$\alpha = \left(\frac{H_s \cdot \omega_p^2}{4 \cdot g}\right)^2 \cdot \frac{1}{0.065 \cdot \gamma^{0.803} + 0.135} \tag{61}$$

For both the SIMA model and the lumping methods, γ was computed according to the DNV-RP-C205 recommendation [61], as shown in Equation 62.

$$\gamma = \begin{cases} 5, & \text{for } \frac{T_p}{\sqrt{H_s}} \leq 3.6 \\ \exp\left(5.75 - 1.15 \cdot \frac{T_p}{\sqrt{H_s}}\right), & \text{for } 3.6 < \frac{T_p}{\sqrt{H_s}} < 5 \\ 1, & \text{for } \frac{T_p}{\sqrt{H_s}} \geq 5 \end{cases} \tag{62}$$

This spectrum is defined, assuming the frequency is given in rad/s. In order to convert the spectrum to a frequency in Hz, the spectrum is multiplied by 2π, as Equation 63 shows.

$$[S_{\zeta\zeta}] = \frac{[H_s]^2}{[f]} = \frac{[H_s]^2}{[\omega] \cdot \frac{1}{2\pi}} = \frac{[H_s]^2}{[\omega]} \cdot 2\pi \tag{63}$$

D The S-N curve

An S-N curve gives the relation between a given stress range S and the maximum number of cycles N the specified material can endure before material failure occurs. In this thesis, a bilinear S-N curve is used primarily (see Section 3.2.1 for an explanation). Here, the slope m depends on the number of cycles N. Nevertheless, some lumping methods require a value for m but do not offer the possibility to specify m for different cycle counts. This is due to the fact that the stress ranges can only be computed if a load analysis is performed. Lumping methods do not always offer an estimation of these stress ranges and therefore a bilinear S-N curve cannot be used. To solve this issue, a linear S-N curves was created that approximates the bilinear S-N curve.
In order to find a linear approximation of the bilinear S-N curve, the contribution to the fatigue damage is computed for both sections of the bilinear S-N curve.
First, for each scatter diagram the fatigue damage is computed using the bilinear S-N curve (symbolized as D_{total}). While doing so, the fatigue damages of stress ranges higher than 52.63 MPa are summed (symbolized as $D_{\text{m = 3}}$) and the fatigue damages of stress ranges lower than 52.63 MPa are summed (symbolized as $D_{\text{m = 5}}$). Next, the contribution of both curves is computed using Equation 64 until Equation 68. Here, N_{ss} equals the number of sea states in the scatter diagram, $N_{stress,j}$ equals the number of stress ranges for sea state j counted during rainflow counting, p_j equals the probability of occurrence of sea state j, n_i equals the number of cycles for stress range i counted during rainflow counting, and N_i equals the maximum number of cycles that the material that withstand before material failure occurs, as defined in the S-N spectrum.

$$D_{\text{m = 3}} = \sum_{j=1}^{N_{ss}} p_j \cdot \sum_{i=1}^{N_{stress,j}} \begin{cases} \frac{n_i}{N_i}, & \text{if } N_i < 10^7 \\ 0, & \text{if } N_i \geq 10^7 \end{cases} \tag{64}$$

$$D_{\text{m = 5}} = \sum_{j=1}^{N_{ss}} p_j \cdot \sum_{i=1}^{N_{stress,j}} \begin{cases} 0, & \text{if } N_i < 10^7 \\ \frac{n_i}{N_i}, & \text{if } N_i \geq 10^7 \end{cases} \tag{65}$$

$$D_{\text{total}} = \sum_{i=1}^{N_{ss}} p_j \cdot \sum_{i=1}^{N_{stress,j}} \frac{n_i}{N_i} \tag{66}$$

$$\text{Contribution}_{\text{m = 3}} = \frac{D_{\text{m = 3}}}{D_{\text{total}}} \cdot 100\ \% \tag{67}$$

$$\text{Contribution}_{\text{m = 5}} = \frac{D_{\text{m = 5}}}{D_{\text{total}}} \cdot 100\ \% \tag{68}$$

The results of this experiment are shown in Figure 56. This figure shows that stress ranges lower than 52.63 MPa contribute the most to the fatigue damage. This corresponds to a slope m with a value of 5.

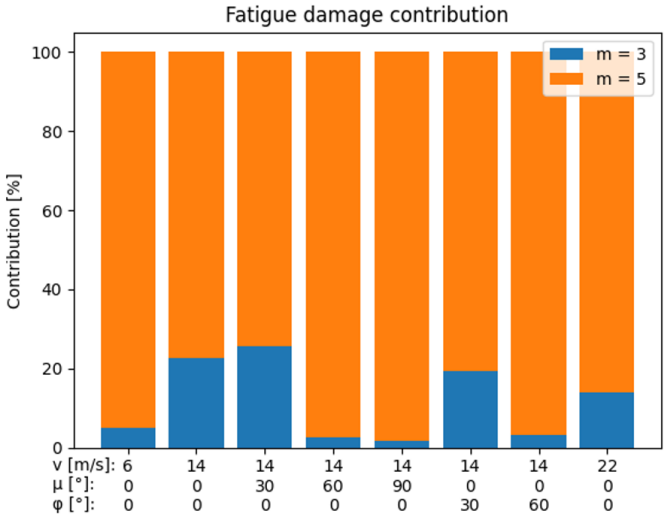

Figure 56: The fatigue damage contribution of the stress ranges higher than 52.63 MPa (where $m = 3$) and lower than 52.63 MPa (where $m = 5$)

To conclude, whenever the value for m needs to be defined in a lumping method, but a bilinear S-N curve cannot be applied, $m = 5$ offers the best approximation. This is confirmed by Figure 57. Here, the fatigue damage of the entire scatter diagram computed using a linear S-N curve with either assuming the S-N curve for $S \geq 52.63$ MPa for all stress ranges (see $m = 3$ in the graph) or assuming the S-N curve for $S < 52.63$ MPa for all stress ranges (see $m = 5$ in the graph), is compared to the fatigue damage computed using the bilinear S-N curve. According to the figure, using a linear S-N curve with a slope of 5, approximates the fatigue damage resulting from the bilinear curve best. This corresponds to the conclusion of a similar test performed on a monopile in a previous study [9].

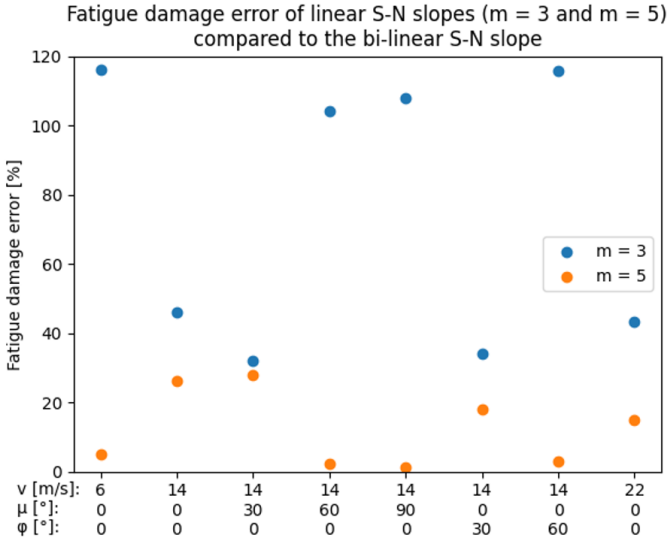

Figure 57: The fatigue damage error assuming $m = 3$ and assuming $m = 5$ for every stress range

To increase the accuracy of the fatigue damage resulting from the linear S-N curve even

more, a new linear S-N curve could be computed that approximates the bilinear S-N curve. To do this, a new value for m and a new value for $\log(\bar{a})$ need to be determined. To find these values a similar study can be performed as explained above, where these two parameters are adjusted to match the fatigue damage computed using the bilinear S-N curve.
Nevertheless, a slope of 5 was considered accurate enough for this study, for the following reasons:

- A lumping methods should approximate the fatigue damage gradient instead of the absolute fatigue damage and might therefore be more robust considering simplifications during the fatigue damage calculation.
- The goal of a lumping method is to increase computational speed and in order to do so, numerous simplifications are made. It is doubtable whether creating a new S-N curve instead of using the $m = 5$ slope of the bilinear S-N curve will increase the accuracy of the lumping method significantly.
- When a lumping method is applied during a commercial project, there will most likely not be enough time to perform the study explained above on which linear S-N curve approximates the bilinear S-N curve best, as this study requires many time domain computations. In this situation, it is likely that turbine developers will rather estimate m based on their knowledge of the model.

E Frequency domain load calculation

In order to perform a load calculation in frequency domain, first a white noise wave spectrum is created, ranging 0 Hz to 0.7 Hz (as motivated at the end of this section). The spectral density is computed using Equation 69. For H_s the weighted average (weighted according to the number of occurrences) of the scatter diagram is used.

$$S_{\zeta\zeta,\text{ white noise}} = \frac{\left(\frac{H_s}{4}\right)^2}{0.5\text{ Hz} \cdot 2\pi} \tag{69}$$

This equation is derived using the fact that $H_s = 4\sqrt{m_0}$, and therefore $m_0 = \left(\frac{H_s}{4}\right)^2$. As Equation 34 shows, m_0 equals the area below the spectrum. Therefore, the area below the spectrum should be equal to $\left(\frac{H_s}{4}\right)^2$. As a white noise spectrum has a constant spectral density for each frequency, it has a rectangle shape. As the area and the frequency range ($\Delta f = 0.7$ Hz) are known, the spectral density can now be computed by dividing the area by the frequency range, as Equation 69 shows. Figure 58 shows an example of a white noise spectrum used in this study.

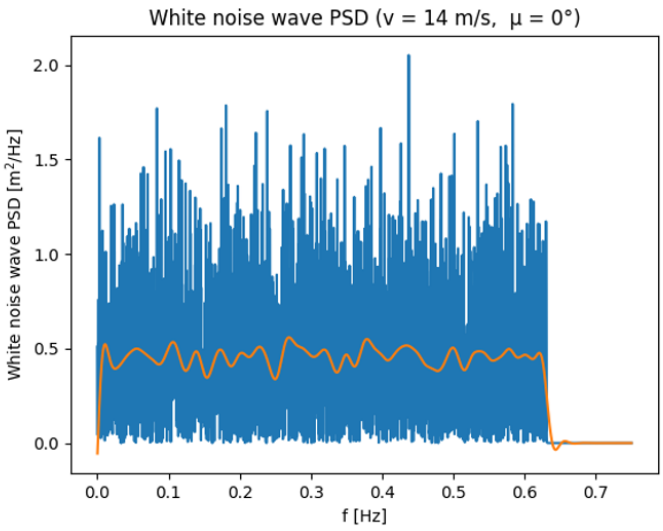

Figure 58: White noise wave spectrum (blue: original, orange: smoothened)

Now a 4000 s (including a 400 s transient) time domain simulation is run and the axial stress time series is computed as explained in Section 2. What effects (like turbulence or tower shadowing) are included in the time domain load simulation model, may be adjusted according to the research goal (this will be specified in the main body of this thesis, whenever this appendix is being referred to). Next, the axial stress time series is calculated (see Section 3.1) and the stress PSD is computed. An example is shown in Figure 59.

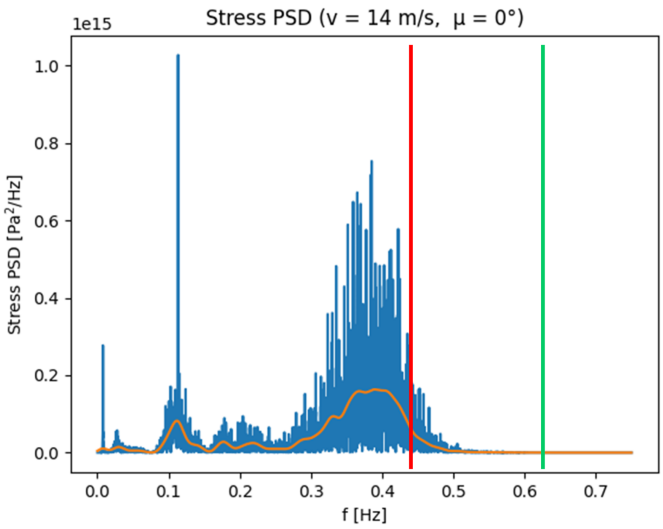

Figure 59: Axial stress PSD resulting from white noise computation (blue: original, orange: smoothened, red: 0.45 Hz, green: 0.63 Hz)

Using Equation 70, the transfer function H is computed. H represents the linear relation between the wave height and the axial stress at tower base. In this formula, the original spectra for $S_{\zeta\zeta,\text{ white noise}}$ and $S_{\sigma\sigma,\text{ white noise}}$ were used to compute the transfer function H. Next, H was smoothened using the Python function scipy.signal.filtfilt() [62]. As recommended by the filtfilt documentation, the input values b and a were computed using scipy.signal.butter() [63]. Using trial and error and based on examples available online, the input values for N (order of the filter) and W_n (critical frequency) were set to 4 and 0.02 respectively. The goal of smoothing the transfer function is to keep the peaks caused by higher stresses due to natural frequencies and to remove peaks that are due to turbulence. The same smoothening parameters were used for any smoothened graph used in this thesis.

$$H_{\zeta\sigma} = \sqrt{\frac{S_{\sigma\sigma,\text{ white noise}}}{S_{\zeta\zeta,\text{ white noise}}}} \tag{70}$$

As Equation 71 shows, the stress spectrum as a result of any JONSWAP wave spectrum can now be computed.

$$S_{\sigma\sigma} = H_{\zeta\sigma}^2 \cdot S_{\zeta\zeta}(H_s, T_p) \tag{71}$$

Once the stress spectrum is known, a stress time series is calculated using the inverse fast Fourier transform function of the Python package NumPy [64]. Now, rainflow counting is applied and the fatigue damage is computed as explained in Section 3.

Frequency range

In the original study where this frequency domain load calculation was applied on a monopile [16], a frequency range of 0 to 0.5 Hz was used. Using this range, SIMA yields a white noise spectrum ranging from 0 to 0.45 Hz. As the first natural frequencies of a semi-submersible tower are much higher (f_{FA} = 0.404 Hz and f_{SS} = 0.419 Hz) than the ones of a monopile, this thesis uses a frequency range of 0 to 0.7 Hz. In practice, this results in a SIMA white noise spectrum ranging from 0 to about 0.63 Hz. Figure 59 shows a stress PSD resulting from a white noise simulation in SIMA. This PSD shows that stresses at frequencies higher than 0.45 Hz are possible, whenever these frequencies are excited. Yet, it is unlikely that the JONSWAP spectrum reaches these frequencies.

F Block partitioning algorithm

The block size is an input parameter of the function, defined as the number of sea states per block. The actual number of sea states per block may not be equal to the block size. This depends on the shape of the scatter diagram.
First, the block dimensions are determined by assuming a(n) (almost) square block shape for any block size. For example, for a block size 10 the block shape will be 3 by 3; for a block size 20 the block shape will be 5 by 4; and for a block size 40 the block shape will be 7 by 6. Here, the first value is equal to the number of H_s values that will be covered by the block and the second value represents the number of T_p values covered by the block.
For each block, the H_s range and the T_p range is determined. The blocks are stored in a list, starting with the blocks with the lowest H_s range (the T_p range ordered from low to high for every H_s range).
A scatter diagram almost never has a rectangular shape. In other words, it almost never occurs that every combination of H_s and T_p in the diagram has a number of occurrences higher than zero. If a block contains less sea states than 20% of the 'block size' input value, then the following happens:

- If the next block exists and if it is not empty, then the block is added to the next block in the list.
- If the next block is an empty block or if it does not exist, the block is added to the previous block, if it exists and if it is not empty.

It is very likely that the last block of every H_s range is empty, as the highest T_p range often only occurs for the lowest H_s range. This prevents these last block of an H_s range to be added to the first block of the next H_s range. Of course, this depends on the set block size and the scatter diagram. Therefore, this method may not work for all scatter diagrams and the block partitioning must be checked manually. No manual alterations to the block partitioning were necessary for the scatter diagrams used in this study.
Cases that are not covered by this code are listed below. These cases are considered as rare. If they occur, nothing happens.

- The first block in the list contains less than 20% of the block size value and the next block is empty.
- The last block in the list contains less than 20% of the block size value and the previous block is empty.

Lastly, all empty blocks are deleted.

G Estimation of computational time needed to compute entire hindcast

As explained in Section 6.1, 20451 time domain load simulations need to be performed in order to compute the entire hindcast. Forty simulations can be run simultaneously. This takes 40 minutes.
One time domain simulation takes up about 1.3 GB of memory. Due to the server's limited memory space of 400 GB, of which 100 GB will be used by supportive files (wind files (37 GB), SIMA back-ups, Matlab post-processing results, plus some free space being reserved for unexpected larger files and intermediate tests that might be needed), about six sets of 40 time domain simulations fit on the server in practice. Post-processing 240 time domain simulations in MATLAB takes about 45 minutes. During the post-processing, the fatigue damage computation is performed and the file size of a single simulation is reduced to 60 MB. It is not recommended to perform the MATLAB post-processing while running the next SIMA batch, as both processes might slow down significantly and this might even cause SIMA to crash or errors to appear. Then the simulations must be downloaded from the server. This requires the files to be uploaded to a drive and to be downloaded onto the personal computer. The server experienced an uploading speed of 100 MB/s and the personal computer experienced a downloading speed of 1.2 MB/s, resulting in a total time of 3 hours and 20 minutes (2.4 minute uploading and the remaining time downloading). Nevertheless, this can be done while running the next 240 batch in SIMA, that takes 4 hours to run. In order to store 20451 60 MB files, the personal computer needs about 1.23 TB of free space, which is a lot, yet doable.
Using this working set up, running 240 time domain simulations will take about 4 hours and 45 minutes in total. This results in 405 hours of work, including 341 hours of SIMA computational time. If starting SIMA, starting the post-processing and downloading the files from the server is completely automised and doesn't require any manual operation by a person, then the 405 hours of work is equivalent to about 16 days. Automating these processes requires advanced knowledge on information technology (IT). If these processes need to be operated manually (as was the case during this study), two sets of 240 simulations can be run each day for five days a week. In this case, it takes almost 9 weeks to compute the entire hindcast. Yet, server downtime, unexpected errors by SIMA and MATLAB, slow internet and human mistakes will slow down the computation. Sporadically (roughly once per 1000 simulations), the combination of a wave seed with certain environmental conditions creates an error by SIMA. In these cases, the sea state must be rerun using a different wave seed. For these reasons, 10 weeks is considered an optimistic estimation of the time needed to compute the 20451 time domain load simulations.

H Lumping multiple sets of waves

The Katsikogiannis lumping method has been further developed for bimodal sea states, including wind-sea and swell components, described and validated in detail in [65]. The steps below describe how this method of lumping both wind waves and swell, is applied:

1. Scatter diagrams are created, using wind speed and 'wind'-'wind wave' misalignment as filters and plotting the wind sea H_s and T_p on the axes of the diagram. These scatter diagrams are lumped, each yielding a single lumped sea state.
2. In the environmental data set, the swell directions are collected that occur at this wind speed and wind wave direction.
3. Scatter diagrams are created, using wind speed and 'wind'-'swell' misalignment as filters and plotting the swell H_s and T_p on the axes of the diagram. These scatter diagrams are lumped, each yielding a single lumped sea state.

Each wind wave lumped sea state now had several corresponding swell lumped sea states. For example, let us assume that the environmental data set contains a single wind speed and three 'wind'-'wind wave' misalignments. This yields three wind wave lumped sea states. The environmental data set shows that each of these three wind wave lumped sea states can occur at three different swell direction, resulting in nine swell lumped sea states. Now, the fatigue damage caused by this environmental data set should be computed using these nine combinations of wind sea lumped sea states and swell lumped sea states.

I Validity of RAFT

RAFT [34] is a Python frequency domain model for performing load analysis on a floating wind turbine. When comparing the RAFT to hydrodynamics that affects fatigue damage for a semi-submersible, the following conclusions are drawn on the validity of the RAFT model:

1. Diffraction affects the fatigue damage of a semi-submersible. In RAFT, diffraction is taken into account when calculating the forces on the columns, but it is neglected for the pontoons.

2. The drag force is estimated using structure motion response iteration in the RAFT model [35]. This estimation does not have to undermine the validity of the RAFT model, as the floaters are inertia dominated. For this reason, a small error in drag force is acceptable.

3. The mooring offset is only determined by the wind force in the RAFT model [35]. Wind-wave misalignments where the wave direction dominates the maximum fatigue damage at the tower base circumference [28], might be misrepresented.

4. In a frequency domain analysis it is assumed that the H_s is linear to the loads. Previous research [28] found a positive relation between H_s and the fatigue damage of a spar for all wind-wave misalignments and for a semi-submersible for wind-wave misalignments lower than 60°. For higher wind-wave misalignments of a semi-submersible, the fatigue damage stayed about constant when the H_s increased, suggesting a non-linear relationship between wave height and loads. This may be misrepresented by this frequency domain method.

5. At some wave directions the floater might experience an increase in resonance due to the wave length and the distance between the floater columns [28]. This is not accounted for by RAFT as RAFT computes the forces acting on the structure by evaluating every column and pontoon individually.

6. According to previous research [35], degrees of freedom with a natural frequency that is lower than the wave frequency, are prone to be excited by higher order wave loads. For a semi-submersible this is often the case for the motion natural frequencies. Higher order wave loads are not taken into account by RAFT.

7. RAFT does not take current into account, while OrcaFlex does [35]. A study [66] showed how wave-current interactions could influence the fatigue damage of the mooring lines. It is not known whether these interactions discussed are taken into account in OrcaFlex. As this report focuses on the fatigue damage of the tower base, these effects might be of less relevance. Further literature on effects of current on tower base fatigue of floating turbines was not found.

8. RAFT assumes a rigid tower, while BHawC/OrcaFlex does not [35]. This will lead to a different response, as the response of the bending modes are not taken into account in RAFT. This assumption might lead to a high inaccuracy when computing the fatigue damage at tower base, since the natural frequency of the tower can be excited by lowere T_p's.

Previous research [35] studied the validity of the RAFT model by comparing it to the BHawC/OrcaFlex model when determining the bending moment at the tower base for

misaligned wind and waves. Figure 60 shows the cases that were investigated and Table 12 shows the environmental parameters used for each case. Two wave systems were used. The first system represents waves and the second system represents swell.

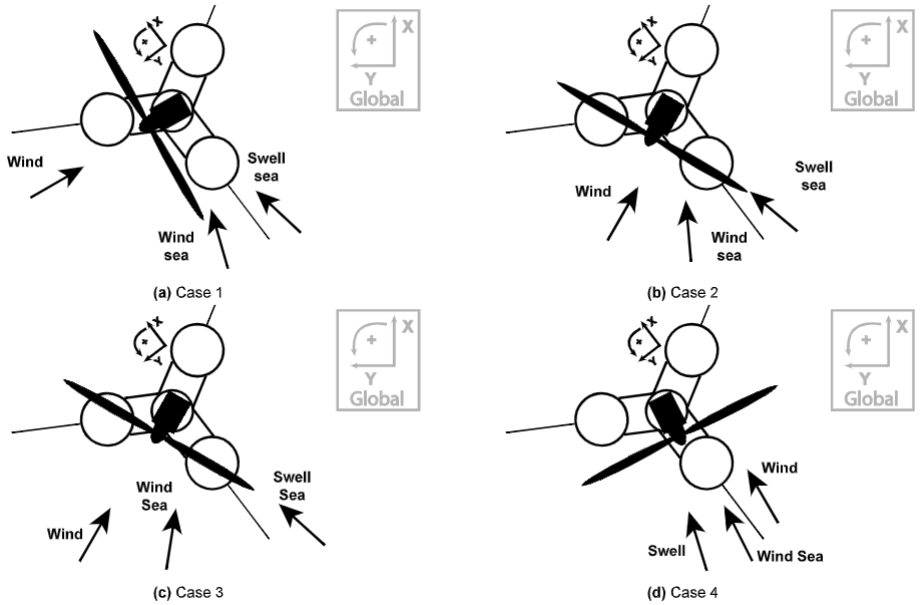

Figure 60: Load analysis cases configurations in previous research that were calculated using BHawC/OrcaFlex and RAFT to compare results. [35]

Property	Case 1	Case 2	Case 3	Case 4
Wind excitation:				
U [m/s]	4.00	9.00	15.00	25.00
Turbulence intensity	0.17	0.10	0.09	0.09
θ_{wind} [deg]	262.50	292.50	292.50	352.50
Yaw error [deg]	0.00	0.00	0.00	0.00
Wave system 1:				
T_p [s]	6.67	5.98	6.14	9.18
H_s [m]	0.94	1.02	1.54	3.40
γ	1.46	1.42	1.44	1.99
θ_{wave1}	338.21	327.27	313.37	349.84
Wave system 2:				
T_p [s]	10.15	9.86	10.26	9.18
H_s [m]	0.74	0.83	0.65	2.66
γ	2.05	1.70	2.03	1.87
θ_{wave2}	9.24	12.78	10.74	339.38

Table 12: Load analysis cases parameters in previous research that were calculated using BHawC/OrcaFlex and RAFT to compare results. For the wind excitation wind speed, turbulence intensity, wind direction and yaw error are given. For the two wave systems (1: waves, 2: swell) the wave period, wave height, damping coefficient and wave direction are given. [35]

Table 13 and Table 14 show the difference in motion responses for the RAFT model and the BHawC/OrcaFlex model. The difference in responses are calculated for the four cases, each

time for a wind-only, wave-only and wind-wave model. As shown, the differences are rather large. The wave-only case seems to perform best and the wind-only case seems to perform worst.

	Case 1			Case 2		
	Wi	Wa	Wi-Wa	Wi	Wa	Wi-Wa
Surge	-104.86	6.22	4.08	194.63	14.08	-57.85
Sway	44	-35.55	-38.75	74.41	-36.72	-47.96
Heave	529.60	3.07	3.14	148.28	11.74	11.17
Roll	266.21	-33.14	266.16	-0.76	-25.96	67.27
Pitch	234.11	29.88	28.72	-42.26	37.95	73.13
Yaw	-103.5	-33.94	-50.17	-104.52	-23.50	-75.96

Table 13: Difference in percentage between motions computed by BHawC/OrcaFlex and motions computed by RAFT for case 1 and case 2. For negative values the result of BHawC/OrcaFlex was higher than the result of RAFT (Wi: wind-only, Wa: wave-only, Wi-Wa: wind-wave) [35]

	Case 3			Case 4		
	Wi	Wa	Wi-Wa	Wi	Wa	Wi-Wa
Surge	206.74	-33.27	-56.71	140.24	9.91	23.32
Sway	73.38	-21.55	-10.54	-45.41	3.00	-15.27
Heave	173.33	-4.19	-6.99	415.39	22.38	19.30
Roll	4.34	-14.73	32.17	-72.69	14.88	-40.49
Pitch	-21.29	11.89	22.46	-31.44	32.98	220.71
Yaw	-104.33	-46.72	-71.87	-82.00	9.91	-17.02

Table 14: Difference in percentage between motions computed by BHawC/OrcaFlex and motions computed by RAFT for case 3 and case 4. For negative values the result of BHawC/OrcaFlex was higher than the result of RAFT (Wi: wind-only, Wa: wave-only, Wi-Wa: wind-wave) [35]

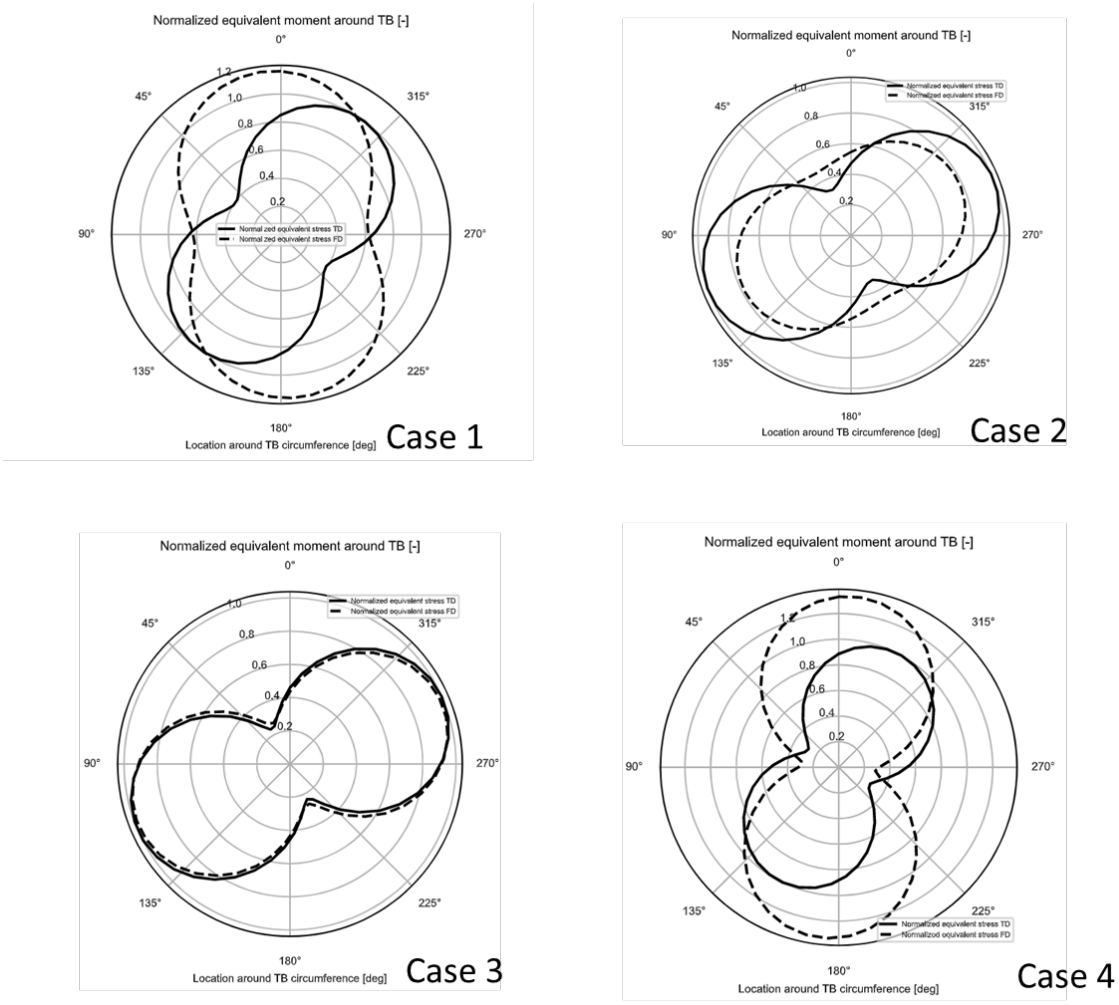

Figure 61: Normalized equivalent axial stress around tower base for all four cases. (Dotted line: RAFT analysis, continuous line: BHawC/OrcaFlex) [35]

Figure 61 shows that for case 1 and case 4, the direction of the maximum axial stress of RAFT does not align with the maximum axial stress of BHawC/OrcaFlex. The motion responses in Table 13 and Table 14 show that the roll is highly overestimated for case 1 and the pitch is highly overestimated for case 4. [35]
It is concluded that the difference in location and size of maximum stress is due to the overestimation of the pitch and roll response, as well as the assumption of a rigid tower. As the relationship between the stress in the tower base and the fatigue damage is exponential (raised to the power of m, the slope of the S-N curve), the error will grow exponentially when fatigue damage is calculated. For this reason, this frequency domain method is not deemed suitable for fatigue damage computation. [35]
The main suggestions for improvement are [35]:

- Improved mooring stiffness estimation;
- Improved turbine design and aerodynamics modelling;
- Including a flexible tower;
- Advancing the computation of hydrodynamic loads (for example including diffraction for elements like pontoons).

J Scatter diagrams

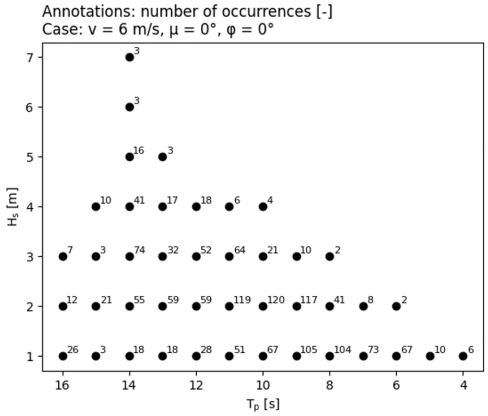

(a) v = 6 m/s, $\mu = 0°$, $\phi = 0°$

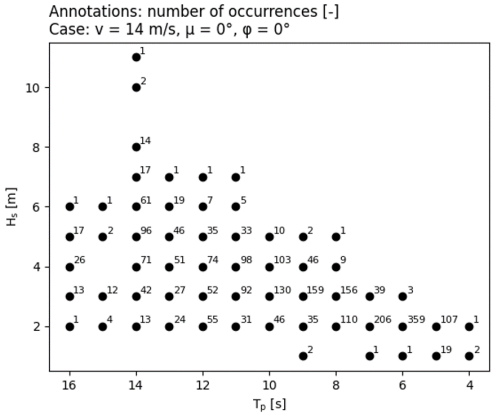

(b) v = 14 m/s, $\mu = 0°$, $\phi = 0°$

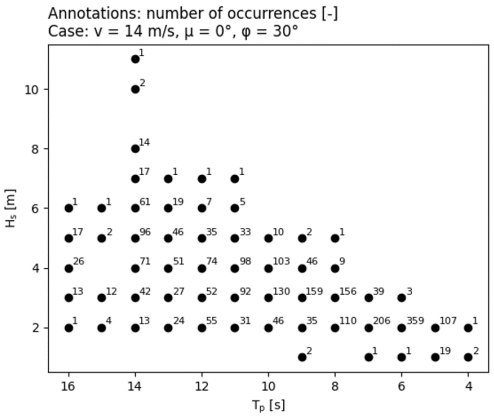

(c) v = 14 m/s, $\mu = 0°$, $\phi = 30°$

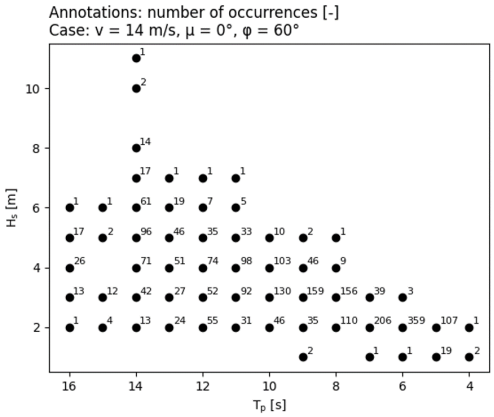

(d) v = 14 m/s, $\mu = 0°$, $\phi = 60°$

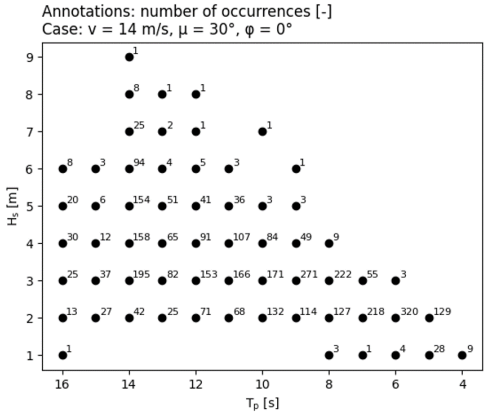

(e) v = 14 m/s, $\mu = 30°$, $\phi = 0°$

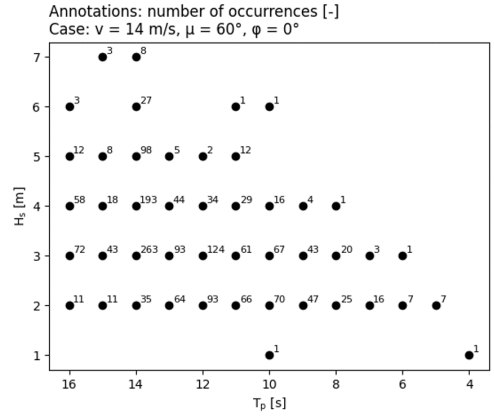

(f) v = 14 m/s, $\mu = 60°$, $\phi = 0°$

Figure 62: Scatter diagrams used in this thesis, with the number of occurrences of each sea state annotated

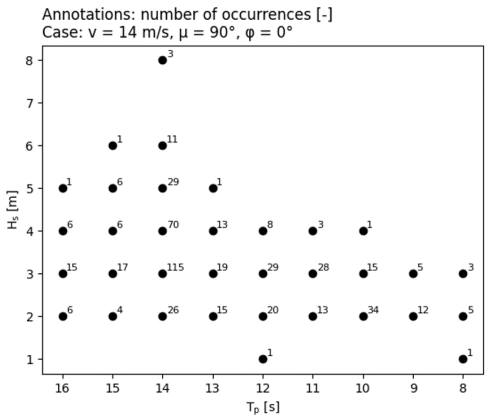

(g) v = 14 m/s. $\mu = 90°$, $\phi = 0°$

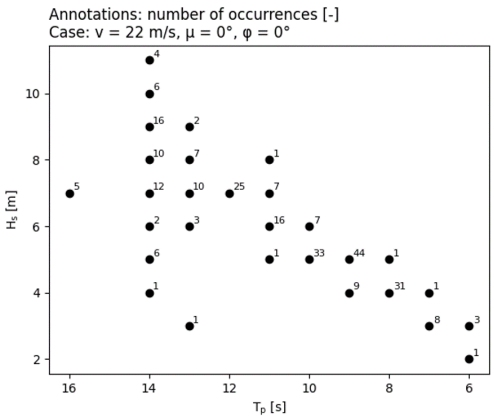

(h) v = 22 m/s, $\mu = 0°$, $\phi = 0°$

Figure 62: Scatter diagrams used in this thesis, with the number of occurrences of each sea state annotated (cont.)

K Fatigue damage computed for different wind seeds

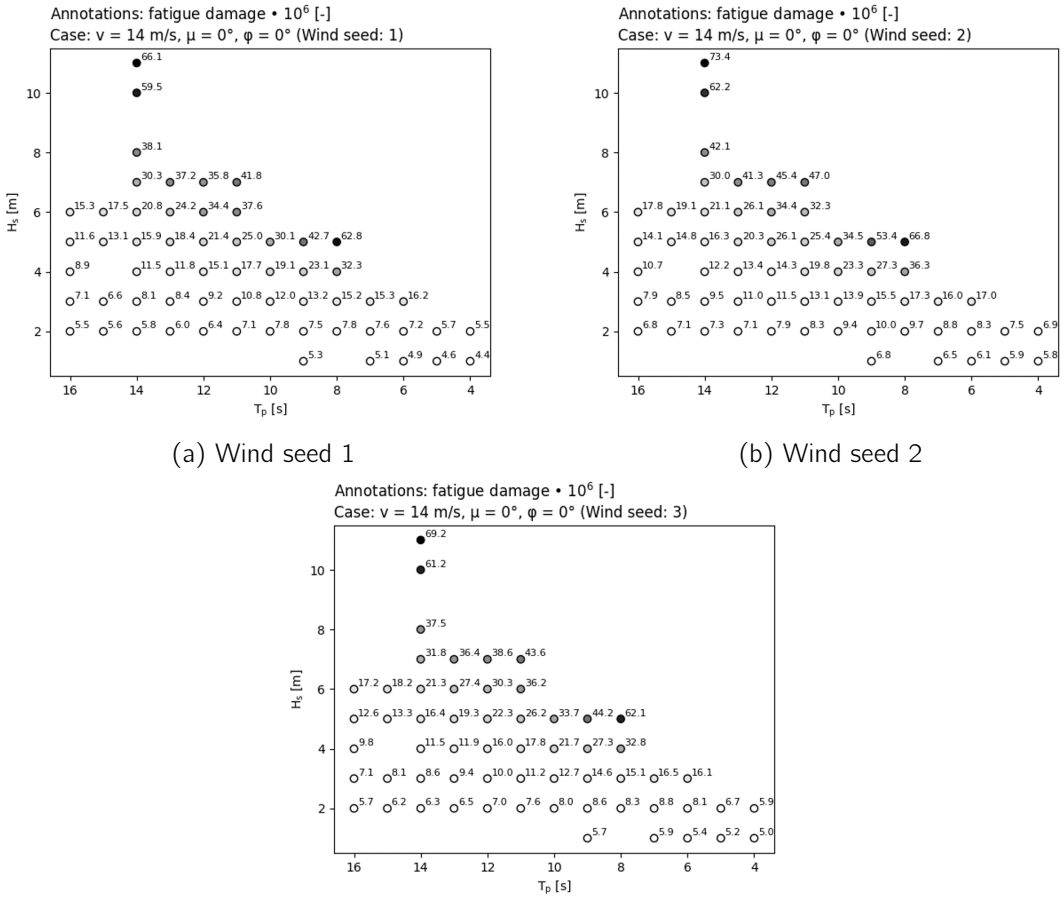

(a) Wind seed 1

(b) Wind seed 2

(c) Wind seed 3

Figure 63: Scatter diagrams, where the fatigue damages are computed using a different wind seed each. A unique wave seed for every sea state is used.

L Accuracy of the fatigue damage linear interpolation

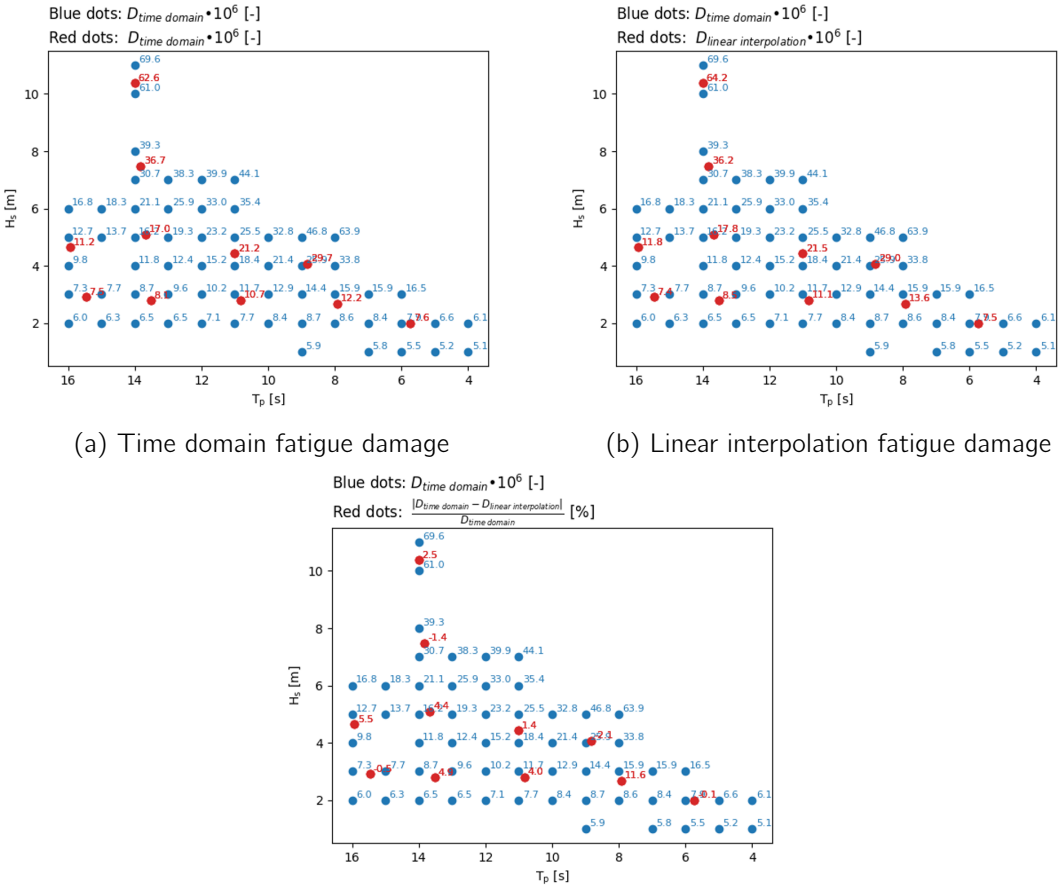

(a) Time domain fatigue damage

(b) Linear interpolation fatigue damage

(c) Linear interpolation error

Figure 64: For nine random sea states the fatigue damage is computed (a) using the time domain analysis (see Part I) and (b) using the linear interpolation method described in Section 5.2. Next, (c) the errors (in %) of the linear interpolation fatigue damages are calculated with respect to the time domain fatigue damages.

M Comparison of Seidel and Katsikogiannis

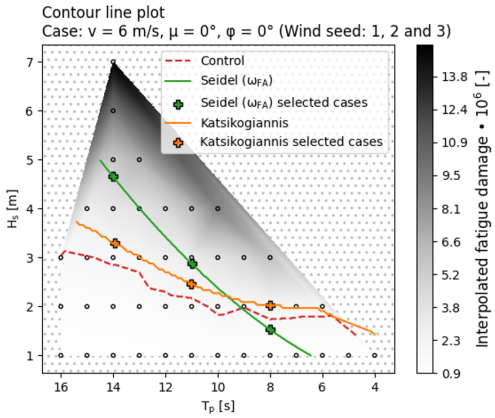

(a) v = 6 m/s, $\mu = 0°$, $\phi = 0°$

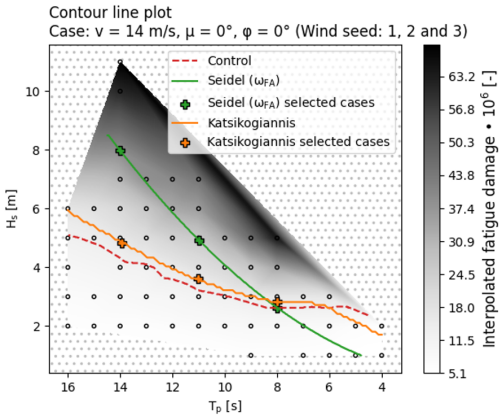

(b) v = 14 m/s, $\mu = 0°$, $\phi = 0°$

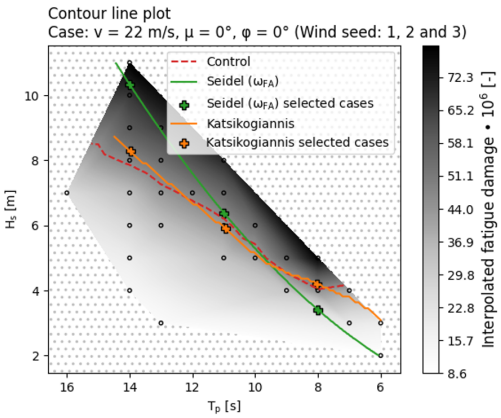

(c) v = 22 m/s, $\mu = 0°$, $\phi = 0°$

Figure 65: Lumped sea states (marked with '+') on Seidel and Katsikogiannis contour lines that were selected to compute the fatigue damage in time domain for comparison of lumping accuracy

N Comparison of block partitioning block sizes

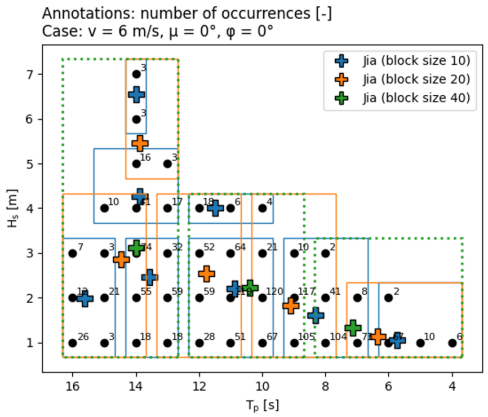

(a) v = 6 m/s, μ = 0°, ϕ = 0°

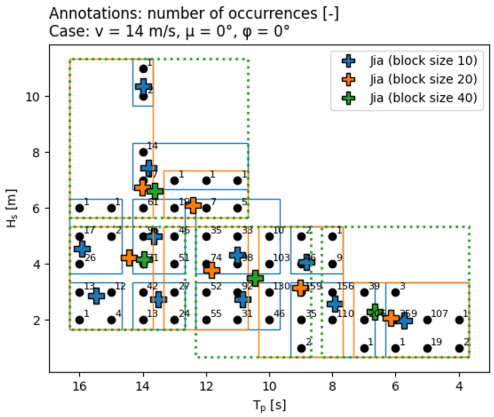

(b) v = 14 m/s, μ = 0°, ϕ = 0°

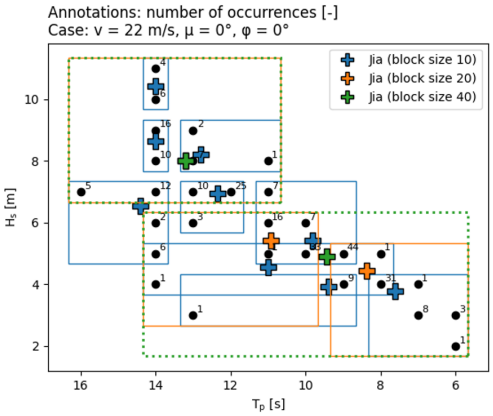

(c) v = 22 m/s, μ = 0°, ϕ = 0°

Figure 66: Lumped sea states according to the Jia method for a block partitioning with block size 10, 20 and 40

O Quantitative comparison of Jia and Song & Wang

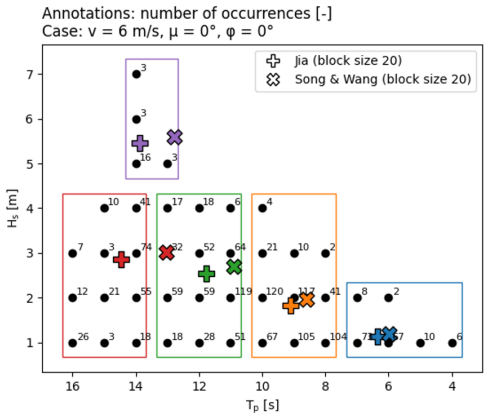

(a) $v = 6$ m/s, $\mu = 0°$, $\phi = 0°$

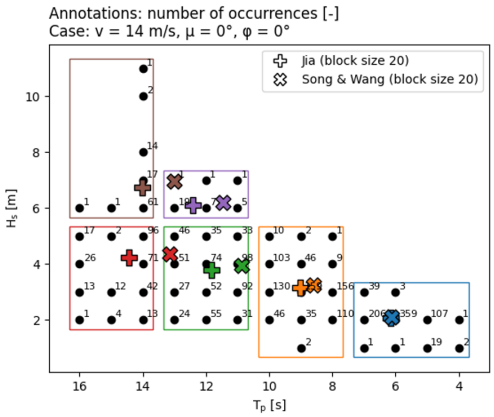

(b) $v = 14$ m/s, $\mu = 0°$, $\phi = 0°$

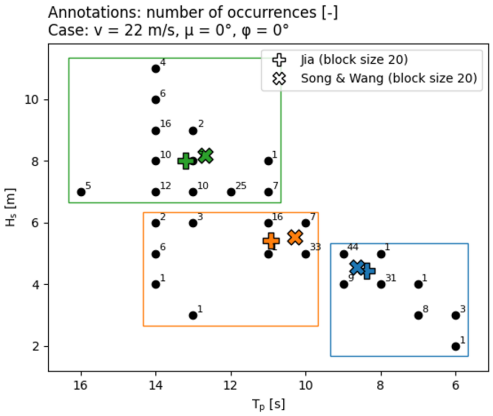

(c) $v = 22$ m/s, $\mu = 0°$, $\phi = 0°$

Figure 67: Lumped sea state resulting from the Jia and Song & Wang lumping methods (using a block partitioning of block size 20)

P Relation between zeroth spectral moment and fatigue damage

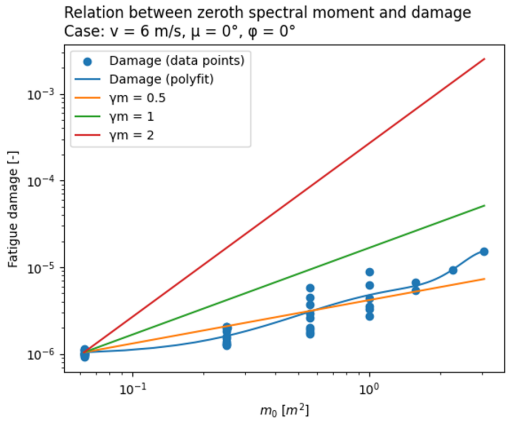

(a) v = 6 m/s, μ = 0°, ϕ = 0°

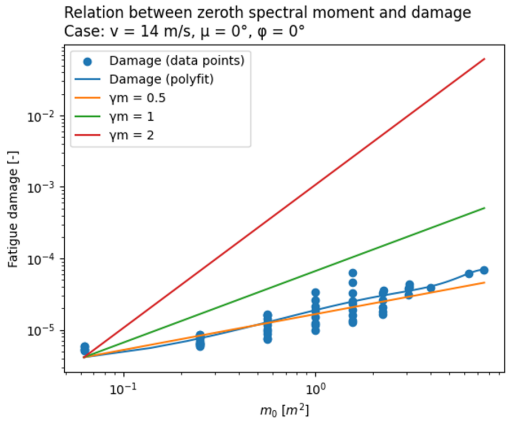

(b) v = 14 m/s, μ = 0°, ϕ = 0°

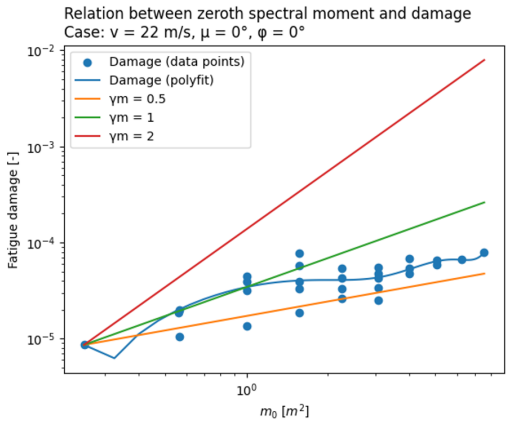

(c) v = 22 m/s, μ = 0°, ϕ = 0°

Figure 68: Relation between zeroth spectral moment (spectral energy) and fatigue damage, compared to different values of γm (according to Song & Wang [20]: $D \propto m_0^{\gamma m}$)

Q Relation between wave period definitions and the fatigue damage

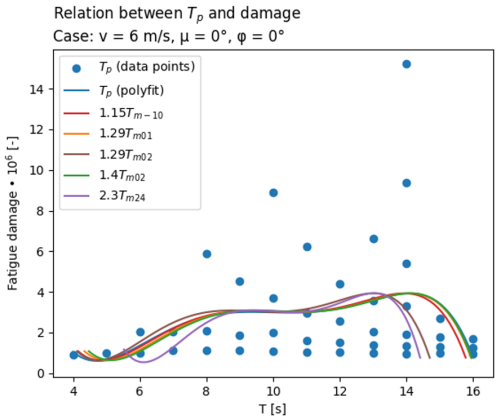

(a) v = 6 m/s, μ = 0°, ϕ = 0°

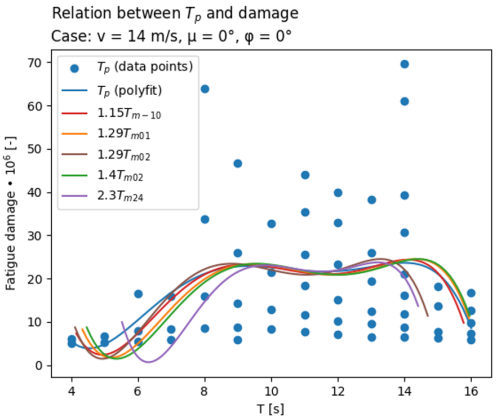

(b) v = 14 m/s, μ = 0°, ϕ = 0°

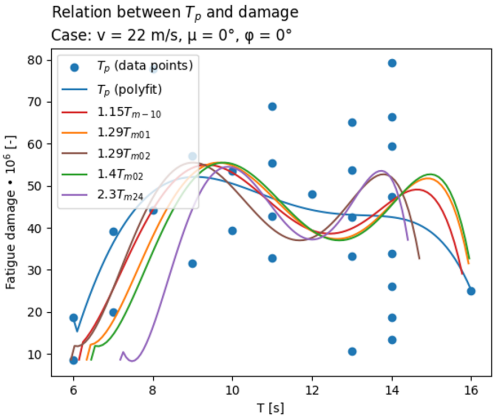

(c) v = 22 m/s, μ = 0°, ϕ = 0°

Figure 69: Relation between various definitions of the wave period and fatigue damage